Project No. 13-5180

# Three Dimensional Fuel Pin Model Validation by Prediction of Hydrogen Distribution in Cladding and Comparison with Experiment

## Nuclear Energy Advanced Modeling and Simulations

**Kostadin Ivanov**
Pennsylvania State University*

**In Collaboration with:**
North Carolina State University
University of Michigan

Dan Funk, Federal POC
Dave Pointer, Technical POC

* Currently at North Carolina State University

NEUP Nuclear Energy University Programs
U.S. Department of Energy

DOE NEUP Project 13-5180

# Three-dimensional fuel pin model validation by prediction of hydrogen distribution in cladding and comparison with experiment

## Final Report


Authors:

A. Aly, M. Avramova, K. Ivanov – North Carolina State Univesrity (NCSU)

A. Motta, E. Lacroix – Pennsylvania State University (PSU)

A. Manera, D. Walter – University of Michigan (UM)

R. Williamson, K. Gamble – Idaho National Laboratory (INL)

# Abstract

To correctly describe and predict this hydrogen distribution there is a need for multi-physics coupling to provide accurate three-dimensional *azimuthal, radial, and axial temperature distributions in the cladding*. Coupled high-fidelity reactor-physics codes with a sub-channel code as well as with a computational fluid dynamics (CFD) tool have been used to calculate detailed temperature distributions. These high-fidelity coupled neutronics/thermal-hydraulics code systems are coupled further with the fuel-performance BISON code with a kernel (module) for hydrogen. Both hydrogen migration and precipitation/dissolution are included in the model. Results from this multi-physics analysis is validated utilizing calculations of hydrogen distribution using models informed by data from hydrogen experiments and PIE data.

# Contents

# Acronyms

| | |
|---|---|
| 2D | Two Dimensional |
| 3D | Three Dimensional |
| α | Rate of precipitation |
| ANL | Argonne National Laboratory |
| APS | Advanced Photon Source |
| BC | Boundary conditions |
| BWR | Boiling Water Reactors |
| CANDU | CANada Deuterium Uranium |
| CASL | Consortium of Advanced Simulation of Light water reactors |
| CFD | Computational Fluid Dynamics |
| COBRA-TF | COolant Boiling in Rod Array – Two Fluid |
| DPA | Displacement Per Atom |
| FWHF | Full Width at Half Maximum |
| H | Hydrogen |
| HBR | High Burnup Rod |
| K | Kelvin |
| LWR | Light Water Reactors |
| MOC | Method Of Characteristics |
| Ni | Nickel |
| PIE | Post Irradiation Evaluation |
| PPM | Particles Per Million |
| PWR | Pressurized Water Reactors |
| Q* | Heat of transport |
| R | Gas constant |
| TSS | Terminal Solid Solubility |
| TSSd | TSS of Dissolution |
| TSSp | TSS of Precipitation |
| TTT | Time Temperature Transformation diagram |
| $UO_2$ | Uranium dioxide |
| VERA | Virtual Environment for Reactor Applications |
| VERA-CS | VERA-Core Simulator |
| Zr | Zirconium |
| $ZrO_2$ | Zirconium dioxide |

# List of figures and tables

# 1 Introduction

## 1.1 Purpose of the activity

Because of corrosion during normal operation in nuclear reactors, hydrogen can enter the zirconium fuel cladding and precipitate as brittle hydride particles, which can severely degrade the cladding ductility. According to previous observations, the distribution of the hydrides in the cladding is not homogeneous and responds to temperature and stress gradients. Due to the heterogeneity of the temperature distribution, hydrides tend to accumulate in the colder areas. This accumulation creates local spots of weak cladding that can favor crack initiation. Therefore, the estimation of the average concentration of the hydrides in the cladding is not sufficient to accurately estimate the risk of cladding failure. An estimation of the local hydride distribution is necessary to help predict the susceptible locations to failure due to the formation of the hydride phase in the cladding.

The hydride distribution is governed by three competing phenomena. Hydrogen in solid solution diffuses under a concentration gradient due to Fick's law and under a temperature gradient due to the Soret effect. Finally, precipitation of hydrides occurs once the hydrogen solubility limit is reached. This precipitation has its own kinetics. These phenomena are strongly temperature dependent. The complex interplay of these separate phenomena can explain why the hydrogen and hydride distribution depends on temperature. In this project, various models describing these phenomena have been developed in order to study the behavior of hydrogen a in the cladding.

Due to the complexity of the modelling, it is usually not possible to find an analytical solution for the hydrogen and hydride distribution for nuclear fuel rod geometries. Numerical solutions were obtained from the implementation of the model in computer program. A more detailed model was then implemented in the three-dimensional (3-D) fuel performance code BISON in order to calculate the hydrogen distribution for more sophisticated geometries, such as a nuclear fuel rod. Several high fidelity multi-physics codes were used to accurately predict the temperature distribution in cladding. MPACT is a neutron transport code used within VERA (Virtual Environment for Reactor Applications). The code provides modelling capabilities for 3-D method of characteristics (MOC), 2-D/1-D time-dependent transport, and traditional 2-D lattice physics capabilities. The modernized version of COBRA-TF (COolant Boiling in Rod Array – Two Fluid) code o known as CTF is a multidimensional sub-channel thermal hydraulics code. It is being utilized in the CASL (Consortium for Advanced Simulation of Light Water Reactors) project for high-fidelity thermal hydraulics calculations. Those codes were coupled by TIAMAT, a multi-physics coupling code that was developed within CASL project as part of the VERA. It was used to couple the three single physics codes described above to perform high fidelity coupled calculations. Star-CCM+ CFD code was used to generate high resolution cladding temperature boundary conditions around grid spacers with mixing vanes to investigate their effect on the hydrogen distribution and compare the level of details to that obtained from CTF.

The results shown by these simulations explain the formation of specific radial distribution of hydrides. The simulations predict that before precipitation occurs, hydrogen tends to accumulate in the colder spots due to the Soret effect. Once the solubility limit is reached, hydrogen precipitates and forms a rim close to the outer edge of the cladding. This is due to the competition between

precipitation and diffusion. The simulations also show an axial transfer of hydrogen from the top of the rod, where the oxidation rate is high, to the bottom of the rod, where the hydrogen will precipitate. The implemented model is able to provide additional information on the azimuthal hydrogen distribution due to asymmetric temperature profile on the outer surface of the cladding due to the presence of cooler locations around guide tubes for instance.

The model used to describe hydrogen behavior is semi-empirical. In particular, two empirical constants have to be determined that do not have consistent values in the literature. Therefore, two experiments were designed and performed in order to measure these constants. The first constant is the heat of transport Q*, which determines the Soret effect. This was measured by applying a temperature gradient to a Zircaloy plate that was previously charged with hydrogen. The measured value for Q* was 58.5 kJ/mol and is higher than previous measurement. The results confirm the large variability of the measurement of the heat of transport. The second constant is the rate of precipitation $\alpha^2$ from Marino, which describes the rate at which the supersaturated hydrogen in solid solution precipitates into zirconium hydrides. This rate is measured through an in-situ X-Ray diffraction experiment in transmission, at the Advanced Photon Source of the Argonne National Laboratory. The results are between 0.013 s-1/2 and 0.034 s-1/2 and are in the same range of values as found in previous experiments. However, no clear trend of temperature dependence has been identified.

## 1.2 Framework of the activity

The work reported in this paper is supported by the US DOE NEUP Project 13-5180 entitled “Three-dimensional fuel pin model validation by prediction of hydrogen distribution in cladding and comparison with experiment”.

The objectives of this project are:

a) Validation of the NEAMS tool BISON for predicting fuel performance in a LWR environment;

b) Use of measured data for hydrogen distribution in the cladding (both from model experiments on artificially hydrided cladding and from the available results of PIE examinations of in-reactor material) in order to assess the predictions of temperature and hydrogen distributions by BISON;

c) Validating the 3-D fuel pin models and proving the importance of high-fidelity multi-physics coupling;

d) Identification of both deficiencies in BISON fuel performance models (if any) as well as gaps in the experimental databases as areas needing further development.

# 2 Theoretical background

This chapter provides the fundamental understanding of the hydrogen behavior in the LWR fuel cladding. The section 2.1 gives the general background of the role of zirconium alloy as a material for the cladding. It is followed, in section 2.2, by the description of the oxidation mechanisms that produce hydrogen at the interface between the coolant and the fuel cladding. In section 2.3, the mechanism of the hydrogen pick-up is briefly explained as a prelude to the calculation of the incoming hydrogen flux in the zirconium cladding. Section 2.4 presents the key elements to understanding the redistribution of hydrogen in the cladding, starting with the experimental observations (sections 2.4.1 and 2.4.2) followed by a description of physical understanding through different models (section 2.4.3, 2.4.4, 2.4.5 and 2.4.6).

## 2.1 Zirconium Alloys for Nuclear Fuel Cladding

The core of a Light Water reactor (LWR) contains fuel assemblies that are cooled by water. Each assembly is made of a series of fuel rods (approximately 4 m in height and 9.6 mm in diameter) that contain fissile material in the form of uranium dioxide pellets ($UO_2$). These fuel rods are sheathed in the nuclear fuel cladding, made of zirconium alloy, which serves as the primary barrier to contain fission products between the nuclear fuel and the primary coolant water.

Zirconium alloys have been chosen as cladding material primarily for their very low thermal neutron absorption cross section (0.185 barns (or $0.185 \times 10^{-24} cm^2$) for 0.0253eV neutrons), which allow for a good neutron economy [1]. Zirconium alloys also exhibit good corrosion resistance, good heat transfer properties, appropriate mechanical strength for LWR conditions and are, to a certain extent, resistant to radiation damage [2].

During in-reactor operation, the zirconium cladding is subject to environmental degradation. The cladding tube is under stress from the pressure of the fission gases emitted from the uranium pellet and can eventually chemically bond with the pellet itself. The typical temperature of the inner cladding wall is about 380 ºC. The outer wall of the cladding is in contact with the cooling water and its temperature is approximately 330 ºC. At this boundary, waterside corrosion occurs. The corrosion reaction generates hydrogen, some of which is picked up by the cladding [3]. Additional sources of hydrogen production are water radiolysis and hydrogen added to the reactor core primary water. Radiation damage also affects the properties of the cladding. Typically, during the 3 year operating lifetime of the fuel rod, each atom in the zirconium cladding is displaced 20 times (20 dpa). This causes an alteration of the material properties [2].

Historically, the alloy most often used in Pressurized Water Reactors (PWRs) is Zircaloy-4, while Zircaloy-2 is used in Boiling Water Reactors (BWRs). Recently, PWRs have started to use more modern alloys such as ZIRLO® and M5®, which exhibit improved corrosion resistance, compared to Zircaloy-4 [4][5]. Another zirconium alloy, Zr-2.5Nb is also used in heavy water reactors such as CANDU reactors. Although the alloying elements are added in small quantities, they have a strong impact on the in-service behavior of the alloy strongly, especially its corrosion resistance. There are other alloys, especially Russian alloys that are not covered by this study.

## 2.2 Origin of hydrogen in the LWR fuel cladding

### 2.2.1 Reactions producing hydrogen in the cladding in LWR

As stated above, the hydrogen produced in the LWR cores comes from three main sources. The first source is the waterside corrosion reaction shown in equation 2-1.

$$Zr + 2H_2O \rightarrow ZrO_2 + 4H \qquad \textit{Eq 2-1}$$

Second, hydrogen can be generated by radiolysis [6] according to the following reaction:

$$H_2O \xrightarrow[(\gamma,n)]{} H^+ + OH^- \qquad \textit{Eq 2-2}$$

Third, hydrogen can be purposefully added to the primary water to limit oxidation. Other factors, such as hydrogen present in the fuel pellets, can make additional hydrogen atoms available to enter the cladding.

### 2.2.2 Kinetics of the cladding oxidation

The oxidation kinetics have been formulated with semi empirical models, which are detailed in the Waterside Corrosion report, produced by the International Atomic Energy Agency (IAEA) [7]. These models separate two different kinetic behaviors. At first, oxidation weight gain kinetics is governed by a cubic rate law:

$$w^3 = k_c * t \qquad \text{Eq 2-3}$$

with:

$$k_c = A_{kc} * exp\left(-\frac{Q_{kc}}{RT}\right) \qquad \text{Eq 2-4}$$

with:

w the weight gain (per unit area)

$A_{kc}$ the pre-transition frequency factor (in $\mu m^3/d$)

$Q_{kc}$ the pre-transition activation energy for oxide growth

R the as constant

t the temperature (K)

Assuming that all oxygen weight gain is used to produce $ZrO_2$ and that no $ZrO_2$ oxide is lost by spallation or dissolution, the oxide layer thickness is proportional to the weight gain [8]:

$$\delta(\mu m) = \frac{w\frac{mg}{dm^2}}{14.7} = \frac{(k_c * t)^{\frac{1}{3}}}{14.7} = K_c^{\frac{1}{3}} * t^{\frac{1}{3}} \qquad \textit{Eq 2-5}$$

Then, the oxide thickness follows a cubic law and oxidation gradually falls down. The equations above reflect the volume expansion of the oxide relative to the metal. The new constant is defined as:

$$K_c = \frac{k_c}{14.7^3} \quad \text{Eq 2-6}$$

At about an alloy dependent thickness (for Zircaloy-4), a kinetic transition is observed. At this point, the oxidation kinetics returns to the initial value seen at the start of the corrosion of the bare metal [9]. Afterwards, the oxidation kinetics can be approximated with a linear rate law:

$$w = k_l * (t - t^*) + w^*, k_l + A_{kl} * \exp(-\frac{Q_{kl}}{RT}) \quad \text{Eq 2-7}$$

With:

w the weight gain
$k_l$ the proportionality constant
t* the transition time
w* the weight gain at the transition.

In terms of oxide thickness,

$$\delta = \delta^* + K_L * (\delta - \delta^*) \quad \textbf{Eq 2-8}$$

Experimental data has been used to calculate the kinetic proportionality constants. According to [7], the values given in Table have been considered in previous work and fuel performance codes:

*Table 2-1: Empiric oxidation kinetics parameters*

| *Source / model* | *Pre transition frequency factor* | *Pre transition activation energy* | *Post transition frequency factor* | *Post transition activation energy* | *Transition oxide thickness S=A*exp(-B/T)* [µm] | |
|---|---|---|---|---|---|---|
| | | | | | A | B |
| | $\mu m^3.d^{-1}$ | $K^{-1}$ | $\mu m^3.d^{-1}$ | $K^{-1}$ | *µm/days* | $K^{-1}$ |
| MATPRO[10] | $4.976*10^9$ | 15,660 | $8.288*10^7$ | 14,080 | 7.749 | 790 |
| EPRI KWU/C-E | $1.78*10^{10}$ | 16,250 | $8.04*10^7$ | 13,766 | $2.14*10^7$ | $-\frac{5417}{T} - 0.0117T$ |
| COCHISE | $11.4*10^{10}$ | 17,171 | $4.0*10^{11}$ | 18,391 | $8.857*10^{10}$ | $\frac{921}{T} - 0.035T$ |
| Motta (private | 535 | 4533 | $8.1*10^6$ | 12,500 | 4.35 | 550 |

Figure 2-1 represents the evolution of the Zircaloy-4 oxide layer thickness, at 320°C, for 9 years. The curves have been drawn following to the equations Eq 2-5 and Eq 2-8 and using the model constants given in Table 2-1.

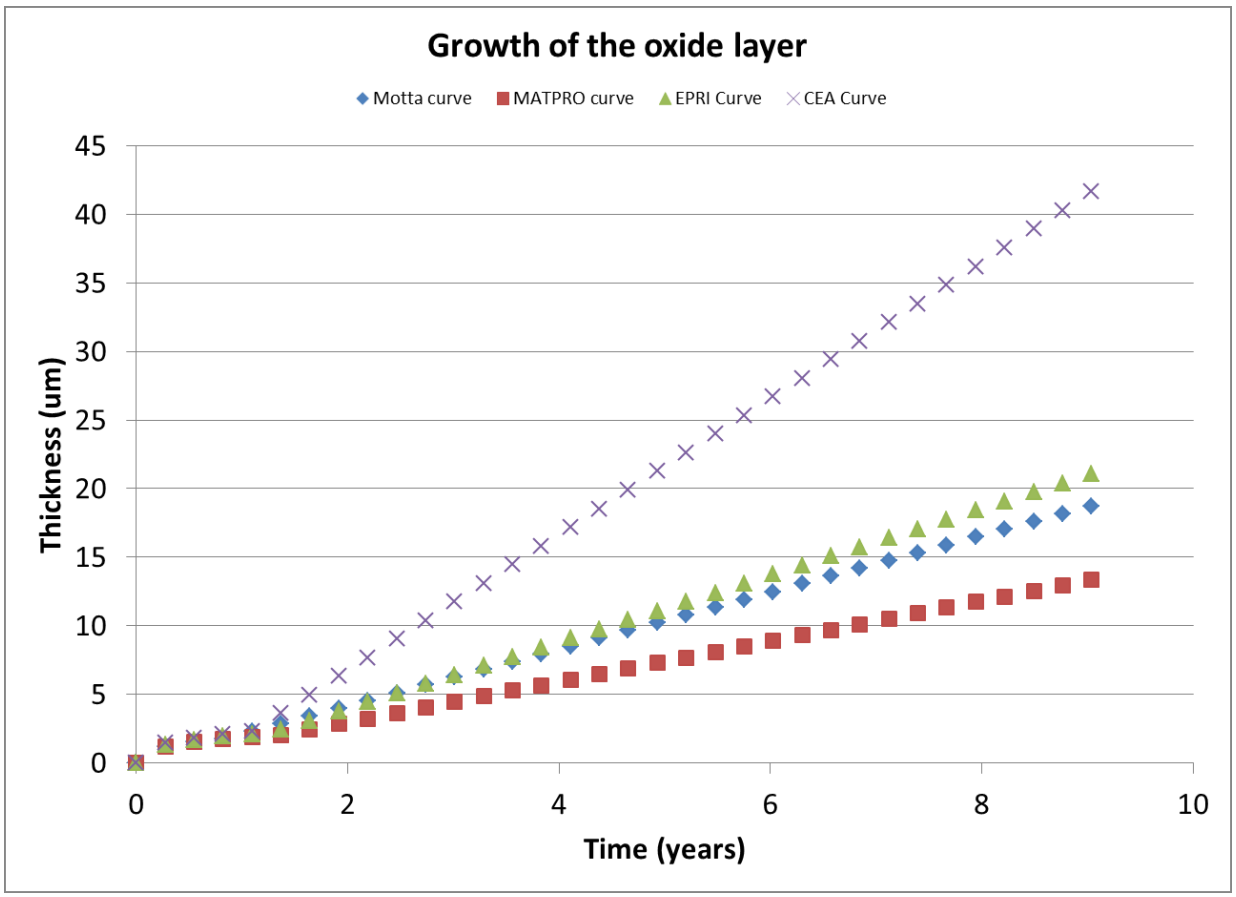


*Figure 2-1: Growth of the cladding oxide layer according to oxidation kinetics models in Table 2-1.*

### 2.2.3 Empirical Hydrogen Pick-up in LWR cladding

Some of the hydrogen atoms produced by the mechanisms detailed in the section 2.2.2 are transported to the oxide-metal interface and can be absorbed into the cladding. This process is called hydrogen pick-up. The absorbed hydrogen migrates through the material in response to thermodynamic driving forces, which will be detailed in the next sections. For Zircaloy-4, 10% to 20% of the hydrogen liberated from corrosion is typically absorbed into the cladding. Factors influencing hydrogen pick-up may include:

a) Oxide film characteristics (thickness, morphology and crystal structure);

b) Second phase particles of various characteristics;

c) Zirconium alloy composition and microstructure;

d) Residual stresses;

e) The ratio of area/volume exposed to corrosion;

f) Water chemistry and more specifically radiolysis of the water during irradiation.

The work from Adrien Couet [11][12] gives information on the pick-up mechanisms. While no accurate model has been proposed at this time, a typical value of 15% is admitted as an average pick-up.

## 2.3 Hydrogen flux entering the cladding

According to the previous section, it is possible to calculate the hydrogen flux that enters the cladding at the coolant interface. The quantity of Zr oxide in the oxide layer, per unit of surface, is given by:

$$\boldsymbol{n_{ZrO_2} = \delta * \frac{\rho(ZrO_2)}{M(ZrO_2)}} \qquad \text{Eq 2-9}$$

With $\delta$ the oxide thickness, $\rho(ZrO_2)$ the oxide density and $M(ZrO_2)$ the oxide molar mass. According to the oxidation reaction (Eq 2-10) , there are 4 atoms of hydrogen for each molecule of Zr oxide.

$$\boldsymbol{Zr + 2H_2O \rightarrow ZrO_2 + 2H_2} \qquad \textbf{\textit{Eq 2-10}}$$

Assuming f=15%, the hydrogen pick-up fraction, the amount of hydrogen picked up by the cladding is given by:

$$\boldsymbol{n_H = 4f * \delta * \frac{\rho(ZrO_2)}{M(ZrO_2)}} \qquad \text{Eq 2-11}$$

The mass of hydrogen picked up is:

$$\boldsymbol{m_H = 4f * \delta * \frac{\rho(ZrO_2)}{M(ZrO_2)} * M_H} \qquad \text{Eq 2-12}$$

With $M_H$ the hydrogen molar mass.

It is common to use wt. ppm for the concentration of hydrogen. Thus, it is necessary to evaluate the amount of zirconium (per unit of surface) in the cladding, which is given by Eq 2-13.

$$\boldsymbol{m_{Zr} = \rho(Zr) * (thickness - \delta)} \qquad \text{Eq 2-13}$$

The thickness corresponds to the thickness of the cladding, which is usually close to 650 microns. Finally, the average concentration of hydrogen in the cladding is given by Eq 2-14.

$$\boldsymbol{C_H[wt.ppm] = 4f * \frac{\frac{\rho(ZrO_2)}{M(ZrO_2)} * \delta}{\frac{\rho(Zr)}{M(Zr)} * (thickness - \delta)} * \frac{M_H}{M_{Zr}} = \frac{4f}{1.56} \frac{\delta}{(thickness - \delta)} * \frac{M_H}{M_{Zr}}} \qquad \text{Eq 2-14}$$

### 2.3.1 Shape of hydrogen overall concentration

Figure 2-2 gives the average hydrogen concentration evolution with time, assuming a constant hydrogen pick-up fraction of 15%, using a cladding/coolant interface temperature of 320°C and a cladding thickness of 0.6 mm.

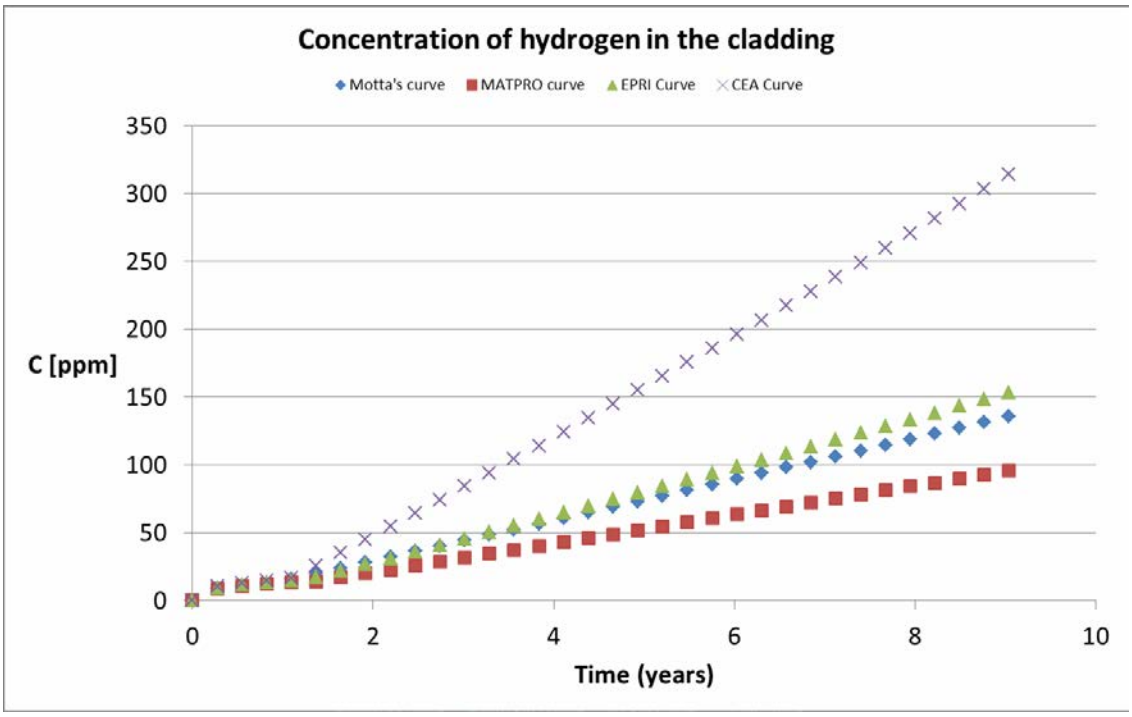


*Figure 2-2 Evolution of the average cladding hydrogen concentration with time at 320°C, using kinetics models of Table 2-1.*

### 2.3.2 Hydrogen flux at the coolant/cladding interface

The rate of the increase of the oxide layer is:

- For the cubic regime (according to Eq 2-5)

$$\frac{d(\delta)}{dt} = (k_c)^{\frac{1}{3}} * \frac{1}{3} t^{-(\frac{2}{3})} \qquad \textbf{Eq 2-15}$$

- For the linear regime (according to Eq 2-8)

$$\frac{d(\delta)}{dt} = k_L \qquad \text{Eq 2-16}$$

The rate of the increase of hydrogen in the cladding is given by:

$$\frac{dC_H}{dt} = \frac{d}{dt}\frac{4f}{1.56}\frac{\delta}{(thickness-\delta)} * \frac{M_H}{M_{Zr}}$$

$$\frac{dC_H}{dt} = \frac{4f}{1.56}\frac{M_H}{M_{Zr}}\frac{d}{d\delta}\frac{\delta}{(thickness-\delta)} * \frac{d\delta}{dt} \qquad \text{Eq 2-17}$$

$$\frac{dC_H}{dt} = \frac{4f}{1.56}\frac{M_H}{M_{Zr}}\frac{thickness}{(thickness-\delta)^2} * \frac{d\delta}{dt}$$

By conservation of species:

$$\frac{dC_H}{dt} * V = J * S \qquad \textit{Eq 2-18}$$

Where V is the volume of cladding considered and J is the flux of hydrogen coming into this volume through the cross-section S. The cross-section S multiplied by the cladding thickness is equal to the volume V.
Therefore:

$$J = \frac{4f}{1.56} * \frac{M_H}{M_{Zr}} * \frac{thickness^2}{(thickness-\delta)^2} * \frac{d\delta}{dt}\ (wt.ppm.cm^{-2}s^{-1}) \qquad \text{Eq 2-19}$$

In a first approximation, the thickness factor can be neglected. The equation becomes:

$$J = \frac{4f}{1.56} * \frac{M_H}{M_{Zr}} * \frac{d\delta}{dt}(wt.ppm.cm^{-2}s^{-1}) \qquad \textit{Eq 2-20}$$

## 2.4 Redistribution of hydrogen in the cladding

Once the hydrogen enters the cladding, it can exist within two different phases. The hydrogen in solid solution corresponds to H atoms occupying interstitial sites in the hcp zirconium structure. At higher concentrations, hydrogen precipitates and forms hydrides (mostly delta hydrides)[13][14] . The distribution of hydrogen within these two species is strongly interdependent and the specific hydrogen distributions can reduce cladding ductility and create other critical challenges for the nuclear industry. The main purpose of this thesis will be to study, model and simulate this distribution.

### 2.4.1 Consequence of hydrides on Zircaloy cladding properties

According to various work including Robert Daum's mechanical project[15][16], a local high concentration of hydrides has a significant impact on the Zircaloy-4 fuel cladding. Daum's study showed that local accumulation of hydrogen (>5900 wt. ppm) in a hydride rim at the outer surface of the cladding could result in the precipitation of a mixture of hydride phases. Thick rims appear to be susceptible to cracking at 300°C or temperatures close to normal reactor operation and a hot zero power condition.

According to his testing, the propagation of these cracks through the cladding wall is highly dependent on temperature and hydride-rim thickness. Cladding with thin rims (<100 μm) appears to have considerable resistance to unstable crack propagation at temperatures >300°C. A hydride-rim thickness of 100 μm is at the higher end of usual thicknesses formed in typical intermediate and high burnup Zircaloy-4 cladding. For cladding with thicker rims or blisters, surface crack nucleation and subsequent mixed propagation is expected to occur at relatively low plastic strains or, in the case of his study, <2% far field hoop strain. At higher temperatures (375°C), the cladding is ductile even at

a hydride-rim thickness of 210 μm. However, such thick rims are likely to induce a loss of ductility due to the presence of small cracks within the rim.

### 2.4.2 Previous observations and measurements of hydride formation in Zr alloys

According to the following observations, the hydrogen in Zr cladding redistributes because of temperature gradients. The hydrogen tends to move to the cold areas and to precipitate there.

#### 2.4.2.1 Radial distribution of hydrogen in Zircaloy cladding

A radial gradient in the hydride distribution has been observed regularly for cross- sectional samples coming from LWR. At high burnup, a high concentration region is observed, constituting a hydride "rim". Figure 2-3 is a cross-sectional metallography of a cladding coming from a PWR reactor. As in similar studies, the hydride rim is located close to the outer edge of the cladding, where the temperature is the lowest. This is consistent with the assumption that hydrogen diffuses in Zircaloy according to temperature gradients.

A study of Bossis and al.[18] shows that at high burnup, the average concentration in the rim can go up to 1300 wt.ppm, when the cladding average concentration is 430 wt.ppm. Figure 2-4 shows the metallography related to this observation. The hydride rim is also located close to the cladding/coolant interface.

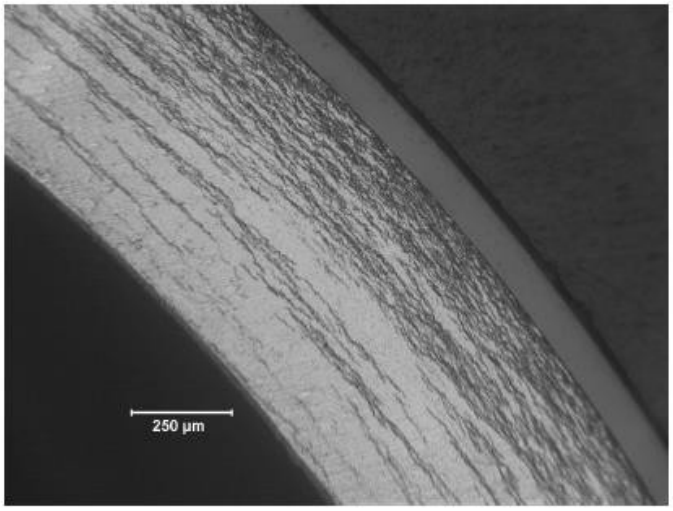


*Figure 2-3 Hydride distribution and morphology in HBR rod F07 cladding near b650 mm above*

*mid plane (740-wppm H).*[17]

*Figure 2-4 Optical micrographs of the hydride distribution and oxide layers on Zircaloy-4 irradiated for 6 cycles in PWR.*[18]

### 2.4.2.2 Axial oxidation behavior and consequence on hydrogen production

Because of the heat production in the fuel, the coolant temperature gradually increases along the axial direction. It also decreases locally close to the spacer grids, due to the presence of elements that are mixing the coolant flow (mixing vanes or castellations). Figure 2-5 shows the oxide thickness as a function of the elevation. It shows that the oxide growth follows the same profile as the temperature, increasing generally and decreasing locally at the spacer grids locations [19]. No precise measurement giving hydrogen concentration as a function of axial elevation has been found. Rough estimations have been provided by Zhang in his work [20]. Image treatment has been used on cross sectional metallography in order to estimate the hydride concentration. However, the results do not seem to be usable, due to very high uncertainties.

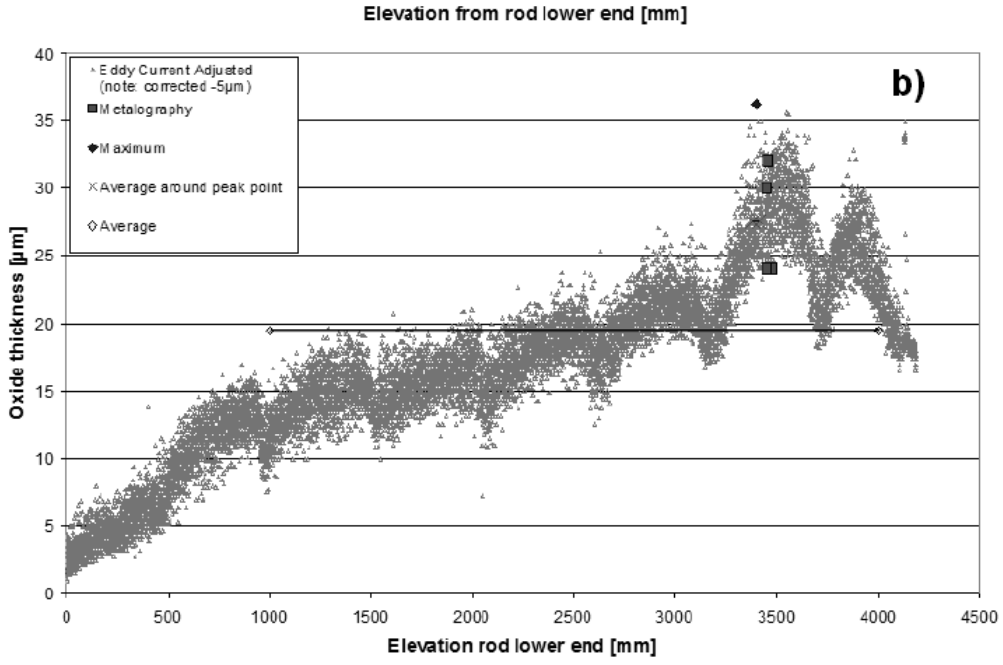

*Figure 2-5 Increase of oxide layer thickness with elevation in a PWR reactor (burnup 70 MWd/kgU).*[19]

### 2.4.2.3 Azimuthal distribution of hydrogen in the cladding

Due to the heterogeneity of the core geometry, the cladding is subjected to a heterogeneous temperature distribution. Guide tubes, corners and sides of the assemblies create colder boundary conditions and, therefore, affect the hydrogen distribution. This phenomenon has been observed by Billone and co-workers [17]. *Figure 2-6* is a collection of irradiated cladding metallography coming from one of their ring compression test. The average total hydrogen concentration has been measured with hot vacuum extraction for different azimuthal sections. The variations between different sections are greater than 150 wt.ppm. Moreover, the result of the test shows that the crack is formed where the concentration is the highest. This confirms the fact that hydrides weaken the cladding.

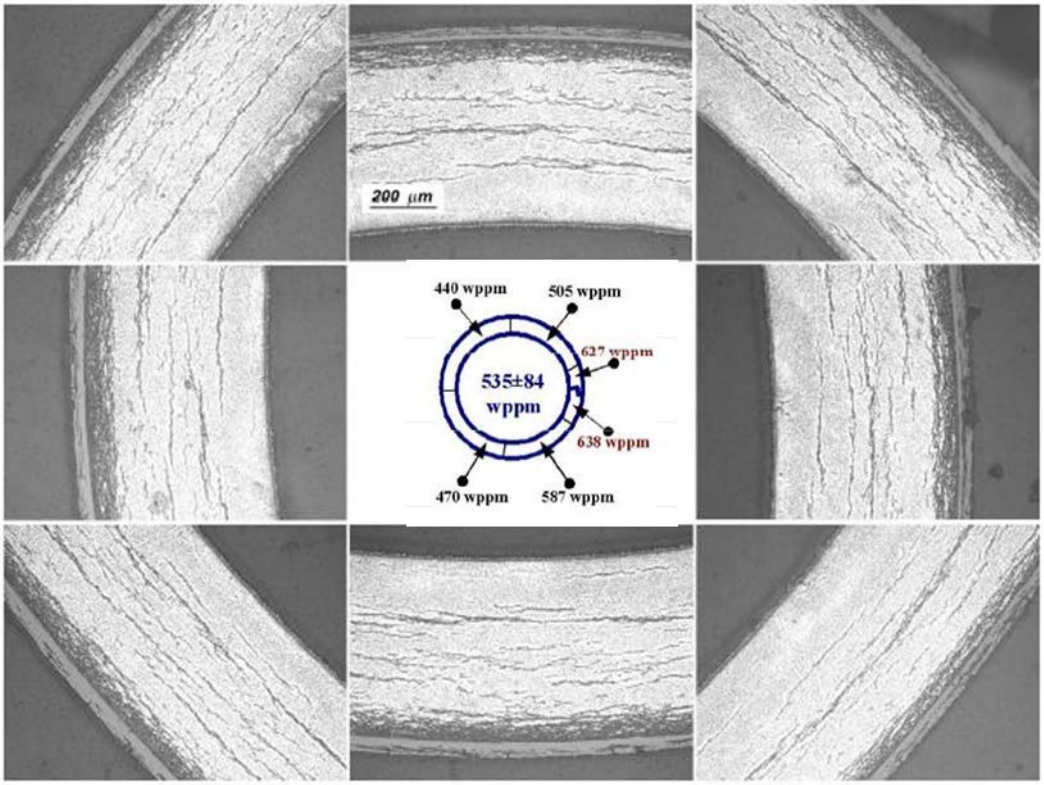


*Figure 2-6 Azimuthal variations of the hydride distribution.*

### 2.4.2.4 Azimuthal distribution of hydrogen in the cladding

Another classical observation regarding the temperature dependence of hydrogen distribution is the enhancement of the concentration of hydride at the inter pellet gap. The mechanical stress due to pellet expansion led to the creation of chamfers, at the top and bottom of the pellets. Figure 2-7 is a metallography of showing a full pellet and its neighboring pellets. The inter-pellet gap forms at the interface between two pellets and has been circled in red.

The presence of chamfers leads to lower temperatures at their locations, which creates a cold spot in the cladding, as it can be seen from a fuel performance calculation (BISON). Figure 2-8 shows the temperature profile at the inter-pellet gap. The pellet is represented in green and its temperature is not displayed. At the inter-pellet gap, a decrease of about 20°C is observed. This is mainly due to the fact

that there is less energy deposition at the inter-pellet gap and that the gap created by the chamfers is filled by the fission gases and the initial helium, which have a significant thermal resistance.

The work by Smith[21] shows a very high concentration of hydrides close to the inter-pellet gap, compared to the mid-pellet cladding. Figure 2-9 shows three different micrographs, coming from the same road. The picture a, on the left, shows the hydride distribution far from the inter-pellet gap. The rim can be seen. On the contrary, the pictures b and c show hydride distribution in the inter-pellet gap. Almost the full thickness is covered by hydrides. This is consistent with the temperature profile shown above.

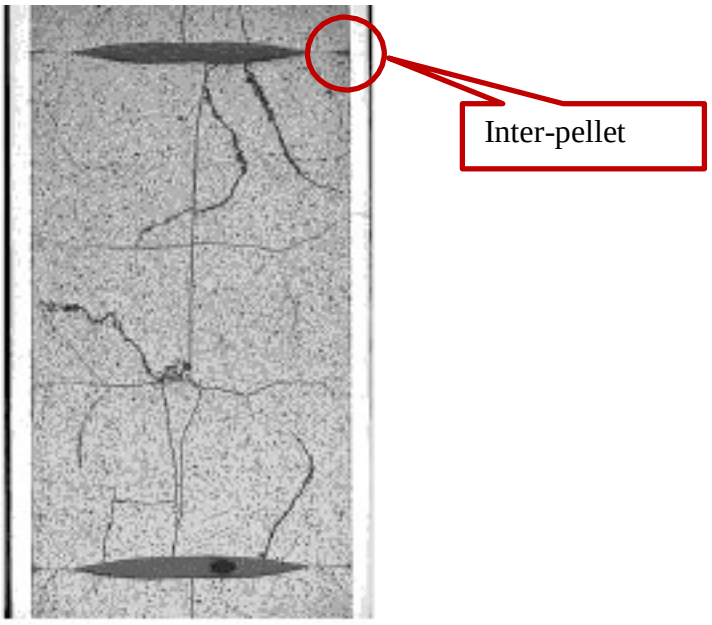


*Figure 2-7 Axial macrograph of a fuel rod.*

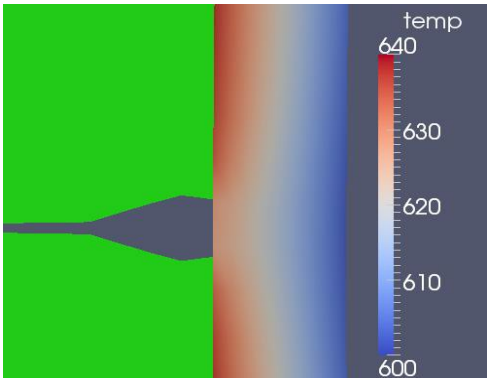


*Figure 2-8 Cladding temperature profile (K) around the inter-pellet gap as calculated with BISON.*

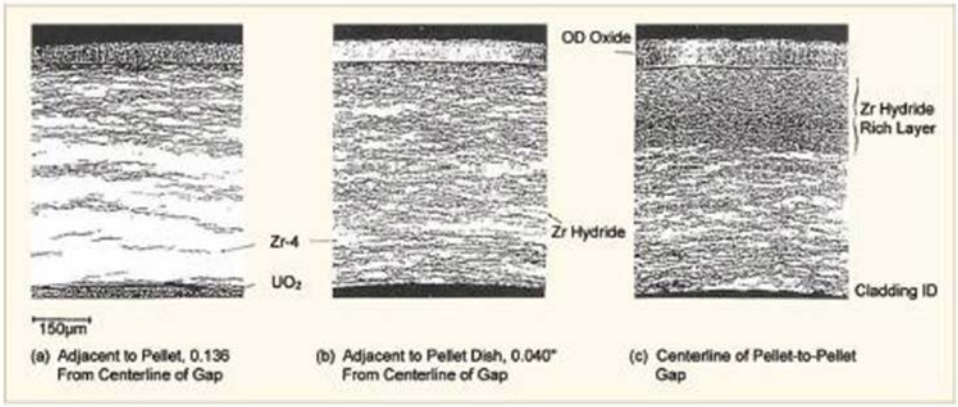


*Figure 2-9 Hydride distribution at the inter-pellet gap cladding compared to mid-pellet cladding.*[21]

#### 2.4.2.5 Oxide spallation

When the oxide thickness reaches a very high value (> 80 ), oxide spallation can occur [22]. At the spallation, the metallic cladding is directly in contact with the coolant, and its temperature decreases quickly. Previous observations show the formation of a hydride blister (pure hydride) at the location of the spallation. Figure 2-10 shows a metallography of a cladding portion where the spallation has occurred. A blister formed at the outer edge. According to these observations, a high concentration of hydrides is usually observed at the lower temperature spots in the nuclear fuel cladding.

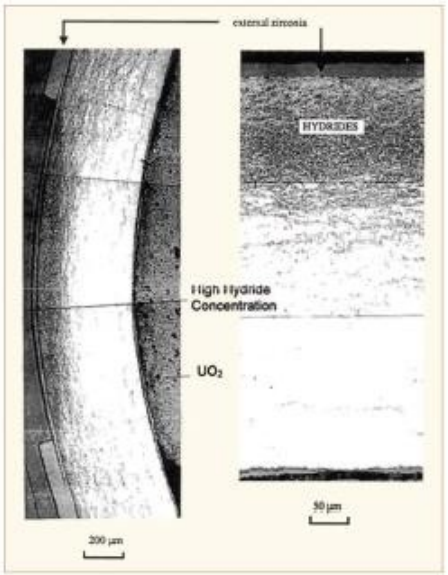


*Figure 2-10 Hydride blister due to oxide spallation.*[22]

### 2.4.3 Hydrogen diffusion in Zircaloy

In order to study the formation of the specific hydride distribution, it is necessary to understand the phenomena that govern the distribution of hydrogen in solid solution. One of these phenomena is the diffusion of hydrogen. The hydrogen diffusion in solid solution in the zirconium matrix is governed by two driving forces: the concentration gradient and the temperature gradient.

#### 2.4.3.1 Fick's law and diffusion coefficient

A concentration gradient in the hydrogen distribution generates a flux according to Fick's law. This concerns only the hydrogen in solid solution, as the hydrogen in hydrides is immobilized within that place.

$$J_{Fick} = -D * \nabla C_{ss} \quad \text{Eq 2-21}$$

$J_{Fick}$ is the diffusion flux due to concentration gradient.

$C_{ss}$ is the concentration of hydrogen in solid solution.

D(T) is the diffusion coefficient, which is governed by an Arrhenius law:

$$D = A_D * exp\left(-\frac{Q_D}{RT}\right) \quad \textit{Eq 2-22}$$

The coefficients have been measured by Kearns [23]:

$$A_D = 7.90 * 10^{-7}\ m^2/s \quad \textit{Eq 2-23}$$

$$Q_D = 4.49 * 10^4\ J/mol \quad \text{Eq 2-24}$$

Figure 2-11 shows the most usual correlations, that have been compiled by Kammenzind [24]. All these calculations are close to each other.

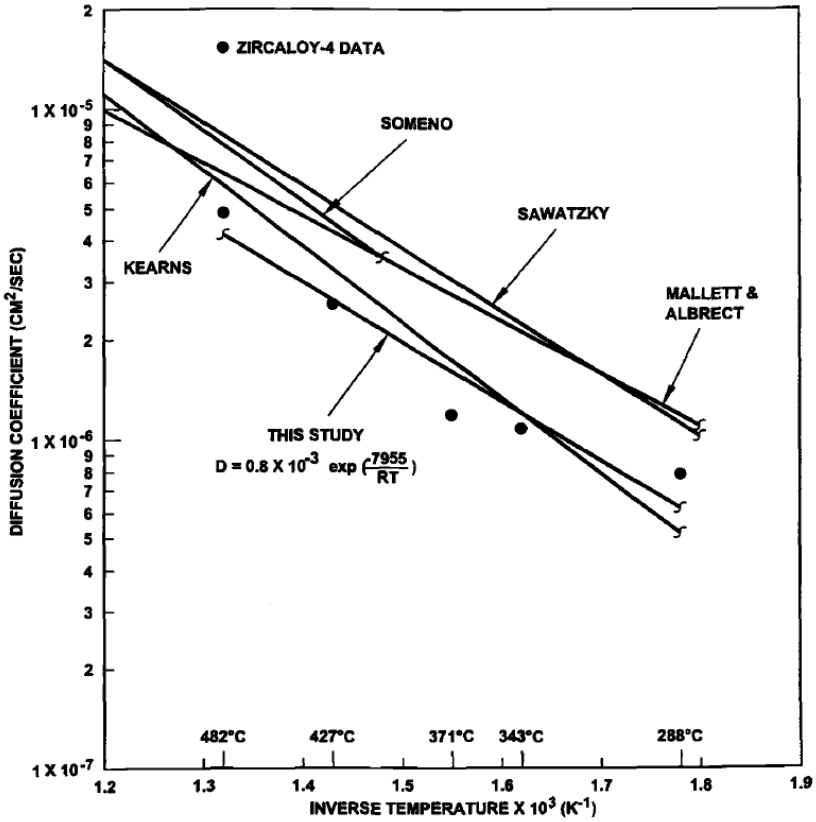

*Figure 2-11 Main measurement of hydrogen diffusion coefficient in Zircaloy-4.* [24]

### 2.4.3.2 Soret effect and heat of transport

As observed by Sawatzky and confirmed in several studies, hydrogen diffusion is also driven by a temperature gradient. According to the linear thermodynamic model [25], there is a coupling between thermal diffusion and species diffusion. The connection between a species diffusion flux and temperature gradient has different names. This phenomenon is called Soret effect (flux of particles induced by temperature gradient) or Dufour effect (heat flux induced by concentration gradient). The thermoelectric phenomena (Seebeck and Peltier effects) that govern the thermocouple laws are also described by the linear thermodynamics theory. This theory also includes the Onsager reciprocal relations. The fundamental assumption of this model is that there is a linear relation between the driving forces and the fluxes, as presented in Table 2-2.

*Table 2-2 Diffusion driving forces and fluxes*

| | **Driving force** | **Flux** |
|---|---|---|
| **Heat transfer** | $\nabla(\frac{1}{T})$ | $J_Q$ |
| **Species diffusion** | $-\frac{\nabla \mu_k}{T}$ | $J_D$ |

The proportionality between the driving forces and the fluxes is assumed. The proportionality coefficients are called $L_{XX}$ for direct relations and $L_{XY}$ for coupled relations. The following set of equations is obtained [25]:

$$\boldsymbol{J_D = L_{ii} * -\frac{\nabla \mu_k}{T} + L_{ij} * \ \nabla(\frac{1}{T})} \qquad \text{Eq 2-25}$$

$$\boldsymbol{J_Q = L_{jj} * -\nabla(\frac{1}{T}) + L_{ij} * \frac{\nabla \mu_k}{T}}$$

With $\mu_k$ the chemical potential of the species k,
$L_{ii}$ and $L_{jj}$ the direct proportionality coefficient (based on the linear approximation)
$L_{ij}$ and $L_{ji}$, the coupling proportionality coefficient
According to Onsager reciprocal relation:

$$\boldsymbol{L_{ij} = L_{ji}} \qquad \text{Eq 2-26}$$

This equality is a consequence of the symmetries of the equations. The full demonstration can be found on page 355 of *Modern Thermodynamics* [25].

According to the relationship between the activity and chemical potential for chemical species:

$$\mu_k(T) = \mu_0 + RTln(a_k) \quad \text{Eq 2-27}$$

With $a_k$ the activity of the species k.

For particle species in solution:

$$a_k = C_{ss} \quad \text{Eq 2-28}$$

With $C_{SS}$ the concentration in solid solution. Thus,

$$J_D = -L_{ii} * R * \frac{\nabla C_{ss}}{C_{ss}} + L_{ij} * \nabla(\frac{1}{T}) \quad \text{Eq 2-29}$$

Then, factorized by $L_{ii} * \frac{R}{C}$:

$$J_D = -L_{ii} * \frac{R}{C_{ss}}(\nabla C - \frac{L_{ij}}{L_{ii}} * \frac{C_{ss}}{R}\nabla(\frac{1}{T}) \quad \text{Eq 2-30}$$

The heat of transport is then defined as:

$$Q^* = \frac{L_{ij}}{L_{ii}} \quad \text{Eq 2-31}$$

Then,

$$J_D = -L_{ii} * \frac{R}{C_{ss}}(\nabla C - Q^* * \frac{C_{ss}}{R}\nabla(\frac{1}{T}) \quad \text{Eq 2-32}$$

By definition of the diffusion coefficient:

$$J_D = L_{ii} * \frac{R}{C_{ss}} \quad \text{Eq 2-33}$$

Then,

$$J_D = -D(\nabla C_{ss} + Q^* * \frac{C_{ss}}{RT^2}\nabla(T) \quad \text{Eq 2-34}$$

The first part of the equation corresponds to Fick's law. It can be observed that the temperature dependence of the diffusion coefficient does not appear in this equation. This is due to the fact that in the framework of the linear thermodynamics, the temperature dependence is assumed to be negligible. This assumption is approximately valid if the temperature does not vary excessively in the region of interest. The second part of the equation corresponds to the Soret effect:

$$J_{Soret} = -\frac{DC_{ss}Q^*}{RT^2}\nabla(T) \quad \text{Eq 2-35}$$

### 2.4.3.3 Consequences of the Soret effect

If the concentration of hydrogen in solid solution is low, there is no hydride precipitation (see section 2.4.4). In simple 1-D geometry, the analytical steady state solution can be calculated. Considering a plate exposed to two different temperatures ($T_{hot}$ and $T_{cold}$) on its two extremities and assuming adiabatic boundary condition on the other sides:


According to the conservation of mass,

$$\frac{dC_{ss}}{dt} = -\nabla J_D = \nabla[-D(\nabla C_{ss} + Q^* * \frac{C_{ss}}{RT^2}\nabla(T)] \quad \text{Eq 2-36}$$

The terms corresponding to the derivative of D with respect to x (or to T) are neglected. Assuming steady state and 1-D geometry, Equation 2-36 becomes:

$$\frac{d}{dx}[-D\left(\nabla C_{ss} + Q^* * \frac{C_{ss}}{RT^2}\nabla(T)\right] = 0 \quad \text{Eq 2-37}$$

Assuming no mass transfer at the cold and hot boundary:

$$-D\left(\frac{d}{dx}C_{ss} + Q^* * \frac{C_{ss}}{RT^2}\frac{d}{dx}T\right] = 0$$

$$\left(\frac{dC_{ss}}{dx} = -Q^*\frac{C_{ss}}{RT^2}\frac{dT}{dx}\right] \quad \text{Eq 2-38}$$

$$\left(\frac{dC_{ss}}{C_{ss}} = -Q^*\frac{dT}{RT^2}\right]$$

Integrating between x=0 and x:

$$\ln(C_{ss}) - \ln(C_0) = -Q^*(\frac{1}{RT} - \frac{1}{RT_0}) \quad \text{Eq 2-39}$$

$$C_{ss} = K_{int} * \exp(\frac{Q^*}{RT}) \quad \text{Eq 2-40}$$

The integration constant $K_{int}$ can be calculated using the conservation of mass and the initial average concentration:

$$\int C_{ss}dx = cst \quad \text{Eq 2-41}$$

The transient calculation, using series expansion, has been performed by Sawatzky and Vogt [26]. This complex calculation has not been reproduced in this thesis. The first part of the publication gives the transient of the case presented above. The second part, however, tries to model the two-phase equilibrium and has to be considered carefully.

### 2.4.4 Hydride precipitation and dissolution (TSS laws)

When the hydrogen content reaches the solubility limit in the α-zirconium matrix, the hydrogen precipitates as zirconium hydride. This limit is called the Terminal Solid Solubility (TSS) [27]. The determination of the TSS is essential for a better understanding of the behavior of zirconium hydrides. Kearns' study on the terminal solubility limit using the diffusion couple method has been widely used as the reference for TSS determination [28]. This study states that below 550ºC (above which recrystallization occurs), the following equation determines the TSS:

$$TSS(\text{wt. ppm}) = 120000\ exp(-\frac{4302}{T}) \quad \text{Eq 2-42}$$

where T is the temperature in Kelvin.

A hysteresis phenomenon has been observed in several studies between the TSS for dissolution (TSSd) and the TSS for precipitation (TSSp). This temperature hysteresis is a result of the work associated with volume expansion which is required for hydride precipitation, as illustrated in Figure 2-12. When a small plate-shaped hydride precipitate is nucleated, reversible elastic work is done on the surrounding matrix, yielding the following expression for the nucleation solvus [29][30]:

$$C_{nucl} = C_s \exp\left(\frac{w_e}{RT}\right) \quad \text{Eq 2-43}$$

where $C_{nucl}$ is the amount of hydrogen in solution until hydride precipitation, $C_S$ is a theoretical "stress-free" or equilibrium solvus, $w_e$ is the elastic accommodation energy of the matrix and hydride precipitate per mole hydrogen (which is influenced by the orientation relationship of the precipitate and the matrix), and T is the temperature. Because the hydride is performing work on the matrix as it precipitates, the hydrogen concentration in the matrix is elevated relative to the equilibrium solvus $C_S$. When a hydride grows past a critical size (typically sub-micron [31][32]), the accommodation energy is no longer purely elastic and the expression must account for plastic accommodation of the hydride [33] :

$$C_{cool} = C_s \exp\left(\frac{w_{e,p} + w_P}{RT}\right) = C_s \exp\left(\frac{Q_{cool}}{RT}\right) \quad \text{Eq 2-44}$$

where $w_P$ is the plastic accommodation energy, $w_{e,p}$ is the elastic contribution in the presence of plastic deformation, and $Q_{cool}$ represents the total accommodation energy upon cooling. The solvus expression for hydride dissolution, $C_{Heat}$, is similar to that of precipitation, the difference being the plastic work required to precipitate the hydride is not reversible (and therefore the contribution from $w_p$ is negligible on heating):

$$C_{heat} = C_s \exp\left(\frac{w_{e,p} + w_P}{RT}\right) = C_s \exp\left(\frac{Q_{heat}}{RT}\right) \quad \text{Eq 2-45}$$

In the case of zirconium, it is the plastic work term that dominates during cooling and for this reason the hydrogen concentration on dissolution $C_{heat}$ is often approximated as $C_S$. It should also be noted that the hydrogen concentration on precipitation $C_{cool}$ is not unique and is affected by the previous thermo-mechanical history of a specimen [29][30][34].

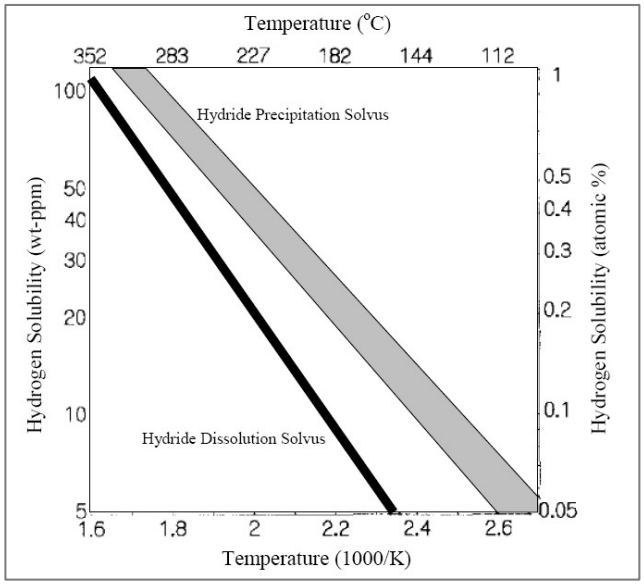


*Figure 2-12 Illustration of the precipitation hysteresis.* [34]

According to McMinn [35] and without any additional effects, the TSSd and the TSSp can be approximated by the following equations:

$$TSSd = 106466.7 * \exp(-\frac{4328.67}{T}) \qquad Eq\ 2\text{-}46$$

$$TSSp = 138746.0 * \exp(-\frac{4145.72}{T})$$

In addition to temperature, the main factors that influence hydride dissolution and precipitation in zirconium and its alloys are:

a) Irradiation;

b) Oxygen in solid solution;

c) Alloying elements;

d) Thermal cycles.

### 2.4.5 Hydride precipitation and dissolution (TSS laws)

#### 2.4.5.1 Necessity of the precipitation kinetics understanding

The kinetics of precipitation is a critical aspect of hydrogen redistribution in the cladding. While the TSSp and TSSd give the equilibrium value between the hydrogen in solid solution and in the precipitated hydrides, the kinetics provide information regarding the transient behavior between a non-equilibrated initial condition and the final steady state equilibrium. The detailed kinetics of hydride precipitation is likely one of the main causes of the rim feature and specific hydrogen distributions that occur in the nuclear fuel cladding. Because the kinetics are difficult to model, in his initial work, Sawatzky tried to explain the hydride redistribution without taking the kinetics into account [36].

However, he considered an initial homogeneous concentration of zirconium and applied a temperature gradient. Then, he observed a local increase of the hydride concentration that looks like a rim, but

is completely different from the rim that is seen in reactor condition. It can, however, be considered in calculations for dry-cask storage.

In the case of reactor operation, the initial concentration of hydrogen starts at about 0 wt. ppm. The cladding is submitted to a temperature gradient of about 40°C for a thickness of 0.6 mm. The hydrogen flux is coming from the coolant interface, as shown below:

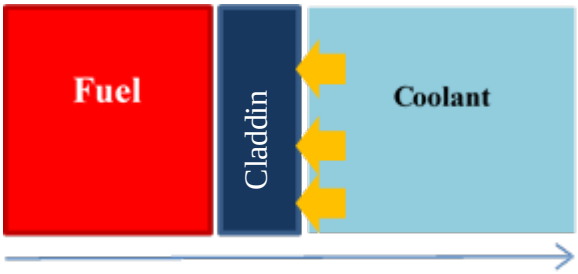


*Figure 2-13 Hydrogen boundary condition schematic.*

As already noticed by Shewmon [37], it is impossible to predict the redistribution solely from the diffusion laws and the Terminal Solid Solubility. Indeed, as long as the hydrogen concentration does not reach the TSSp, the equilibrium will be established in a quasi-steady-state manner, with a solution close to the one explained in section 2.4.3.3. It means that the highest concentration of hydrogen will occur in the colder area, which is the coolant/cladding interface.

Moreover, the TSSp decreases when the temperature decreases. Therefore, the lowest temperature area also has the lowest TSSp. Thus, the point where hydrogen reaches the TSSp first is at the cladding/coolant interface. If instantaneous precipitation is assumed, there is no reason for the hydrogen to diffuse into the cladding. It will precipitate instantaneously upon entry into the cladding. This would however lead to the formation of a solid hydride, and it is not what is observed (see section 2.4.2.1). Therefore, the role of precipitation kinetics needs to be examined. This precipitation will explain why hydrogen can diffuse into the cladding. If all the hydrogen in solid solution does not precipitate instantaneously, it remains supersaturated in the solid state. In that case, the previous diffusion equilibrium is modified and hydrogen diffuses toward the fuel/cladding interface.

### 2.4.5.2 Model of precipitation kinetics developed by Marino

This section follows the model developed by Marino [38][39]. In his papers, he proposed a precipitation rate proportional to the difference between supersaturated hydrogen in solid solution concentration $C_{ss}$ and the equilibrium value (given by the TSSp):

$$\frac{dC_{ss}}{dt} = -\alpha^2(C_{ss} - TSSp) \qquad \text{Eq 2-47}$$

The kinetics parameter $\alpha^2$ has been studied by Kammenzind, who measured it in his experiment and proposed an Arrhenius law to describe its dependence on temperature [24]. Figure 2-14 shows Kammenzind's measurements and the linear interpolation of his data. The value of α is plotted against the inverse of the temperature (in Kelvin).

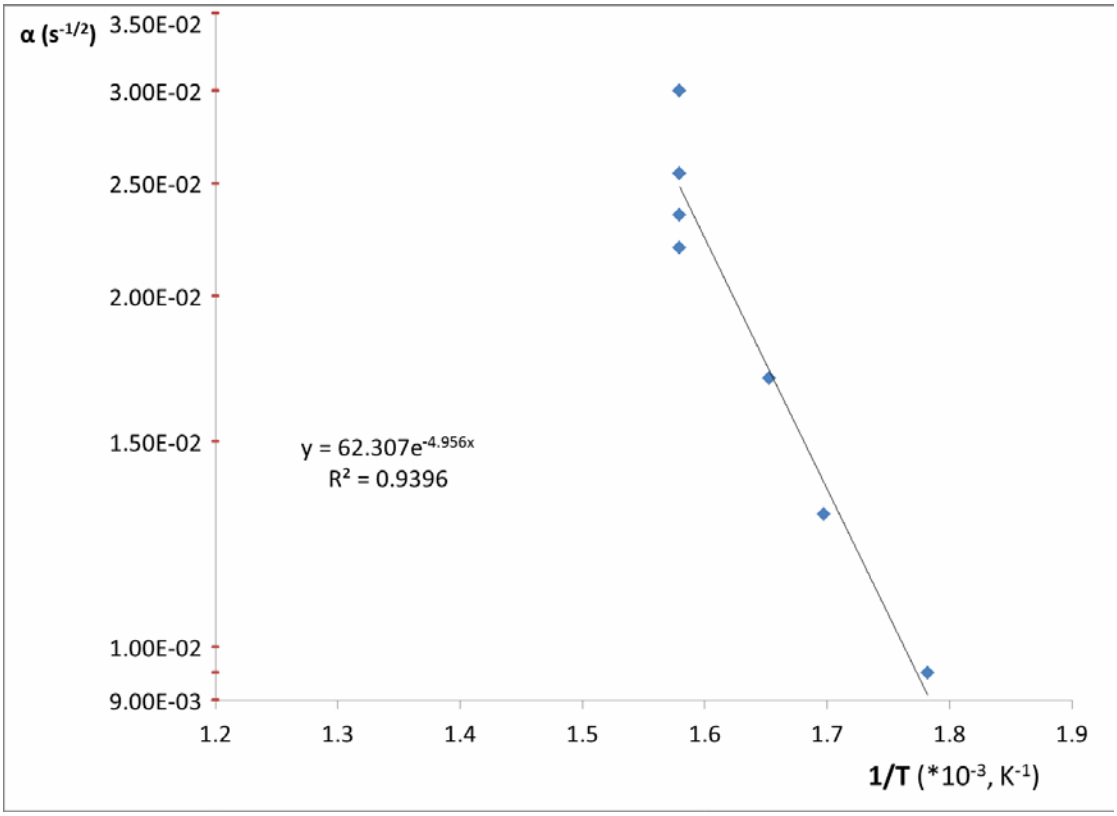


*Figure 2-14 Kammenzind measurement of the rate of precipitation as a function of temperature.*

The equation found for the kinetics parameter is:

$$\boldsymbol{\alpha = A_\alpha * exp(-\frac{Q_\alpha}{RT})} \qquad \textbf{\textit{Eq 2-48}}$$

With $A_\alpha \approx 62.3\ s^{1/2}$ and $Q_\alpha = 4.12810^4 J$

### 2.4.6 Summary of the balance equations governing hydrogen concentration

From the precipitation, dissolution and diffusion model explained in the previous sections, the balance equation for hydrogen in solid solution and hydride concentration can be deduced. The variation of hydrogen in solid solution per unit of time is given by the sum of the net flux, the hydrogen created by the dissolution of hydride minus the hydrogen transformed into hydride due to precipitation.
Based on the Sawatzky diffusion model given by Eq 2-34, the diffusion flux is equal to:

$$\boldsymbol{J_D = (-D\nabla C_{ss} - \frac{DC_{ss}Q^*}{RT^2}\nabla(T)} \qquad \text{Eq 2-49}$$

Hydride precipitation occurs when the $C_{SS}$ surpasses the TSSp. Hydride dissolution occurs when the $C_{SS}$ becomes lower than the TSSd. The TSSp and TSSd values measured by McMinn [40] have been used for the current work. Recalling equation 2-46:

$$TSSd = 106466.7 * \exp(-\frac{4328.67}{T}) \qquad \textit{Eq 2-50}$$
$$TSSp = 138746.0 * \exp(-\frac{4145.72}{T})$$

According to Marino's equation Eq 2-47, the rate of precipitation (in wt.ppm/s) is given by:

$$\boldsymbol{R_{precipitation} = -\alpha^2(C_{ss} - TSSp)} \qquad \textit{Eq 2-51}$$

The dissolution is assumed instantaneous by most authors and is assumed here. In order to simplify our future calculations, we assume a linear law for the dissolution, with a characteristic time very small compared to the precipitation characteristic time:

$$\boldsymbol{R_{dissolution} = \beta^2(C_{ss} - TSSp)} \qquad \text{Eq 2-52}$$

*Note*: $\beta \gg \alpha,\ \beta \gg \frac{l^2}{D}$

The diffusion coefficient is calculated using Kearns' correlation [23]

$$\boldsymbol{D = A_{diff} * \exp\left(-\frac{Q_{Diff}}{RT}\right)} \qquad \text{Eq 2-53}$$

Four different cases have to be taken into account for the writing of the balance equations.

In the first case, the concentration of hydrogen in solid solution is greater than the TSSp. Then, precipitation occurs according to the laws described above.

- Precipitation:

$$\boldsymbol{if\ C_{ss} > TSSp,} \begin{cases} \boldsymbol{\frac{dC_{ss}}{dt} = -\nabla J - \alpha^2(C_{ss} - TSSp)} \\ \boldsymbol{\frac{dC_p}{dt} = \alpha^2(C_{ss} - TSSp)} \end{cases} \qquad \text{Eq 2-54}$$

In the second case, the concentration in solid solution is between the TSSp and the TSSd. This is the "hysteresis" area, where neither diffusion nor precipitation occurs.

- Hysteresis:

$$\boldsymbol{if\ TSSp \geq C_{ss} > TSSd,} \begin{cases} \boldsymbol{\frac{dC_{ss}}{dt} = -\nabla J} \\ \boldsymbol{\frac{dC_p}{dt} = 0} \end{cases} \qquad \text{Eq 2-55}$$

In the third case, the concentration in solid solution is below the TSSd. The hydrogen in the precipitated hydrides ($C_P$) is dissolving so that the $C_{SS}$ matches the TSSd value. This is possible only if there are hydrides ($C_P>0$).

- Dissolution:

$$\boldsymbol{if\ TSSd \le C_{ss}\ and\ C_p > 0\ and\ \nabla J > 0}\ , \begin{cases} \dfrac{dC_{ss}}{dt} = -\nabla J + \beta^2(TSSd - C_{ss}) \\ \dfrac{dC_p}{dt} = -\beta^2(TSSd - C_{ss}) \end{cases} \quad \text{Eq 2-56}$$

In the fourth and last case, the concentration in solid solution is below the TSSd but there are no more hydrides to dissolve. In that case, the only change to hydrogen concentration comes from net diffusion flux.

- Diffusion only:

$$\boldsymbol{if\ \ TSSd \ge C_{ss}\ and\ C_p = 0},\quad \begin{cases} \dfrac{dC_{ss}}{dt} = -\nabla J \\ \dfrac{dC_p}{dt} = 0 \end{cases} \quad \text{Eq 2-57}$$

The model constants have been taken from the literature and are summarized in Table 2-3.

*Table 2-3 Hydrogen model constants*

| **Phenomenon** | **Parameter** | **Value** | **Unit** | **Source** | **Comments** |
|---|---|---|---|---|---|
| Fick's law | $A_{Dff}$ | $7.90*10^{-7}$ | $m^2/s$ | [41] | Longitudinal diffusion |
| | $Q_{Diff}$ | $4.49*10^{4}$ | J/mol | [41] | Longitudinal diffusion |
| Soret effect | $Q^*$ | $2.51*10^{4}$ | J/mol/K | [24] | Average value |
| Precipitation | $A_P$ | $1.39*10^{5}$ | wt. ppm | [40] | Unirradiated |
| | $Q_P$ | $3.45*10^{4}$ | J/mol | [40] | Unirradiated |
| Dissolution | $A_D$ | $1.06*10^{5}$ | wt. ppm | [40] | Unirradiated |
| | $Q_D$ | $3.60*10^{4}$ | J/mol | [40] | Unirradiated |
| Precipitation kinetics | $A_\alpha$ | $6.23*10^{1}$ | $s^{1/2}$ | [24] | |
| | $Q_\alpha$ | $4.12*10^{4}$ | J/mol | [24] | |

# 3 Experimental Design for hydrogen model validation

## 3.1 Design and performance of targeted model experiments to determine Q* and α2

### 3.1.1 Q* experiment by Olivier

#### 3.1.1.1 Scattered previous measurements of the heat of transport

Previous measurements of the heat of transport (Q*), for hydrogen in Zircaloy-4, show significant dispersion among measured values. These measurements were gathered and presented by Menibus in his thesis [41], and his table is reproduced in Table 3-1. Figure 3-1 shows the average value of each experiment against the temperature range that is used. All the measurements follow similar procedures. A zirconium (or Zircaloy) plate is initially charged with hydrogen. Then the plate is submitted to a constant temperature gradient over a long-time period. At the end of the experiment, the hydrogen distribution is assumed to have a steady state profile. In some experiments (as in the one made by Jovanovic [42]), the initial concentration of hydrogen is chosen to avoid any precipitation in the sample. In others, (e.g. Hong [43]) precipitation is observed. In the second case, the results, analysis and the calculation of Q* are more complicated because hydride precipitation affects hydrogen distribution.

*Table 3-1 Summary of heat of transport of hydrogen in Zircaloy measurements.*

| **Material** | **Temperature (°C)** | **H (wt.ppm)** | **Q* (kJ/mol)** | **# of exp.** | **Source** | **ΔT / Δx (°C/cm)** |
|---|---|---|---|---|---|---|
| Zr-α | 300-500 | 60 | 24.7 ± 0.6 | 2 | Sawatzky [44] | 167 |
| | 350-400 | <55 | 29.5 ± 0.7 | 2 | Sugiaski [45] | n/a |
| | 200-480 | 10 | 22.2 | 1 | Morozumi [46] | 175 |
| | 350-560 | 55 | 11+0.026 T | 11 | Hashizume [47] | 137, 150 |
| Zircaloy-2 | 295-450 | 300 | 14.2 | 1 | Markowitz [48] | n/a |
| | 300-500 | 60 | 22.6 ±4.2 | 2 | Sawatzky [26] | 167 |
| Zircaloy-4 | 260-648 | 46-250 | 26.9 ± 5.4 | 11 | Kammenzind [24] | 66, 87 |
| | 300-340 | 60 | 28.1 | 1 | Hong [43] | 13 |
| Zr-α-1%Nb | 200-480 | 10 | 24.7 | 1 | Morozumi [46] | 175 |
| Zr-α-2.6%Nb | 300-500 | 68 | 23.4 ± 1.8 | 2 | Sawatzky [44] | 163 |
| Zr-α-2.5%Nb | 240-500 | 28-108 | 19.3 ± 1.8 | 8 | Jovanovic [42] | 43, 47, 50 |

| | | | | | | |
|---|---|---|---|---|---|---|
| Zircaloy-2 / Deuterium | 300-500 | 120 | 27.2 ± 1.8 | 2 | Sawatzky [44] | 133 |
| Zr-Tritium | 250-350 | <55 | 24.3 ± 2 | 3 | Sugiaski [45] | n/a |

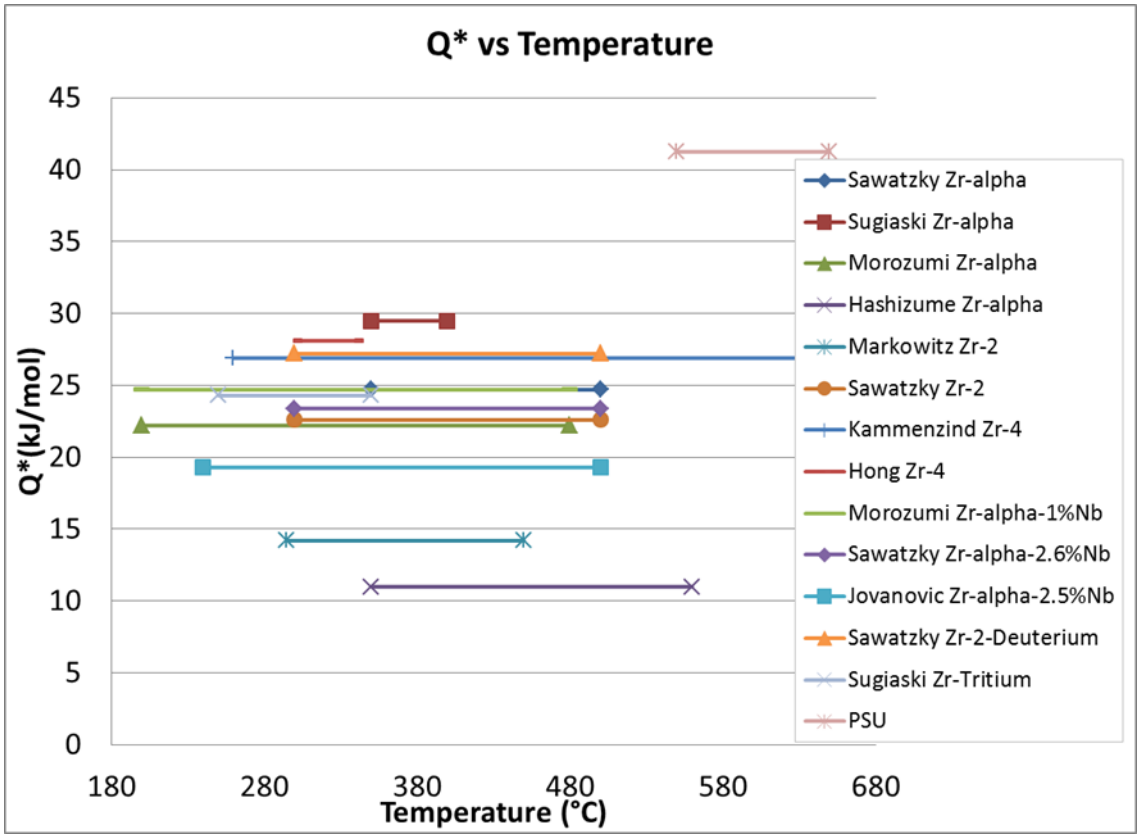


*Figure 3-1 Measurement of Q* with respect to the temperature.*

Only two studies are devoted to Zircaloy-4. The Kammenzind's study shows a variation of the heat of transport with the temperature, but also with the gradient applied. However, no clear law seems to be deducible from his measurements [49]. Figure 3-2 shows the measured values of Q* versus the inverse of the absolute temperature. Kammenzind's experimental results show a high dispersion. Regarding Hong's measurement, its correlation includes a two phase area, which should be driven by the TSSp equilibrium and not by the Soret-Fick equilibrium. This approximation may affect the calculation. Nevertheless, none of the Zircaloy-4 measurements give conclusive results. Since this parameter is critical in the diffusion model and that it cannot be calculated, an experiment was designed to measure the value of Q*.

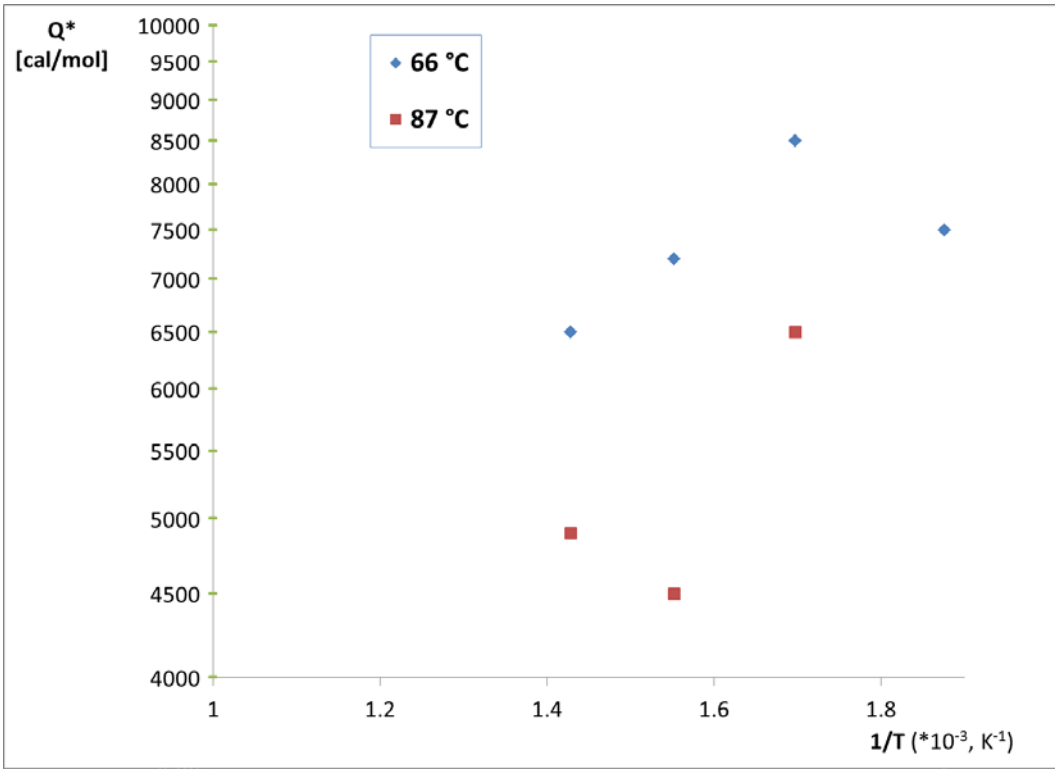


*Figure 3-2 Heat of transport measured by Kammenzind.*

### 3.1.1.2 Experimental design for measurement of Q*

The experiment was designed[1] to observe the redistribution of hydrogen under a temperature gradient in the absence of precipitation, as done by Jovanovic et al. but not by Hong [42][43]. In this case, the steady state equilibrium hydrogen concentration in solid solution is given by:

$$C_{ss}(x) = C_0 * \exp\left(\frac{Q^*}{RT}\right) \qquad \textit{Eq 3-1}$$

The sample chosen for the study is a Zircaloy-4 plate, measuring 1cm x 3.4cm x 0.06cm. The sample is stacked between two stainless steel holders, as shown in Figure 3-3.

[1] *The experiment was designed with the help of Daniel Nunez, undergraduate student and summer intern at the Pennsylvania State University, within the framework of the Toshiba-Westinghouse Fellows Program.*

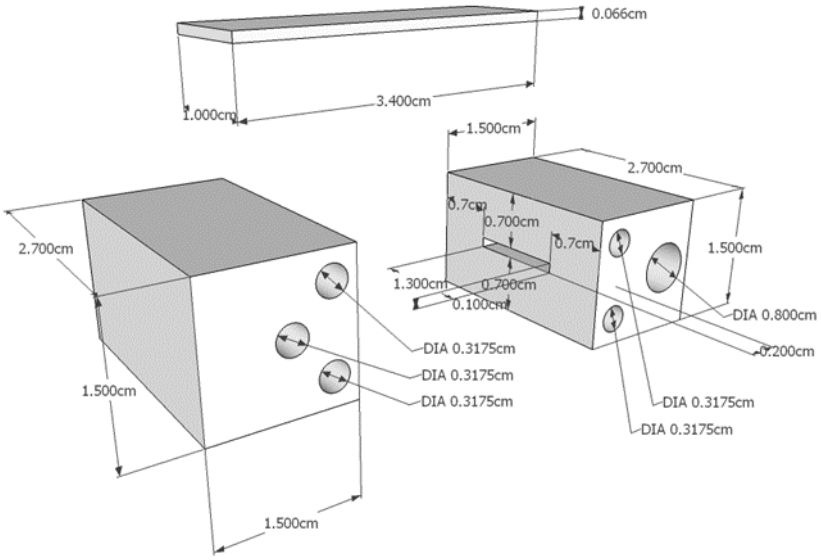


*Figure 3-3 3-D view of the 304 stainless steel holders and the Zircaloy-4 plate sample.*

The holder with 3 small holes is heated to the higher temperature and the second one is one heated to a lower temperature. The plate is inserted about 2 mm into the slot in each holder, which means that the experimentally usable section of the sample is 3 cm long. The holders were heated with silicon carbide surface igniters [50]. These igniters can reach a temperature greater than 1000°C, and allow obtaining high temperatures in a localized spot. The igniters are placed on the outside of the holders, as shown in Figure 3-4.

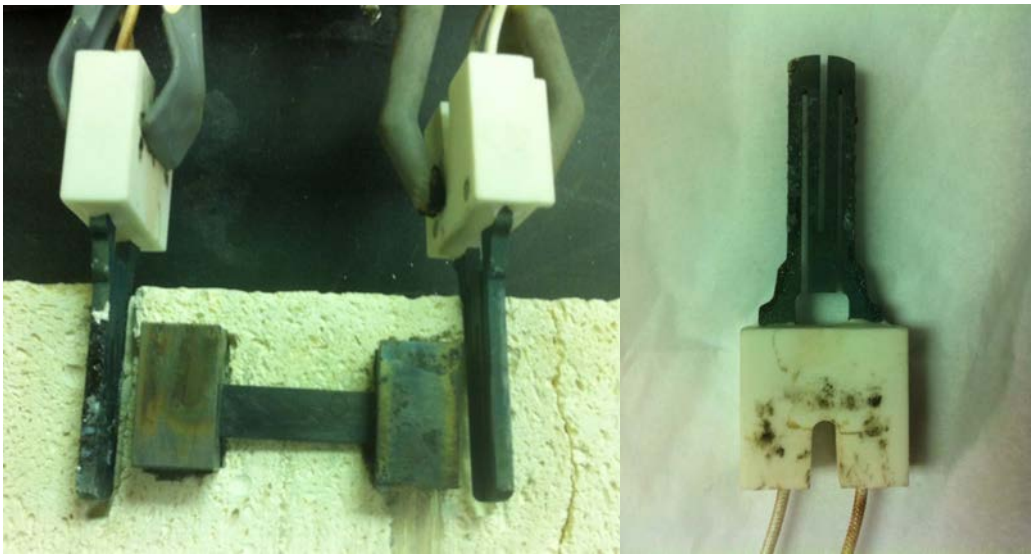

*Figure 3-4 Heaters, holders, and samples in the heat of transport experiment.*

The 0.3175 cm holes drilled into both of the heaters were to be used for heat cartridges. Because of systematic failures of the Omega ® cartridge heaters at 400°C, these holes are no longer used in the current design. The heat cartridges have been replaced by surface igniters. Both of the silicon carbide igniters are controlled with Benchtop Temperature Controllers. Figure 3-5 and Table 3-2 below show the front and back view of the controllers, and their main specifications.

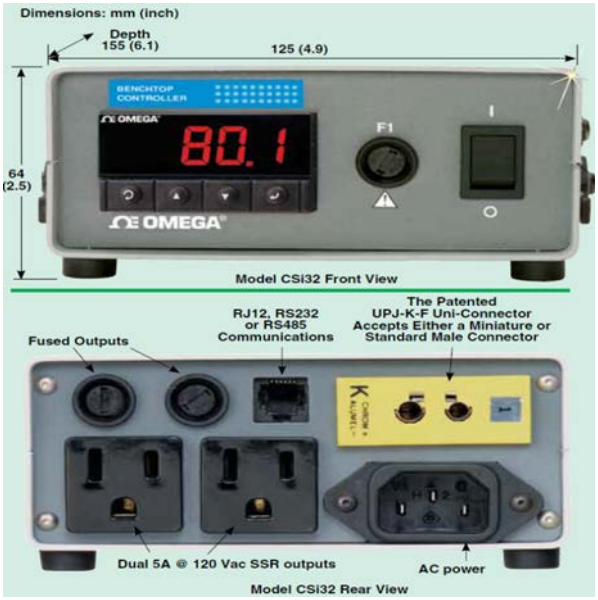


*Figure 3-5 Temperature controller front and back view.*

*Table 3-2 Temperature controller specifications.*

| ***Specification*** | ***Value*** |
|---|---|
| **Resolution:** | 1°/0.1°; 10 μV process |
| **Temperature Stability:** | RTD: 0.04°C/°C |
| **Reading Rate:** | 3 samples per second |
| **Display:** | 4-digit, 9-segment LED; |
| **Input Types** | Thermocouple, RTD, analog voltage, analog current |
| **Thermocouple Lead Resistance** | 100 Ω (max) |
| **Digital Filter:** | Programmable |

These controllers are configured in a Proportional-Integral-Derivative mode. The controlled temperature is given by a type-K thermocouple, attached to the extremity of the plate (But not in the holder). Figure 3-6 shows the control loop pattern.

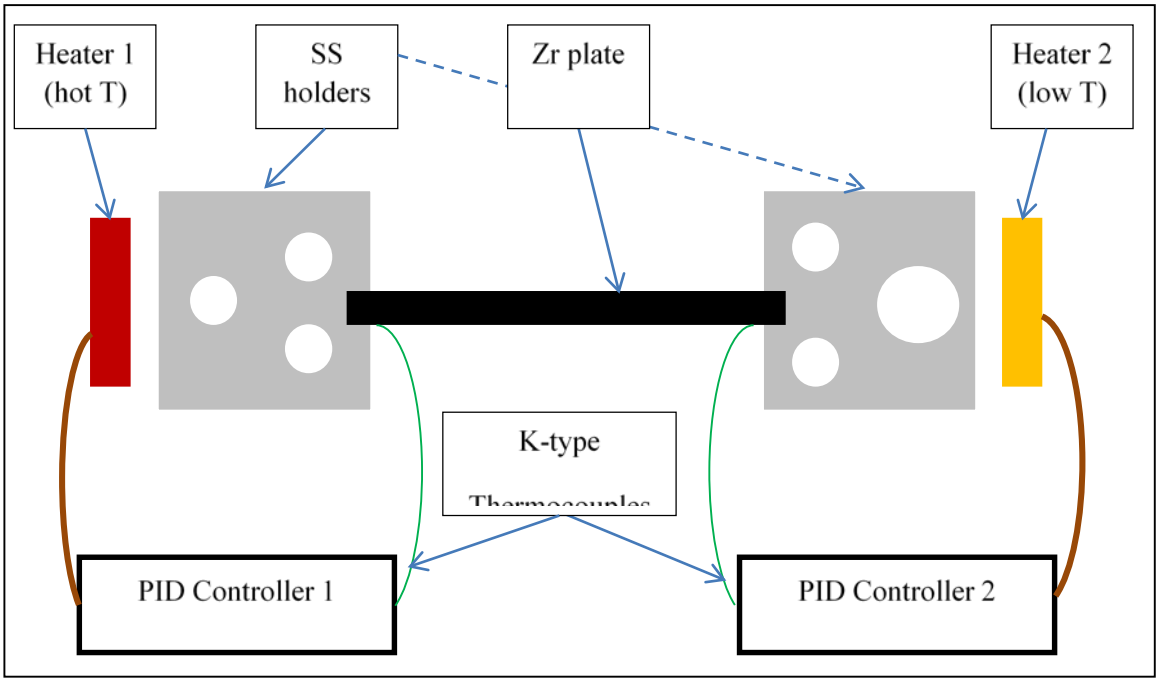


*Figure 3-6 Schematic of temperature control for the diffusion experiment.*

The PID values have been chosen using a manual configuration. Table 3-3 reproduces the values chosen.

*Table 3-3 PID values of the thermal controllers.*

| Parameter | PID controller 1 | PID controller 2 |
|---|---|---|
| P | 50 | 300 |
| I | 100 | 150 |
| D | 6.0 | 25 |

Since there is a heat transfer from the hot side to the cool side of the plate, a thermal flux is created toward the "cool" holder, where the heat is removed using an air cooling system connected to this holder. The air flow is controlled by a regulator (Figure 3-7). Air is blown through a glass tube into the main hole of the second holder (Figure 3-8). However, due to heat loss caused by natural convection, this system is not used in most of the experiments.

*Figure 3-7 Air flow regulator.*

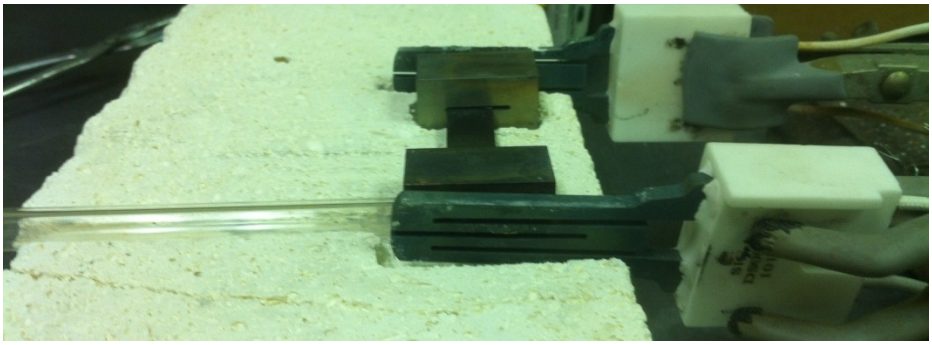

*Figure 3-8 Connection between the air tube and the holder.*

In order to minimize heat losses, two different types of insulation have been installed. First, the entire setup (holder, heating elements, sample and thermocouples) is contained within two insulating bricks. Second, insulation blankets are used to wrap the sample to provide additional thermal insulation. The design of the insulation is shown in Figure 3-9. A second brick covers the experiment.

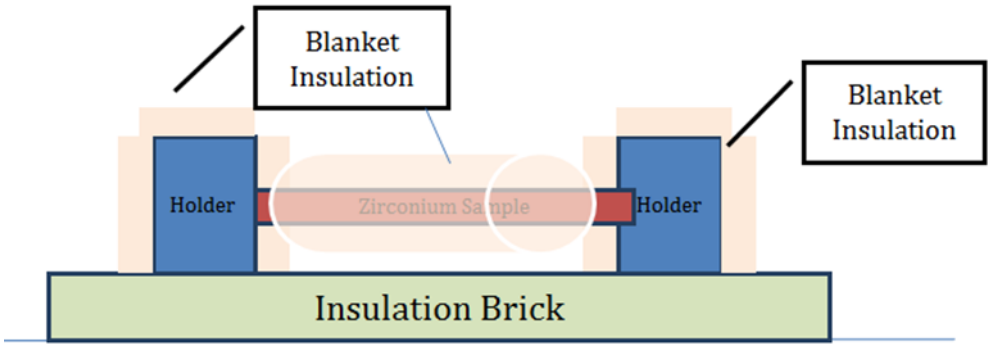


*Figure 3-9 Design of the insulation of the experiment.*

Once the second brick covers the experimental set up and the specimen is at temperature, the temperature measured outside of the experimental setting is smaller than 25 °C (for a room temperature of 20°C). This indicates a small heat loss and good thermal insulation.

The temperature profile was measured nonlinear in the sample, using a thermocouple in the middle of the plate. This indicates the presence of temperature losses. After several attempts, it was not possible to obtain a linear gradient. Nevertheless, the steady state hydrogen concentration profile is expressed as a function of temperature. Therefore, by knowing the temperature profile, the hydrogen concentration profile can be calculated. In order to accurately obtain the steady state temperature profile, 5 thermocouples have been attached to the plate, as shown in Figure 3-10.

*Figure 3-10 Thermocouples on the sample.*

#### 3.1.1.3 Sample preparation

The preparation of the samples requires the following steps.

a) Since the sample is exposed to high temperature (~ 500-700°C), the sample may recrystallize. To avoid change to the microstructure during the experiment, the sample is subject to a recrystallization heat treatment before the experiment starts;
b) To prevent oxidation, the samples are coated with a deposited 100 nm layer of Nickel;
c) Hydrogen is put into the sample using to the hydrogen charging equipment at PSU.

#### 3.1.1.4 Experimental procedure

In a first attempt, the experiment was run with a 750°C-650°C temperature difference. The sample had been charged with an initial concentration of 1000 wt. ppm. After 40 hours, the experiment was stopped and the sample quenched. Unfortunately, the sample broke during the experiment as shown in Figure 3-11. On the hot side, almost 20% of the sample was destroyed and transformed into oxide dust. Moreover, the sample was significantly bent. The sample failure is probably due to a strong oxidation and a low yield stress that have allowed plastic deformation. The high oxidation rate due to high temperature and issues with the Ni coating probably leads to the formation of a “destructive” oxide layer. Then, at high temperature, the yield stress is significantly lower and thus allows plastic deformation.

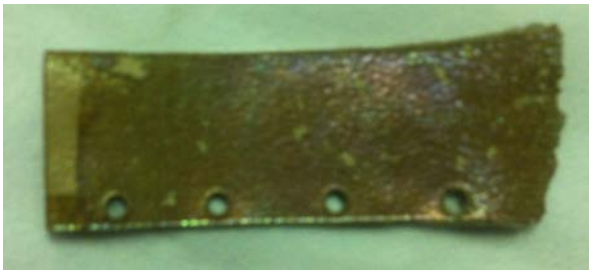

*Figure 3-11 Sample damaged after 750°-650° experiment.*

In order to prevent these phenomena, a new run with a lower gradient (650°C-550°C) was performed. In this case, the initial concentration has to be 650 wt. ppm in order to prevent hydride precipitation. The hydrogen charging does not allow a precise concentration. The hydrogen concentration has been measured after the charging and was equal to 709°C wt.ppm. Therefore, the temperatures conditions were moved to 660°C-560°C to avoid precipitation. During preliminary tests, the temperature profile has been measured to estimate the heat loss. Assuming a constant linear heat loss, and using a sample length l=3 cm:

$$T(x) = \frac{q}{2k} * x^2 - \frac{q}{2k} l * x + T_{maxi} \qquad \text{Eq 3-2}$$

Where q is the linear heat loss, k is the thermal conductivity and $T_{maxi}$ is the temperature at the hot end. It has been determined experimentally that $\frac{q}{2k} = 27K.cm^{-2}$.

The steady state profile hydrogen profile (and the TSSp) obtained for this temperature profile are given in Figure 3-12. The steady state profile confirms the fact that there should not be any precipitation. In order to perform the calculation, the value heat of transport was assumed equal to $2.51 * 10^4\ J/mol$. This average value comes from Kammenzind work [51].

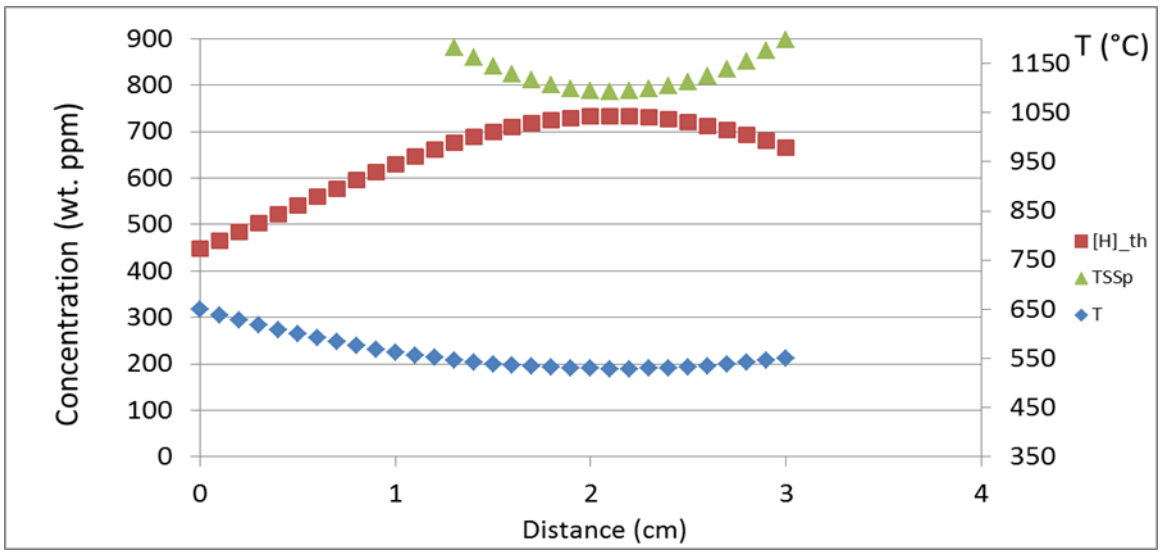


*Figure 3-12 Temperature and hydrogen steady state profile under 650°-550° gradient.*

To perform the experiment, dissolution of all the hydrides is required. To dissolve the hydrides, it is necessary to heat up the sample to a temperature higher than the dissolution TSS (TSSd) in the sample before applying the temperature gradient. Assuming the same quadratic profile, a temperature of 680°C applied at each side of the sample is necessary. According to a steady state calculation, the

application of this temperature to the sample implies a full dissolution of the hydrogen, as shown in Figure 3-13.

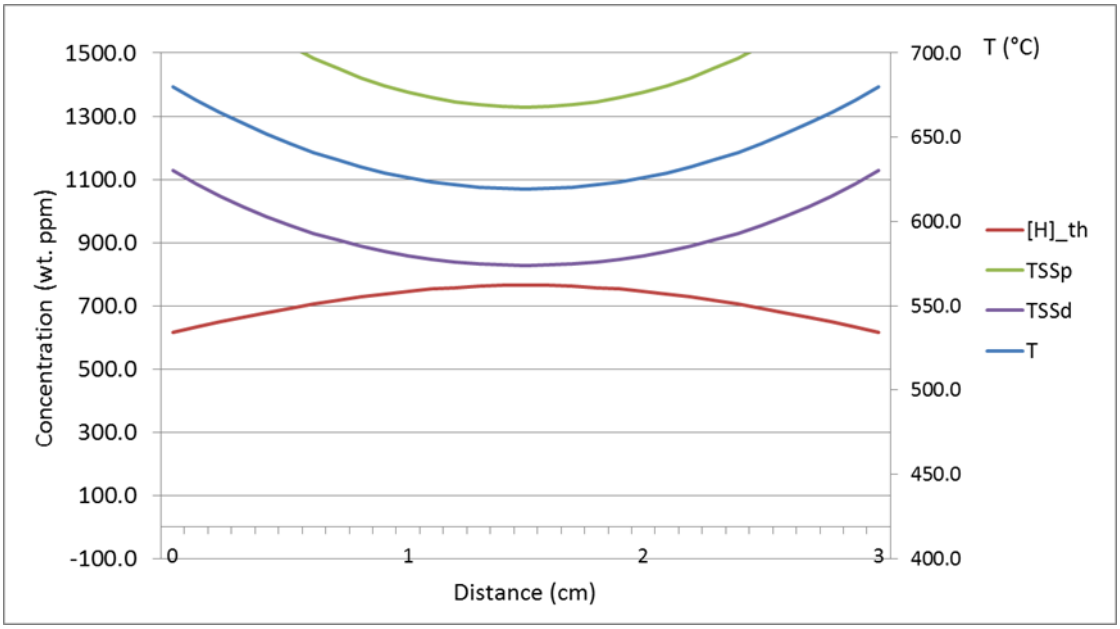


*Figure 3-13 Hydrogen profile before starting 660°C-560°C gradient experiment.*

After the dissolution step, the 660°C-560°C gradient has been applied. Using the HydruLab code developed in the frame of this project, the transient profile has been calculated, assuming an initial constant hydrogen profile. The transient profiles are represented on Figure 3-14 and Figure 3-15 for hydrogen in solid solution and hydrides respectively. Each line represents 10 hours. Table 3-4 shows a numerical estimation of the difference between the steady state profile and each transient profile, by calculating the maximum, minimum and average difference of the 200 mesh points. Considering that the uncertainty of the hydrogen measurement is 20 wt.ppm, it can be concluded that after 60 hours, the transient is sufficiently close to the steady state (with a difference of about 5 wt. ppm).

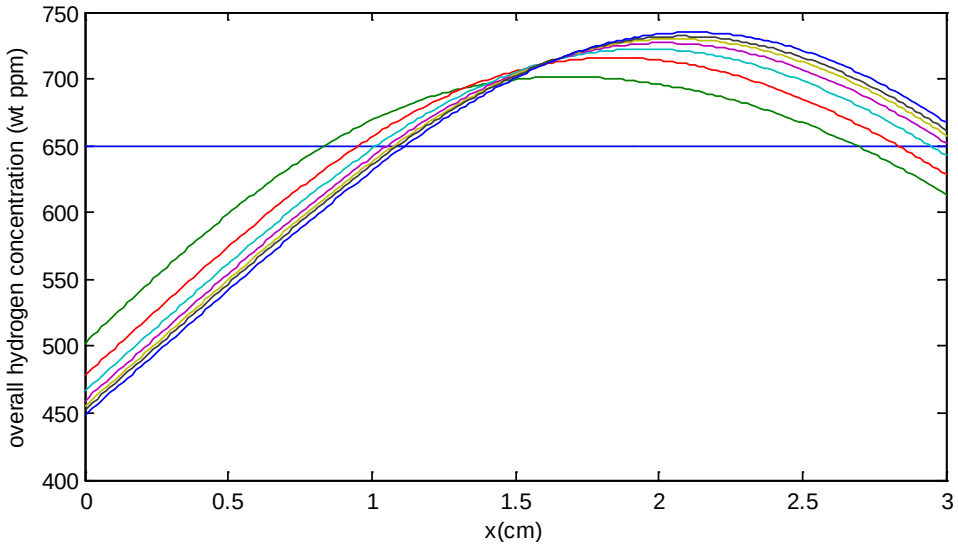


Figure 3-14: Kinetics of the concentration profile (one line per 10 hours) with a 650°-550°C gradient

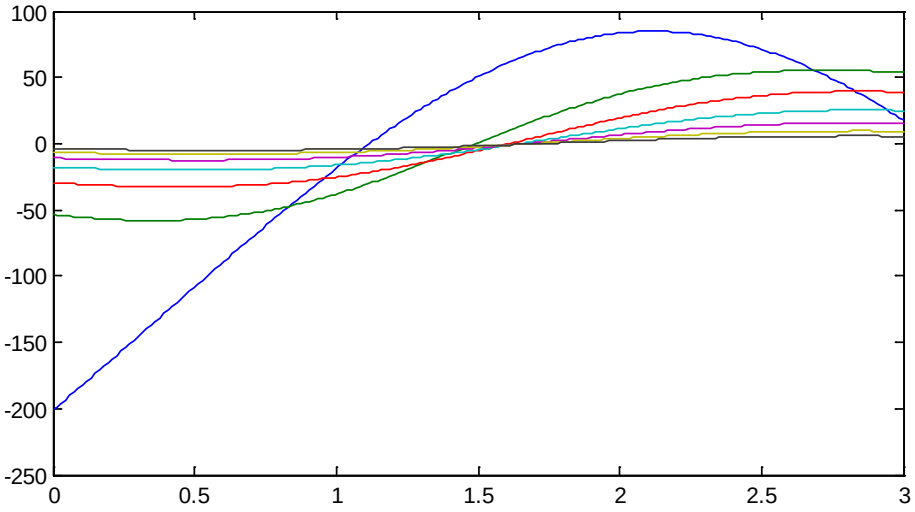


*Figure 3-15: Difference with steady state (one line per 10 hours) with a 650°-550°C gradient.*

*Table 3-4 Estimators of the difference between transient and steady state profile (650°C-550°C).*

| time (h) | average difference with SS | maximum difference with steady state | minimum difference with steady state | standard deviation |
|---|---|---|---|---|
| **0.0** | 198.8 | 84.8 | -200.6 | 86.3 |
| **10.0** | 53.9 | 55.5 | -58.0 | 44.9 |
| **20.0** | 29.6 | 39.5 | -32.6 | 27.9 |
| **30.0** | 17.8 | 25.3 | -19.9 | 17.4 |
| **40.0** | 10.9 | 15.7 | -12.4 | 10.8 |
| **50.0** | 6.7 | 9.6 | -7.8 | 6.7 |
| **60.0** | 4.1 | 5.7 | -4.9 | 4.1 |

Figure 3-16 shows the sample after 60 hours. There is some oxidation on the surface, but it is mostly a black protective layer. After measurement of the oxygen content, the oxide layer is thinner than 20 microns.

*Figure 3-16: Sample after 660°C-560°C experiment.*

### 3.1.1.5 Results of the heat of transport experiment.

The temperature profile has been measured during the experiment at five different locations on the plate. The temperature was measured constant during the 60 hours of the experiment. Table 3-5 provides the temperatures and the locations of these thermocouples. The length of the sample in which

analysis is judged to be reliable, goes from the first to the last thermocouple, which corresponds to a length of 2.6 cm

*Table 3-5 Temperature in the plate during the diffusion experiment.*

| Location of the thermocouple | Temperature (°C) |
|---|---|
| 0.4 | 550 |
| 1 | 567 |
| 1.7 | 581.5 |
| 2.4 | 607 |
| 3 | 660 |

This temperature profile cannot be estimated with the simplified profile described by equation 3-2. The heat losses are modelled with by convective heat transfer with the air. The equation 3-3 describes the steady state equilibrium.

$$k\nabla^2 T + \frac{2 \cdot h}{l_{Zr}}(T - T_{air}) = 0 \qquad \textit{Eq 3-3}$$

With k the conductivity of the Zircaloy-4, $l_{Zr}$ the length of the plate, h the heat transfer coefficient for Zircaloy in air and $T_{air}$ the temperature of the air. Equation 3-3 has for solution:

$$T(x) - T_{cool} = (T_{cool} - T_{air}) \cdot \cosh\left(\frac{x}{\sqrt{\frac{2 \cdot h}{l_{Zr}}}}\right) + \left[T_{hot} - T_{air} - (T_{cool} - T_{air}) * \coth\left(\frac{2.6}{\sqrt{\frac{2 \cdot h}{l_{Zr}}}}\right)\right] \cdot \sinh\left(\frac{x}{\sqrt{\frac{2 \cdot h}{l_{Zr}}}}\right) \qquad \textit{Eq 3-4}$$

The temperature of the air is assumed to be equal to the temperature of the coolest side. The h is assumed to be equal to 45 $K^{-1}$ and the conductivity is 2100 m/K.[52] Figure 3-16 shows the calculated profiles and the measured thermocouple data points, showing that the temperature model given by equation 3-3 provides a good estimate of the actual temperature profile.

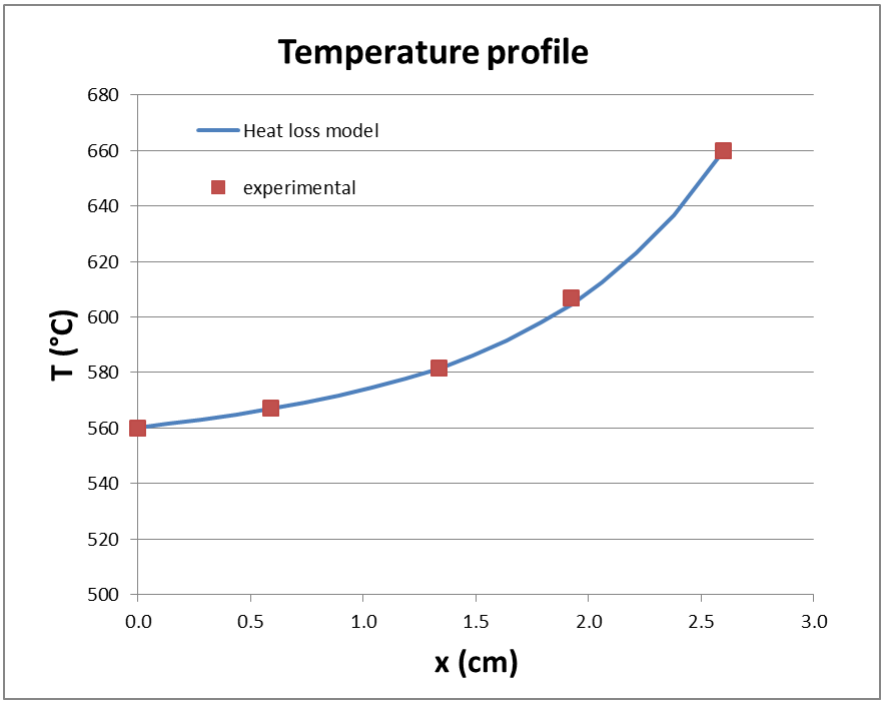


*Figure 3-17: Temperature profile for diffusion experiment*

Subsequent to the experiment, the plate was cut into small samples 1.5 mm wide, and the hydrogen measured in each slice using hot vacuum extraction (performed by Luvak company [53]. Figure 3-18 shows the natural logarithm of the concentration (multiplied by the gas constant R) as a function of the inverse of temperature. The slope of the curve is Q* in J/mol.

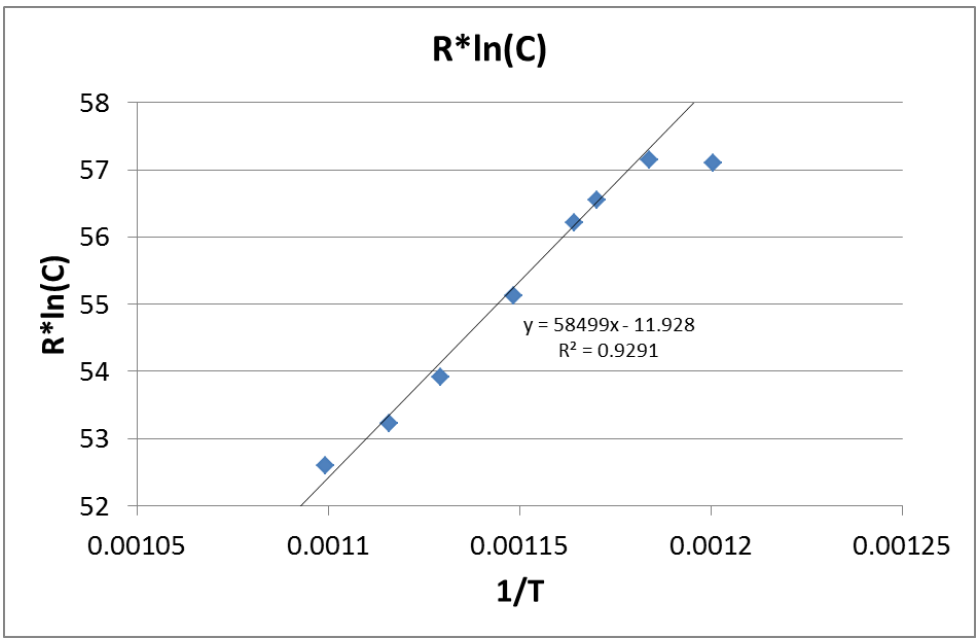


*Figure 3-18: Result of the diffusion experiment*

The value find for Q* is 58.50 kJ/mol.

### *3.1.1.6 Conclusion of the results of the Q* measurement*

The value for Q* found in this work is higher than Kammenzind's measurements. The order of magnitude is comparable, as shown in Figure 3-19. Considering Kammenzind data, it is possible that the value of the temperature gradient has an impact on the value of Q*. This trend seems to be confirmed by the measurement made during this work. The temperature gradient was 38°C/cm, which is significantly lower than Kammenzind's data. However, the comparison of all the measurements versus the temperature gradient, as shown in Figure 3-20, does not confirm such a trend. This result should be confirmed with other temperature gradient in order to validate or not the conjecture. If the value of Q* is dependent on the temperature gradient, the model of the Soret effect should be modified.

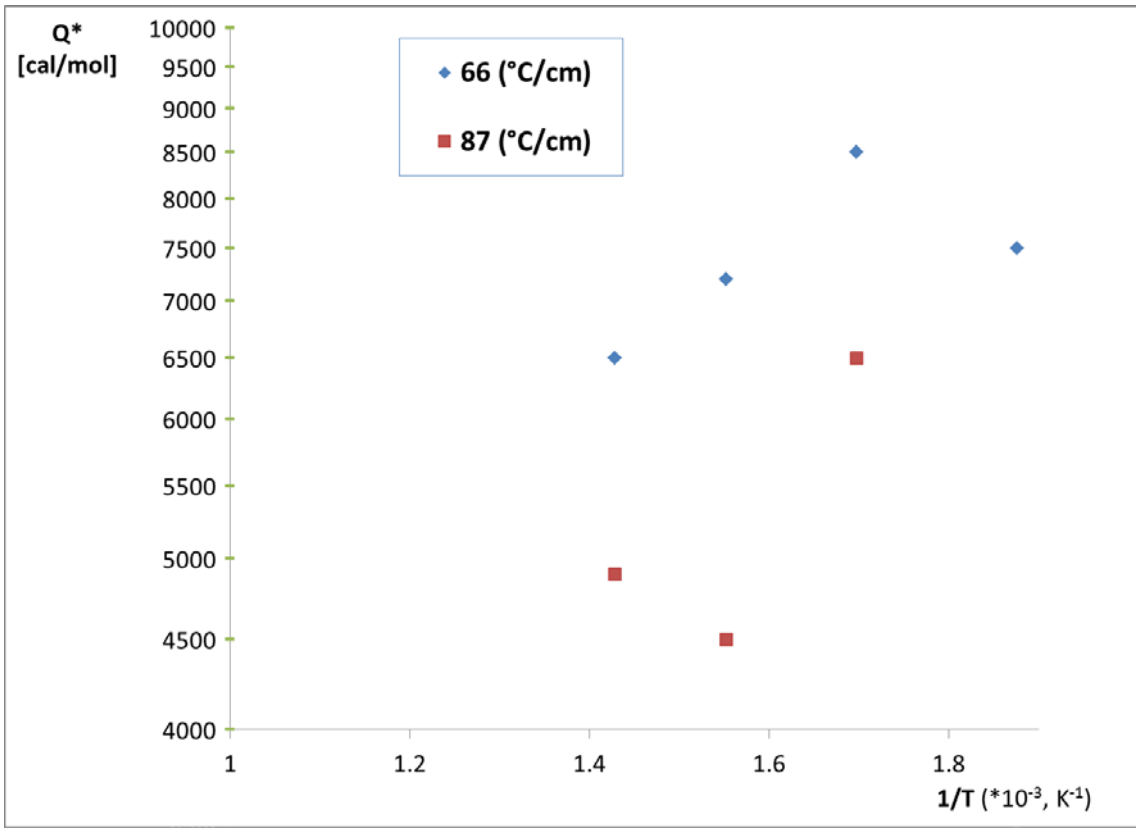


*Figure 3-19: Comparison of experimental results with Kammenzind's data [10]*

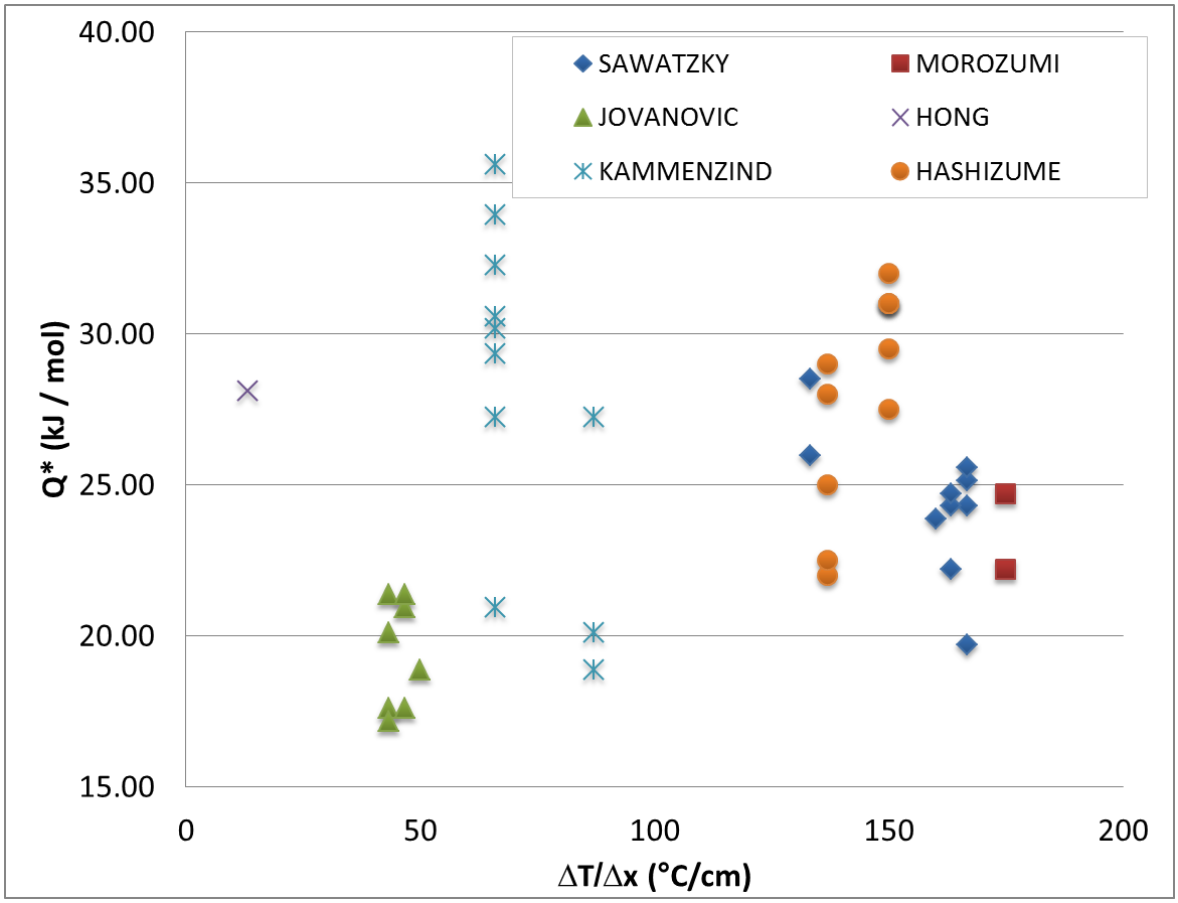


*Figure 3-20: Heat of transport Q* measured in the literature as a function of the temperature gradient*

### 3.1.2 $\alpha^2$ Experiments by Olivier and Chris: materials, procedure and results

#### *3.1.2.1 Experimental technique*

*The current section is directly inspired from Kimberly Colas PhD thesis [54].*

##### 3.1.2.1.1 General description of XRD using synchrotron radiation

The technique used in this study is synchrotron radiation X-Ray diffraction at the Advanced Photon Source (APS) at Argonne National Laboratory (Argonne, Ill). X-Ray diffraction is the process of the coherent scattering of an X-Ray beam by planes of atoms in a crystal and is governed by Bragg's law [55][56]:

$$\lambda = 2\, d\, sin(\theta) \qquad \textit{Eq 3-5}$$

where λ is the wavelength of the x-ray beam (m), d is the inter-planar spacing of the atoms (m) and θ is the diffraction angle (radians) as illustrated in Figure 3-21. The quality of X-Ray diffraction data is directly related to the quality of the X-Ray source used. In this study, the X-Ray source is the APS synchrotron. The APS is a third-generation synchrotron which produces X-rays at a very high brilliance which allows enhanced resolution and high energy radiation compared to conventional laboratory X-ray sources such as Cu-Kα for example. The brilliance is a measure of the intensity (photons per second per unit area) and directionality of the X-ray beam through its divergence (mill radians squared). The brilliance of the APS is 6 to 10 orders of magnitude higher than that of a

conventional X-Ray source such as Cu-Kα [57]. This very high brilliance allows quick acquisition of data, high resolution and low background. This enables the detection of small volume fractions of phases that would otherwise not be detected. In addition, the high photon flux can be produced over a wide range of energies. This enables either the use of a monochromatic beam with a high and well known energy for our material or the use of a polychromatic beam.

In the next section, the beamline used for our experiments (designated 1-ID,) is described. Its position along the APS synchrotron ring is shown in Figure 3-22. This beamline operates at very high energy (e.g. 80 KeV) which allows the X-Ray beam to transmit through the thickness of a 1 mm thick sample, thus providing bulk information on the sample studied.

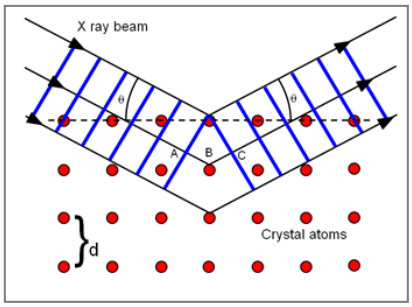


*Figure 3-21: Illustration of Bragg's law.*

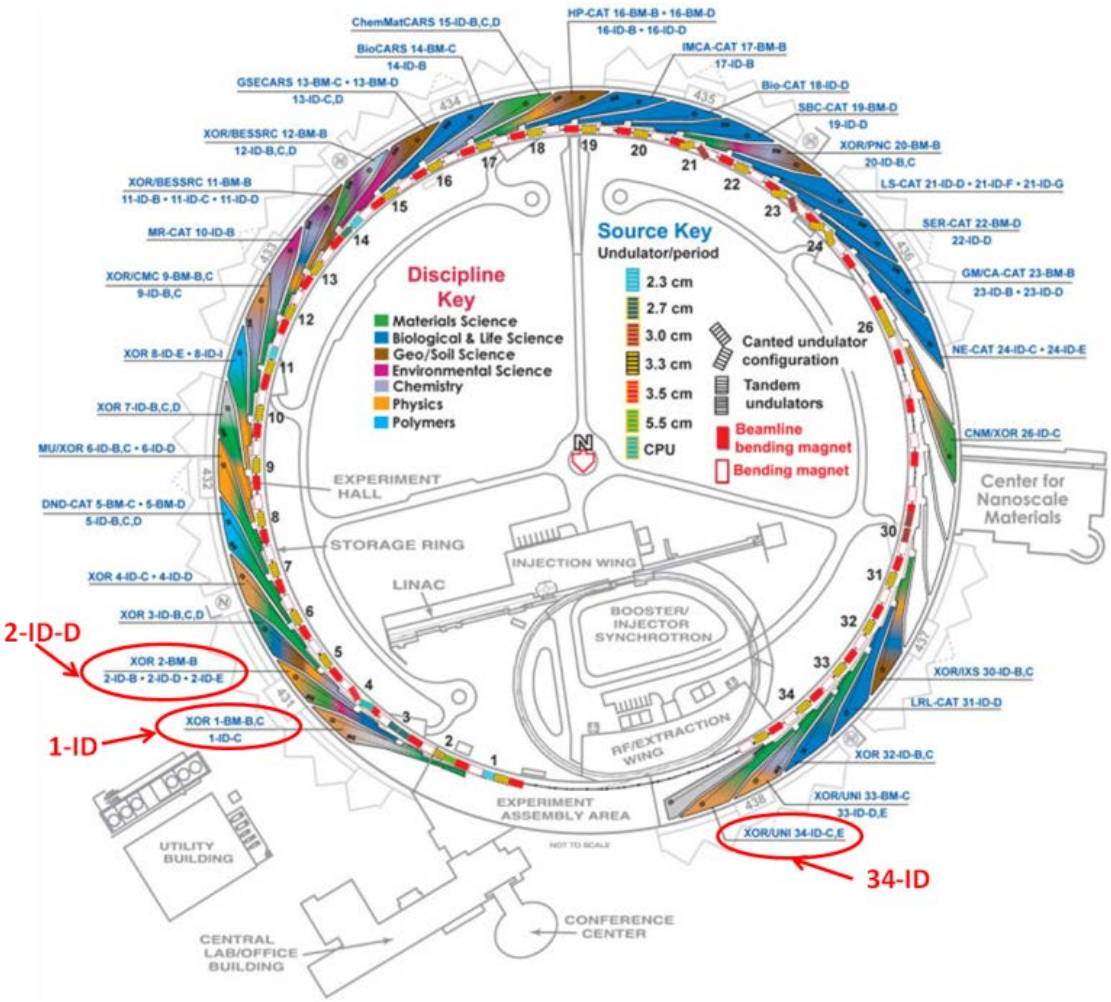


*Figure 3-22: Advanced Photon Source synchrotron and position of the beamline used in our experiment.*

#### 3.1.2.1.2 Beamline 1-ID: High Energy In-Situ Transmission XRD

- ***Beamline properties***

Beamline 1-ID has the unique capability to operate at very high photon energies (more than 80 keV) allowing X-Rays to penetrate through the sample, while operating in transmission X-Ray diffraction. This allows data to be averaged over the full sample thickness which provides very good statistics. This beamline is also equipped with a fast-amorphous silicon GE detector that allows very fast data collection rates. The beam is focused to a rectangular shape with slits which can be as small as 50 x 50 μm [58]. The geometry of the beamline, illustrated schematically in Figure 3-23, allows the full diffraction rings to be recorded, which helps reveal in-plane texture.

The 1-ID beamline is also equipped with an MTS® load frame. This load frame is used for applying stresses to samples by computer monitoring of the applied force, the displacement, or the displacement rate. In addition, an optical furnace can heat the samples up to 900ºC while continuously gathering X-Ray diffraction data. The heating and cooling rates can be monitored by temperature controllers using K-type thermocouples, spot welded onto the sample surface as feedback. The load frame and furnace can be seen in Figure 3-24.

- ***Experimental procedures***

  - **Sample Preparation**

One of the advantages of the 1-ID beamline is that very little sample preparation is needed in order to obtain reliable X-Ray diffraction data. Since the high energy X-Rays penetrate through the entire sample thickness, no particular surface preparation is needed, although having two parallel surfaces through the sample thickness simplifies the calculation of sample to detector distance. The only requirement is to allow full transmission of X-Rays through the sample. In the case of zirconium atoms probed by 80 keV X-Rays, a maximum thickness of 2 mm is allowed for the samples.

  - **Calibration**

A calibration sample of an APS ceria powder is run at the beginning of every experiment in order to measure the exact beam position, angle and sample-to-detector distance. The X-Ray diffraction data from this sample is fitted, and the results of the fit are used to measure the volume fraction of hydrides in the zirconium matrix.

  - **Data Acquisition**

The data is acquired on a large two-dimensional plate detector that allows the recording of the full diffraction ring. The detector recording area is 2048 x 2048 pixels big with each pixel measuring 200 x 200 μm, which gives an angular resolution of $4.6 \times 10^{-3}$ ° with our typical set-up. In the experiments performed at beamline 1-ID, continuous recording of data was performed while heating and cooling of samples under load. This allowed studying the kinetics of hydride precipitation *in situ*. One diffraction frame was recorded as ten consecutive images with a typical exposure time of 1 second (to avoid saturation of the detector). While recording data, the temperature and load were monitored and recorded by control computers. The temperature is measured with a thermocouple that is screwed to the sample, as for the diffusion experiment.

  - **Data Analysis**

Several steps were needed to analyze the raw two-dimensional diffraction frames. The ten images recorded for one frame were summed and averaged by a Matlab® routine developed by J. Almer [58] and the background was subtracted, as described below. Using the Matlab® routine, full diffraction rings were integrated over the whole azimuth (360°). The integration files obtained were then reduced to a one-dimensional GSAS file by the Matlab® routine as illustrated in Figure 3-25. The GSAS peaks obtained were then analyzed using GSAS/Rawplot®[59]. This software program is primarily a Rietveld refinement program that can fit all the different parameters that would affect peak height, shape and position (these parameters can be sample characteristics such as composition, crystal structure, atom positions, etc. or exterior parameters such as sample-to-detector distance, temperature, pressure, etc). However, GSAS also allows a faster refinement by only fitting the peak shape, position and intensity of the raw data in a sub routine called Rawplot. For our peak fitting, the precision and amount of information given by Rawplot were sufficient. The peaks are fitted to a pseudo-Voigt function which is a convolution of Gaussian and Lorentzian peak shapes. Only the Gaussian full-width at half-maximum (FWHM) was fitted while the Lorentzian FWHM remained constant; this Gaussian FWHM gives an understanding of the sample contribution to broadening. The background was modeled using a third-degree polynomial function and several refinement steps were iterated

(usually 10 successive refinements for each parameter we chose to refine). This allowed us to fit the diffraction peaks and obtain (i) the integrated intensity, (ii) the Gaussian full width at half maximum (FWHM), (iii) the peak positions for the desired peaks. Additional details on the data analysis procedure can be found in Kimberly Colas thesis [54].

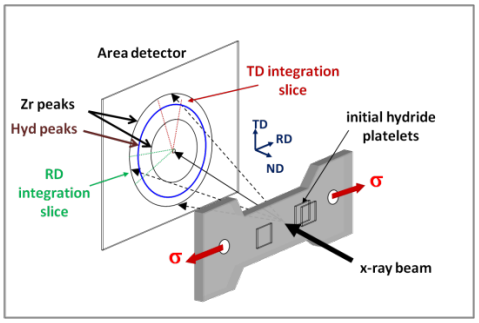


*Figure 3-23: Schematic representation of beam line 1-ID experimental set-up.*

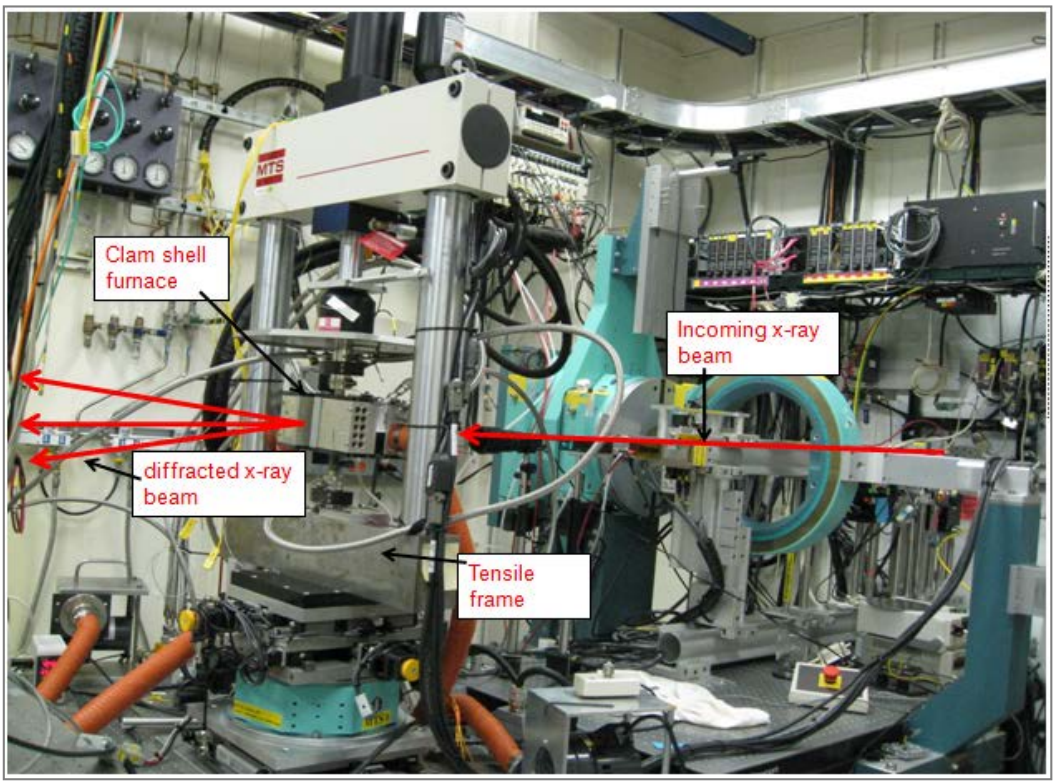


*Figure 3-24: Picture of the experimental set-up at beam line 1-ID.*

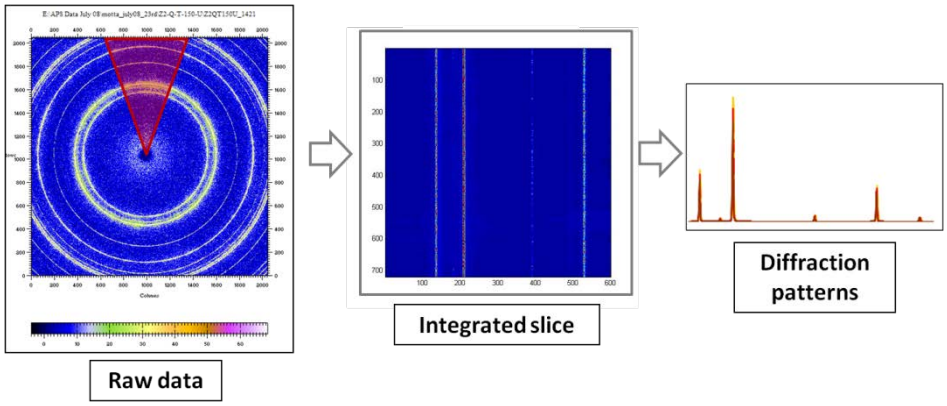


*Figure 3-25: Data Analysis procedure for X-Ray diffraction data collected at beamline 1-ID.*

#### *3.1.2.2 Sample preparation*

The preparation of the samples requires the following steps.

a) Since the sample is exposed to high temperature (~ 500-700°C), the sample may recrystallize. To avoid change to the microstructure during the experiment, the sample is subject to a recrystallization heat treatment before the experiment starts.

b) To prevent oxidation, the samples are coated with a deposited 100 nm layer of Nickel.

c) Hydrogen is put into the sample using to the hydrogen charging equipment at PSU. The concentrations were checked by performing a hydrogen hot vacuum extraction on small parts of the samples. The hydrogen content of the samples are gathered in Table 3-6.

*Table 3-6 Overall hydrogen concentration in the APS samples*

| Sample name | Content (wt.ppm) |
|---|---|
| H_310 | 310 |
| H_400 | 400 |
| H_502 | 502 |
| H_644 | 644 |

#### 3.1.2.3 Experimental procedure

Figure 3-26 shows the evolution of the area under the 111 delta hydride peak and the evolution of temperature with respect to time. The samples were heated to the dissolution temperature, in order to dissolve all the hydrides. This maximum temperature is held for 20 minutes, in order to reach a steady state. Then, the sample is cooled as fast as possible (about 1°C/s) to the target temperature (330°C in Figure 3-26). The sample is then held at this temperature, while the supersaturated hydrogen precipitates. The resulting increase of the hydride peak intensity allows measuring the kinetics of precipitation. In this case, indeed, the equations can be reduced to:

$$\left\{\begin{matrix}\frac{dC_H}{dt} = \alpha^2(C_{SS} - TSSp) \\ \frac{dC_{ss}}{dt} = -\alpha^2(C_{SS} - TSSp)\end{matrix}\right\} \quad \textit{Eq 3-6}$$

with $\alpha$ and TSSp constant.

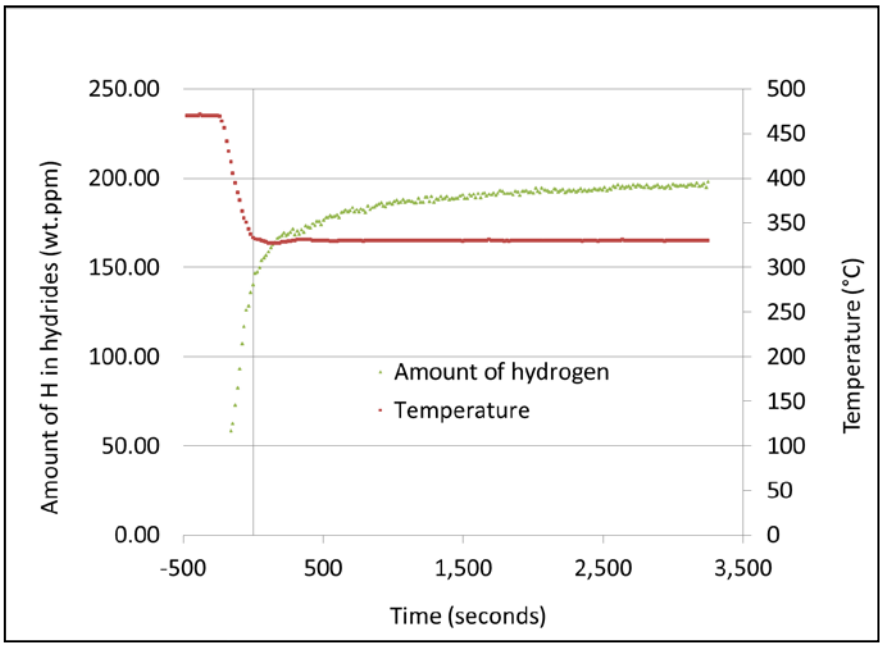


*Figure 3-26: Evolution of temperature and hydrides concentration during synchrotron experiment*

The second differential equation can be solved independently:

$$C_{ss}(t) = Aexp(-\alpha^2 t) + TSSp \quad \textit{Eq 3-7}$$

When t=0, $C_{ss}(0) = C_{ini}$,

$$C_{ss}(t) = (C_{ini} - TSSp) \cdot exp(-\alpha^2 t) + TSSp \quad \textit{Eq 3-}$$

Then, the second equation of system 3-6 can be solved:

$$\frac{dC_p}{dt} = \alpha^2(C_{ini} - TSSp)\, exp(-\alpha^2 t) \quad \textit{Eq 3-9}$$

So,

$$C_p(t) = -(C_{ini} - TSSp)\, exp(-\alpha^2 t) + A \quad \textit{Eq 3-10}$$

When t=0, $C_p(0) = C_{Pini}$, so:

$$C_{Pini} + C_{ini} - TSSp = A \quad \textit{Eq 3-11}$$

$$C_p(t) - C_{Pini} = (C_{ini} - TSSp)(1 - exp(-\alpha^2 t)) \quad \textit{Eq 3-12}$$

$$\frac{C_p(t) - C_{Pini}}{(C_{ini} - TSSp)} = (1 - \exp(-\alpha^2 t)) \quad \textit{Eq 3-13}$$

$$\frac{C_p(t) - C_{Pini}}{(C_{ini} - TSSp)} - 1 = -\exp(-\alpha^2 t) \quad \textit{Eq 3-14}$$

$$\frac{C_p(t) - C_{Pini} - C_{ini} + TSSp}{(C_{ini} - TSSp)} = -\exp(-\alpha^2 t) \qquad \textit{Eq 3-15}$$

Recalling:

$$C_{TOT} = C_{ini} + C_{Pini} = C_p(t) + C_{SS}(t) \qquad \textit{Eq 3-16}$$

When t → infinity,

$$C_p(\infty) = C_{TOT} - TSSp \qquad \textit{Eq 3-17}$$

So,

$$\frac{C_p(\infty) - C_p(t)}{C_{TOT} - C_{Pini} - TSSp} = \exp(-\alpha^2 t) \qquad \textit{Eq 3-18}$$

Taking the logarithm of the previous expression:

$$-\log\left(C_p(\infty) - C_p(t)\right) = \alpha^2 t - \log(C_{TOT} - C_{Hini} - TSSp) \qquad \textit{Eq 3-19}$$

Plotting the log of the concentration against time allow the estimation of $\alpha^2$ with a linear regression.

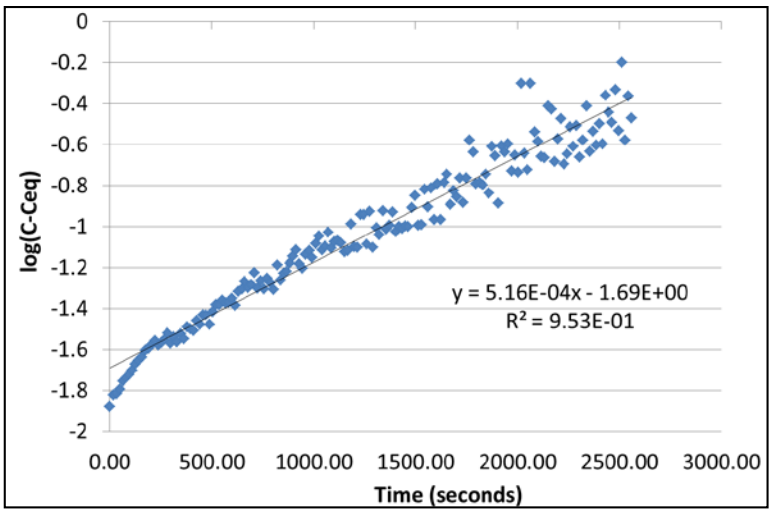


*Figure 3-27: Linear regression and alpha calculation*

In Figure 3-27 case, the regression gives $\alpha^2(330°C) = 5.16 * 10^{-4} s^{-1}$ *and* $\alpha = 0.023\ s^{-1/2}$ at 320°C and with an initial hydrogen content of 310 wt. ppm.

#### *3.1.2.4 Results*

In addition to the preliminary experiment detailed in the previous section, the hydride precipitation rate has been determined for five different temperatures and with three different initial concentrations using the approach illustrated in Figure 3-27. The measured values of $\alpha^2$ are summarized in Table 3-7, while the value for $\alpha$ are given in Table 3-8. Figure 3-28 shows the value of $\alpha^2$ agains the inverse of the absolute temperature. Figure 3-29 shows the $\alpha$ values against the inverse of temperature, and also displays the values reported by Kammenzind [51].

*Table 3-7 Measurement of the kinetics parameter alpha$^2$ (s)*

| | **Initial total concentration** | | | |
|---|---|---|---|---|
| **Temperature** | **310 wt. ppm** | **400 wt. ppm** | **502 wt. ppm** | **644 wt. ppm** |
| 288°C | n/a | 1.69E-04 | 1.69E-04 | 1.23E-03 |
| 316°C | n/a | 2.56E-04 | 1.69E-04 | 2.56E-04 |
| 330°C | 5.29E-04 | n/a | n/a | n/a |
| 332°C | n/a | 3.24E-04 | 2.25E-04 | 5.29E-04 |
| 360°C | n/a | 2.89E-04 | 1.69E-04 | 2.56E-04 |
| 380°C | n/a | n/a | 1.96E-04 | 4.00E-04 |
| 400°C | n/a | n/a | 1.69E-04 | n/a |

*Table 3-8 Measurement of the kinetics parameter alpha ($s^{-1/2}$)*

| | **Initial total concentration** | | | |
|---|---|---|---|---|
| **Temperature** | **310 wt. ppm** | **400 wt. ppm** | **502 wt. ppm** | **644 wt. ppm** |
| 288°C | n/a | 0.013 | 0.013 | 0.035 |
| 316°C | n/a | 0.016 | 0.013 | 0.016 |
| 330°C | 0.023 | n/a | n/a | n/a |
| 332°C | n/a | 0.018 | 0.015 | 0.023 |
| 360°C | n/a | 0.017 | 0.013 | 0.016 |
| 380°C | n/a | n/a | 0.014 | 0.020 |
| 400°C | n/a | n/a | 0.013 | n/a |

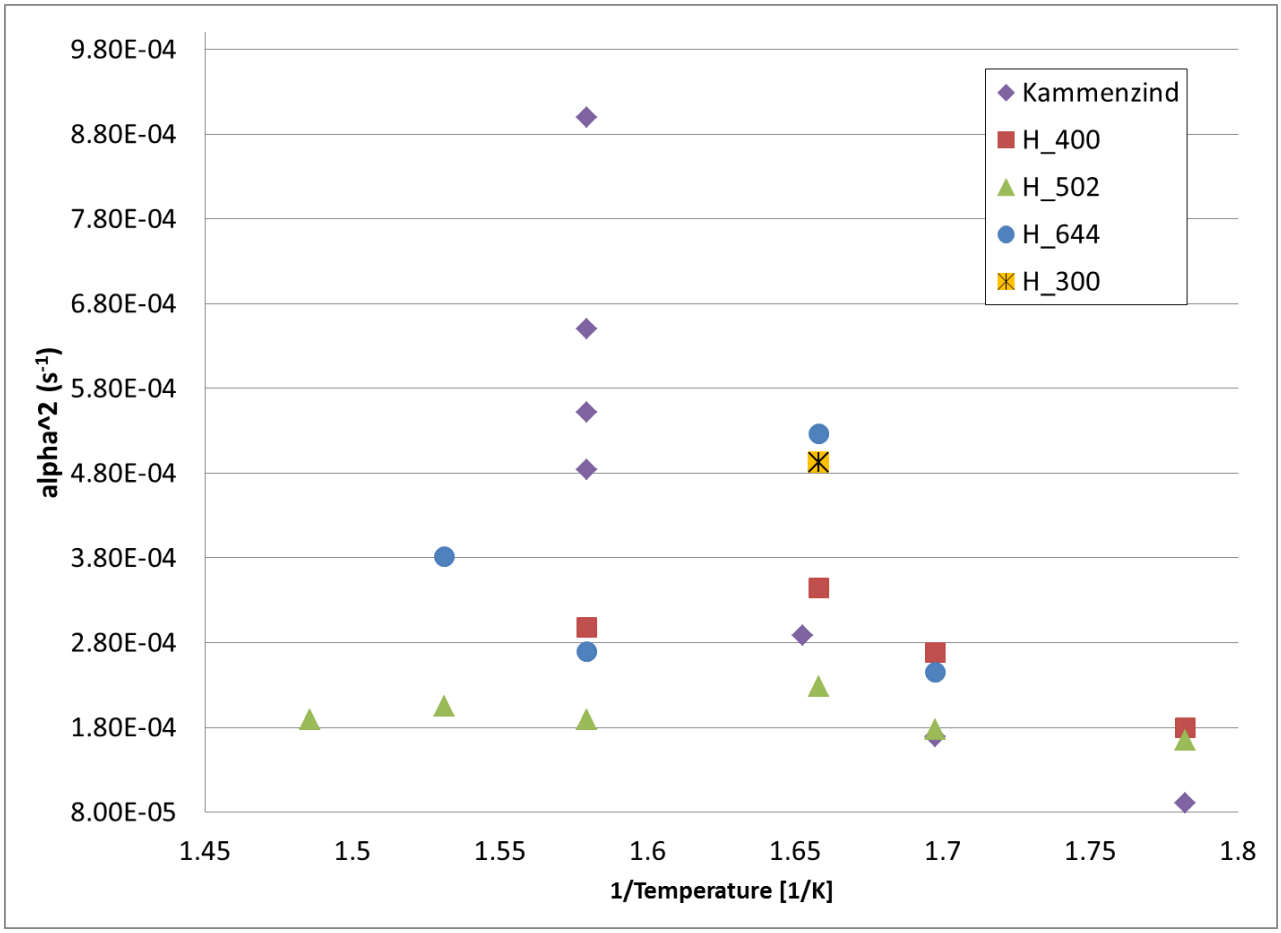


*Figure 3-28: Measured precipitation parameter $\alpha^2$ with respect to 1/T, with different initial concentration (300, 400, 502 and 644 wt. ppm)*

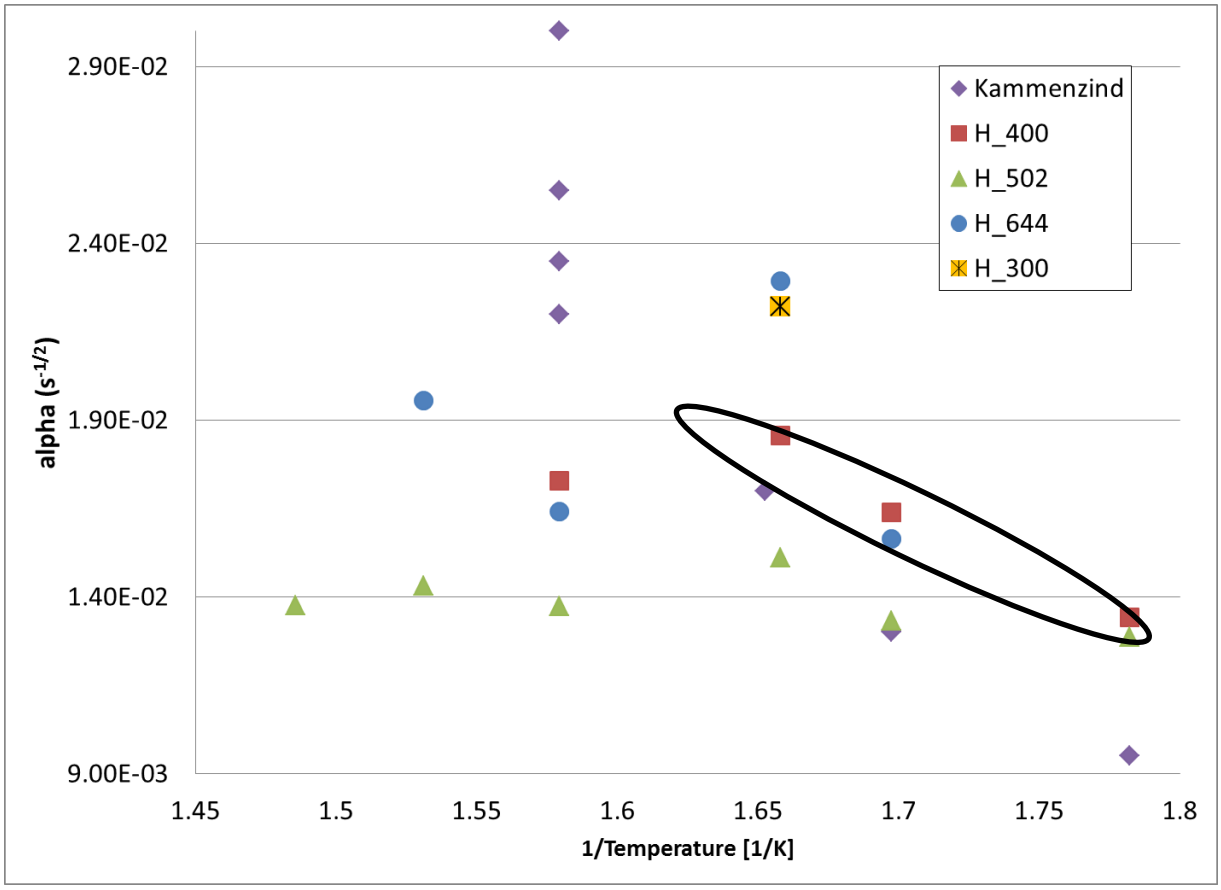


*Figure 3-29: Measured precipitation parameter **α** with respect to 1/T, with different initial concentration (300, 400, 502 and 644 wt. ppm)*

### *3.1.2.5 Conclusion of the results*

Kammenzind suggested using a fitting with an Arrhenius law in his work [51]. The fitting of his results is reproduced in Figure 3-30. It is clear that the results obtained in this work, and which are also shown in Figure 3-30 cannot be fitted with the same law. The results obtained and shown in Figure 3-29 do not confirm these measurements. In fact, several observations can be made regarding the results. First, three of the four alpha values obtained for the sample with a low initial concentration (400 wt.ppm) show a similar temperature dependence as in Kammenzind's data (as shown in Figure 3-30), with an offset of about 0.03 $s^{-1/2}$. In contrast contrary, the data obtained with the 502 wt.ppm initial concentration shows a value of $\alpha$ that is almost constant with temperature. We should note that the temperature profiles imposed on the samples at APS varied somewhat in the intended temperature ramps, leading us to believe that these results are more reliable. This variation was smallest in the 502 wt.ppm set of measurements. For example with the 644 wt.ppm sample, the results are very heterogeneous.

At this point, several interpretations can be made. It is possible that the value of $\alpha$ does not depend on temperature. The values are only changing from 0.009 to 0.024, with a high number of data points between 0.015 and 0.022. Then, the variations could be caused by uncertainties in the temperature profile and the temperature measurements. As stated above, the least scattered data values are obtained in the sample with 502 wt.ppm, which shows a constant profile. It is also possible that $\alpha$ does depend on temperature. There is a global trend showing higher values of alpha when the

temperature increases.it could be expected that the precipitation kinetics would be faster at higher temperature because of higher diffusion. The observation of constant alpha could also indicate a temperature independent process such as interface absorption of hydrogen into the hydrides.

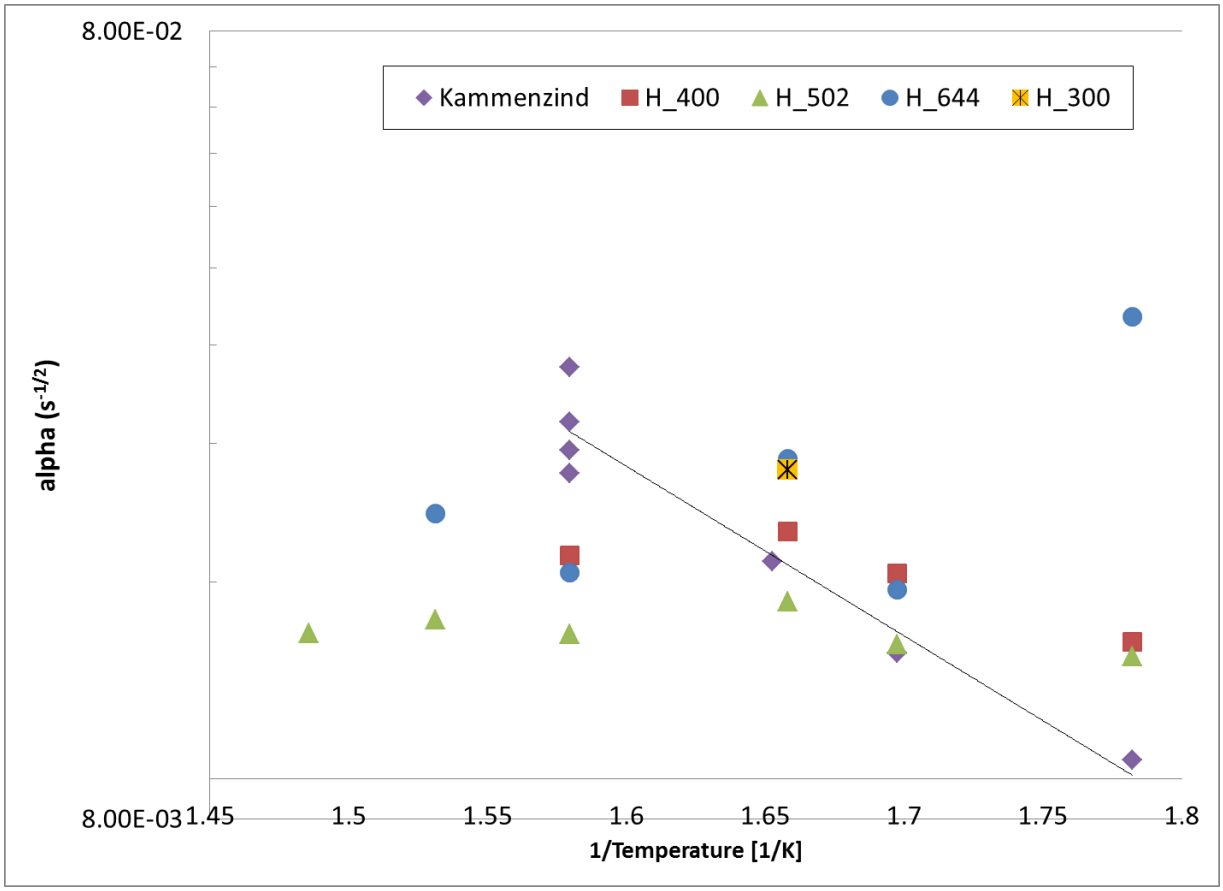


*Figure 3-30: Measured precipitation parameter α with respect to 1/T, in log scale and with Kammenzind interpolation*

### 3.1.3 Data reprocessing, analysis and alternate model

The model developed previously showed promising results. However, when observing this model in closer detail, it was observed that it is kinetically inaccurate. This model is only predicting hydrogen growth, as stated by Marino [38]. When a sample containing hydrogen cools down from an elevated temperature, a portion of the hydrogen will nucleate. Nucleation is not modeled in the previous model. Therefore, an initial attempt to model hydride nucleation in the matrix has been made.

Section describes a detailed analysis of an experiment performed to study hydride precipitation in Zircaloy-4 as it occurs, that is, in-situ. The principle of this experiment was to heat previously hydrided samples to a high enough temperature to dissolve all hydrides present in the sample, and then cool the sample down fast to different target temperatures. This was followed by a hold at the target temperature, all the while following the increase of the hydride diffraction signal as hydrides precipitate. Upon cooling, hydrogen is supersaturated in solid solution. Holding at the fixed temperature then causes hydrogen to precipitate into hydrides. The evolution of the hydride content can then be measured through the increase in the hydride diffraction signal.

The (111) δ-hydride peak intensity was converted into hydride content and its evolution over time was observed, the data was then used to find a value for alpha. Precipitation of zirconium hydrides is governed by the equation set 2-54. The precipitation of hydrogen into hydride this experience is described by equations 3-20 and 3-21.

$$\begin{cases} \frac{dC_P}{dt} = \alpha^2(C_{ss}(t) - TSS_P) & \text{Eq 3-20} \\ \frac{dC_{ss}}{dt} = -\alpha^2(C_{SS}(t) - TSS_P) & \text{Eq 3-21} \end{cases}$$

where $C_P$ is the concentration of hydrogen present as hydrides, α is the kinetics parameter, $C_{SS}$ is the hydrogen content present in the in solid solution and $TSS_p$ is the terminal solid solubility for precipitation at the holding temperature. By solving the differential equations 3-20 and 3-21, it is possible to obtain the hydrogen content in solid solution, as the hydrogen content in hydrides can be found from the mass conservation equation for hydrogen in the sample. Rearranging equation 2, we have:

$$\frac{dC_{SS}}{C_{SS}(t) - TSS_P} = -\alpha^2 dt \qquad \text{Eq 3-22}$$

Integrating equation 3-22 between t=0 and t, we obtain:

$$\ln(C_{SS}(t) - TSS_P) = -\alpha^2 t + \ln(C_{SS}^{ini} - TSS_P) \qquad \text{Eq 3-23}$$

where $C_{SS}^{ini}$ is the initial hydrogen content in solid solution (at t=0). This value is estimated after the temperature is stabilized following cooling. From conservation of hydrogen in the sample, we obtain:

$$C_{SS}(t) + C_P(t) = C_P^{eq} + TSS_P \qquad \text{Eq 3-24}$$

where $C_P^{eq}$ is the hydrogen content in hydrides when steady state is reached, at the target temperature. Thus,

$$C_{SS}(t) - TSS_P = C_P^{eq} - C_P(t) \qquad \text{Eq 3-25}$$

By inserting equation (3-25) into (3-23), it is possible to obtain the evolution of the hydrogen in hydrides, $C_P(t)$, as a function of time:

$$\ln\left(C_P^{eq} - C_P(t)\right) = -\alpha^2 t + \ln(C_{SS}^{ini} - TSS_P) \qquad \text{Eq 3-26}$$

Thus,

$$C_P(t) = C_P^{eq} - \left(C_{SS}^{ini} - TSS_P\right)e^{-\alpha^2 t} \qquad \textit{Eq 3-27}$$

If it is assume that the diffracted intensity of the (111) peak from the δ-phase obtained in the in-situ diffraction synchrotron experiment is proportional to the hydride volume fraction, it is possible to determine $C_P(t)$. As discussed above, $C_P^{eq}$ is the equilibrium value of hydrogen in hydride form. From the definition of the $TSS_P$, this value is $C_{TOT} - TSS_P$. In order to find α, the parameter $I_\alpha = \ln\left(C_P^{eq} - C_P(t)\right) \times 1 \cdot 10^4 = (-\alpha^2 t + \ln(C_{SS}^{ini} - TSS_P)) \times 10^4$ is defined. $I_\alpha$ has no specific

physical significance but is useful to calculating the value of α. This parameter was plotted versus time and a linear regression was performed. As an example, The results for a sample of 541 wt ppm cooled down from 550°C to 400°C at 1°C/s are shown in *Figure 3-31*.

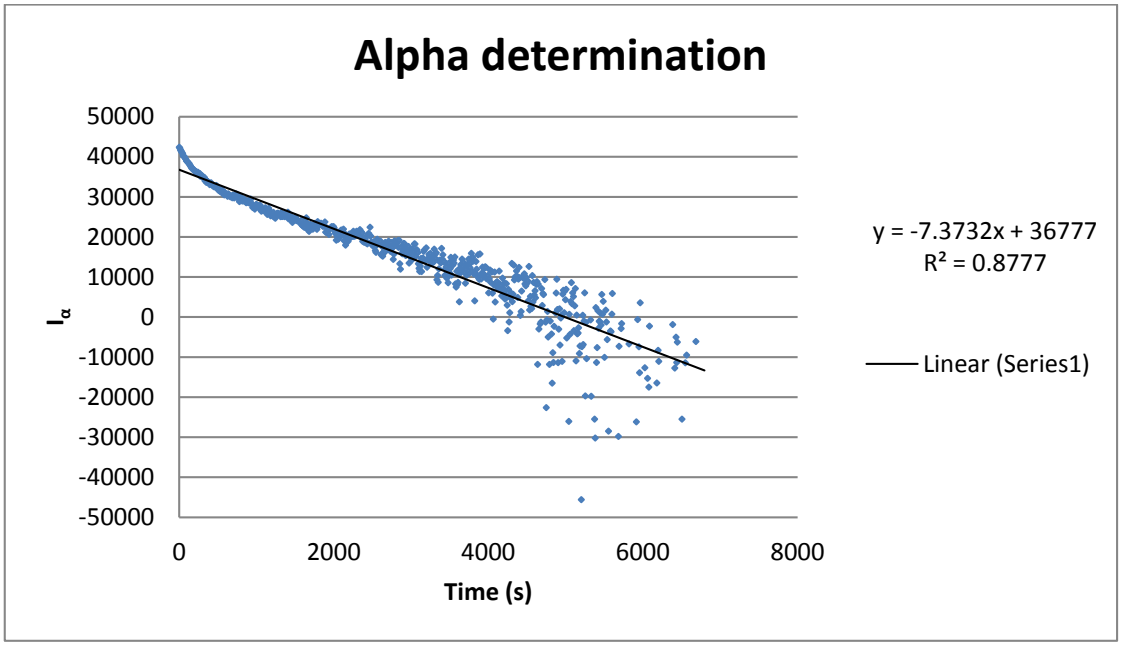


*Figure 3-31. Least-squares linear fitting of the calculated Iα versus time to obtain a value for α for the 541 wt. ppm sample heated up to 550°C and then cooled to 400°C.*

*Figure 3-31* shows that the scatter on the value of $I_\alpha$ increases significantly with time. This comes from the fact that in plotting $\ln\left(C_P^{eq} - C_P(t)\right)$, as steady state is approached the lesser the difference between the two values becomes. Mathematically, it means that when $t \to \infty, C_p(t) \to C_P^{eq}$ and therefore, when t→ ∞, $C_P^{eq} - C_P(t)$ is just the statistical error coming from the synchrotron, and as ln(x) shows the most variation when x is small, the error present when reaching steady state will be large. For that reason, it was decided to stop the fitting process at the time where the concentration of hydrogen in hydrides reaches 99% of the steady state, which in this case occurs at about 4,300s. Following this, the plot in figure 3-32 is obtained. The fitting value given here is in the format y=ax+b where y is $I_p$, a is $-\alpha^2$, x is the time (t) and b is $\ln(C_{SS}^{ini} - TSS_P)$. The values of these three parameters, calculated with those two methods, as shown in *Figure 3-31* and *Figure 3-32* differ greatly. It is possible that by not stopping the fitting at 99%, the errors introduced to the fitting were too great and masked the temperature dependence of α [60].

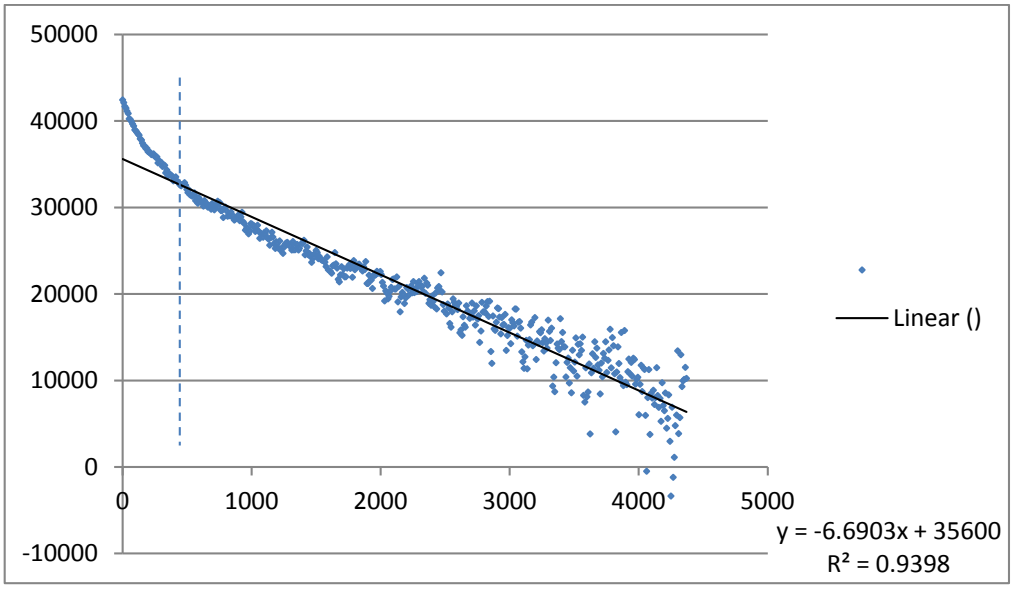


*Figure 3-32. Linear least-squares fitting of Iα versus time to obtain a value for alpha, considering only points up to 99% of steady state.*

As observed on *Figure 3-32*, a significant discrepancy between the fit and the data occurs at the beginning of the experiment (shown by a dashed line on *Figure 3-32*). This difference was consistently observed on the various plots obtained. The difference was also observed on other work, such as M.S. Blackmur [61], who performed a similar experiment (with higher cooling rates) to determine the nucleation rates of hydrides in zirconium hydrides (Blackmur's experiment however was not aimed to determine the kinetics parameter α). When taking the graph of the evolution of hydrides in their samples, that same initial difference appeared between the fit and the data. A better fit to the data is obtained if the following equations rule hydrogen precipitation during an initial regime, which is only valid during the initial time period $t_{ini}$ :

$$\begin{cases} \dfrac{dC_P}{dt} = \lambda^2 (C_{ss}(t) - TSS_P)^2 \\ \dfrac{dC_{ss}}{dt} = -\lambda^2 (C_{SS}(t) - TSS_P)^2 \end{cases}$$

Eq 3-28
Eq 3-29

where λ is another precipitation parameter. To find λ it is first necessary to solve the differential equation, as was done for α. Rearranging equation 3-29, we obtain:

$$\frac{dC_{ss}}{(C_{SS}(t) - TSS_P)^2} = -\lambda^2 dt$$

Eq 3-30

$$\frac{-1}{(C_{SS}(t) - TSS_P)} + \frac{1}{\left(C_{SS}^{ini} - TSS_P\right)} = -\lambda^2 t$$

Eq 3-31

Integrating equation 3-30 between t=0 and t, we obtain:

Solving for $C_{SS}(t)$:

$$C_{SS}(t) = \frac{1}{\lambda^2 t + \frac{1}{C_{SS}^{ini} - TSS_P}} + TSS_P$$

Eq 3-32

By substituting equation (3-25) into (3-32) and rearranging, it is possible to obtain the evolution of the hydrogen concentration in the δ-phase, $C_P(t)$:

$$\frac{1}{\left(C_P^{eq} - C_P(t)\right)} = \lambda^2 t + \frac{1}{\left(C_{SS}^{ini} - TSS_P\right)} \qquad \text{Eq 3-33}$$

Thus,

$$C_P(t) = C_P^{eq} - \frac{1}{\lambda^2 t + \frac{1}{C_{SS}^{ini} - TSS_P}} \qquad \text{Eq 3-34}$$

To estimate gamma, the parameter $I_\lambda = \frac{1}{\left(C_P^{eq} - C_P(t)\right)} \times 1 \cdot 10^5$ is defined, corresponding to $10^5$ times the left hand side of equation 3-33. This parameter is plotted versus time to obtain a fit that would represent equation 3-35:

$$I_\lambda = \left(\lambda^2 t + \frac{1}{\left(C_{SS}^{ini} - TSS_P\right)}\right) \times 10^5 \qquad \text{Eq 3-35}$$

Similarly to before, the fitting was based only on a short period of time (trying to approach $t_{ini}$). This was done for different reasons. First, the hypothesis assumed here is that at the initial time a transition regime governs the kinetics and second, upon approaching steady state, $C_P^{eq} \rightarrow C_P(t)$ and thus $C_P^{eq} \rightarrow C_P(t)$tends to become the statistical variation of the synchrotron counts. In other words, the error when approaching steady state will become too big to have an accurate fit. The fit for the same data set as Figure 3-31 and Figure 3-32 is given in Figure 3-33.

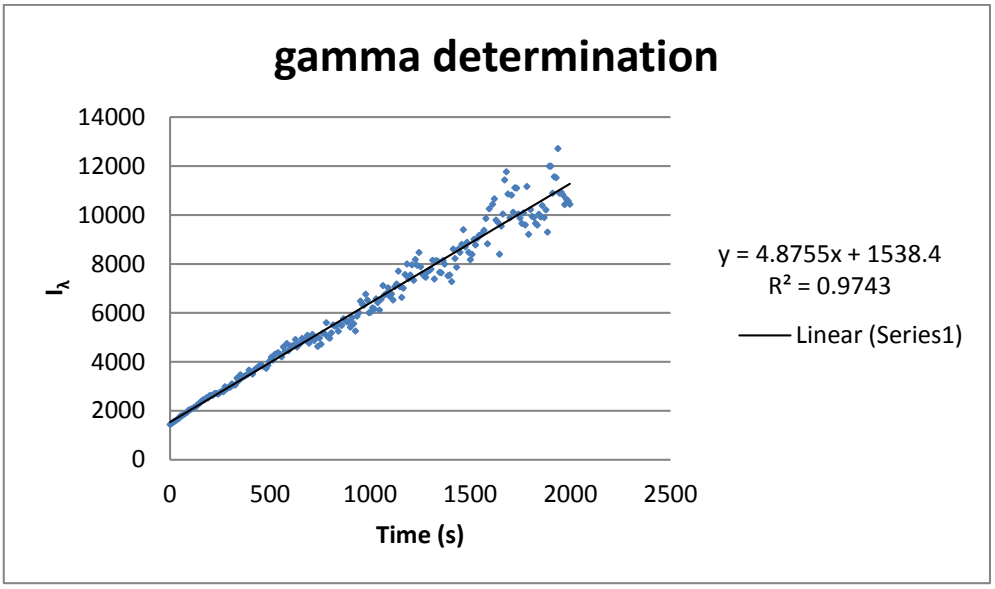


*Figure 3-33. Linear least squares fitting of Iλ versus time to get a value for λ until 95% of steady state in this case for the sample of 541 wt.ppm heated up to 550°C and then cooled down and held at 400°C.*

As shown in Figure 3-33, the fit this time is very good ($R^2$=0.97) and no discrepancy is observed at the beginning of the experiment. Although it is still unclear what mechanisms are involved during that regime, this fit seems to work best. A possible explanation of this would be that a hydride

"nucleation regime" is present up to $t_{ini}$. If two hydrogen atoms have to react to create a nuclei, this is in agreement with the linear dependence of $\frac{dC_{SS}}{dt}$ with $(C_{SS}(t) - TSS_P)^2$. This method is now applied to the analysis of the experimental data obtained by Courty and Piotrowski [62] in the following section.

### 3.1.4 Analysis of Hydrogen Precipitation using the new model

The hydride peak diffracted intensities for the different samples were plotted according to the methods above and fits were obtained, considering both an initial transient regime followed by another regime in which the kinetics follow that of Marino's model.

The results were also fitted using the α value given by Kammenzind [63]. An example of this is shown in Figure 3-34. It is clear that the precipitation kinetics described by Kammenzind's $\alpha^2$ value do not work well for the present case. This is possibly because the fast cool down causes their precipitation process to be different than in Kammenzind's diffusion controlled experiment.

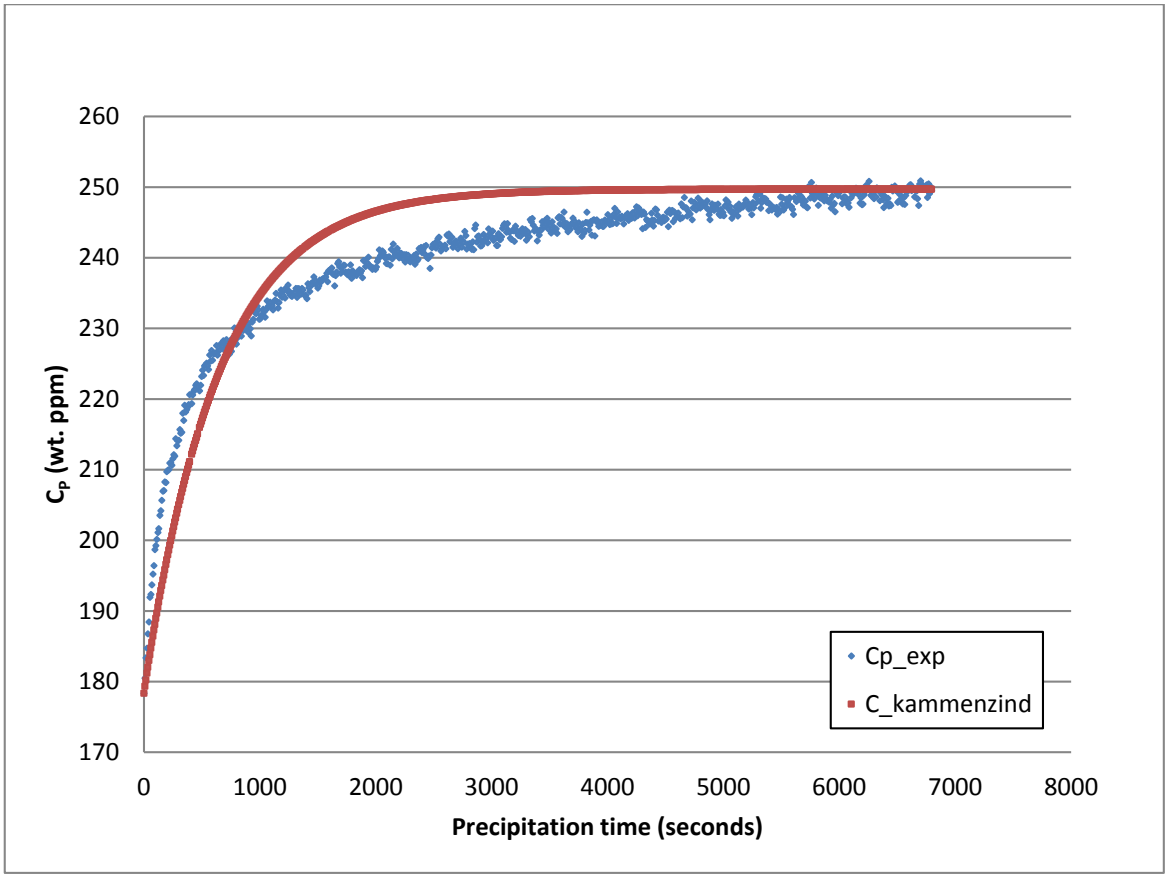


*Figure 3-34. CP (wt.ppm) as determined from the diffraction peak intensity as a function of hold time at 400°C for a sample containing 541 wt.ppm of hydrogen (blue). Simulation of this experiment following Marino's model with Kammenzind's α2 value.*

Figure 3-35 shows the fits obtained using the two-step process on another data set. The fit was done in two steps. The first step was to fit the beginning of the curve with the new model. The second step was to fit the second part of the curve using Marino's model while still preserving continuity both between the two fits and in the first derivative between the first regime and the second regime. This was done by graphically equating the derivatives of the curves and the curves themselves. This leads to an offset of the Marino's model corresponding to the above mentioned $t_{ini}$. In this fitting manner,

the change in regime has been identified as being at the time when the two different expressions governing $C_P$ (represented by equations (3-27 and 3-34) are equal. This task was performed graphically since the equation cannot be solved analytically. Figure 3-35 illustrates this method well.

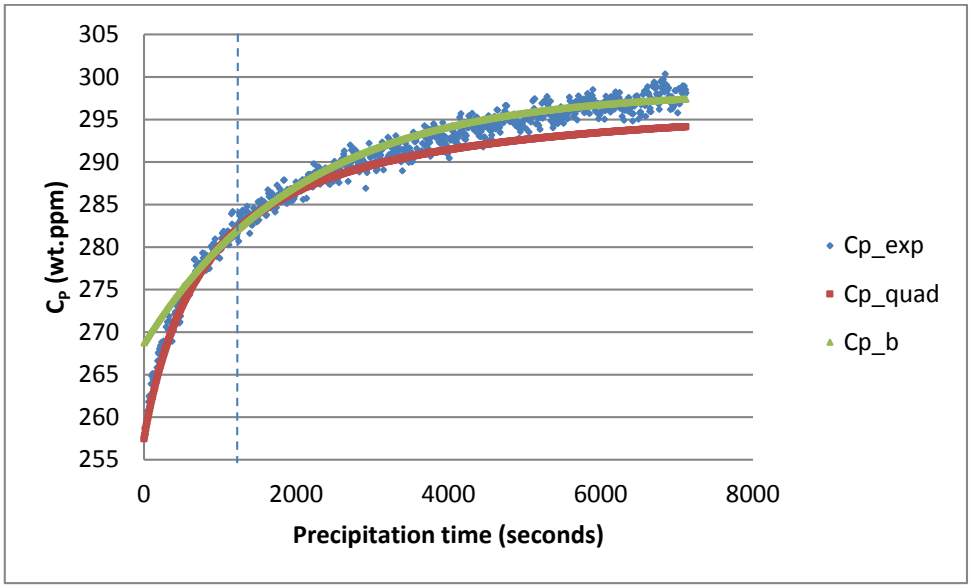


*Figure 3-35. Fitting of experimental data with the two different models explained in 1, on a 541 wt. ppm sample, heated up to 550°C and cooled down to 380°C. Cp_quad is used in the transition regime and Cp_b corresponds to the regime governed by Marino's model.*

Figure 3-35, shows three plots: the experimental plot (blue dots), the second regime's plot (Marino's model, shown by the green curve) and the first regime's plot (in red). The green plot has been offset and equated to the red curve at the transition between the two regimes (the blue, dashed vertical line is where the transition occurs). Although this method is not very precise, it can provide a good fit to the data acquired at the APS, as it can be seen in Figure 3-36 through Figure 3-38.

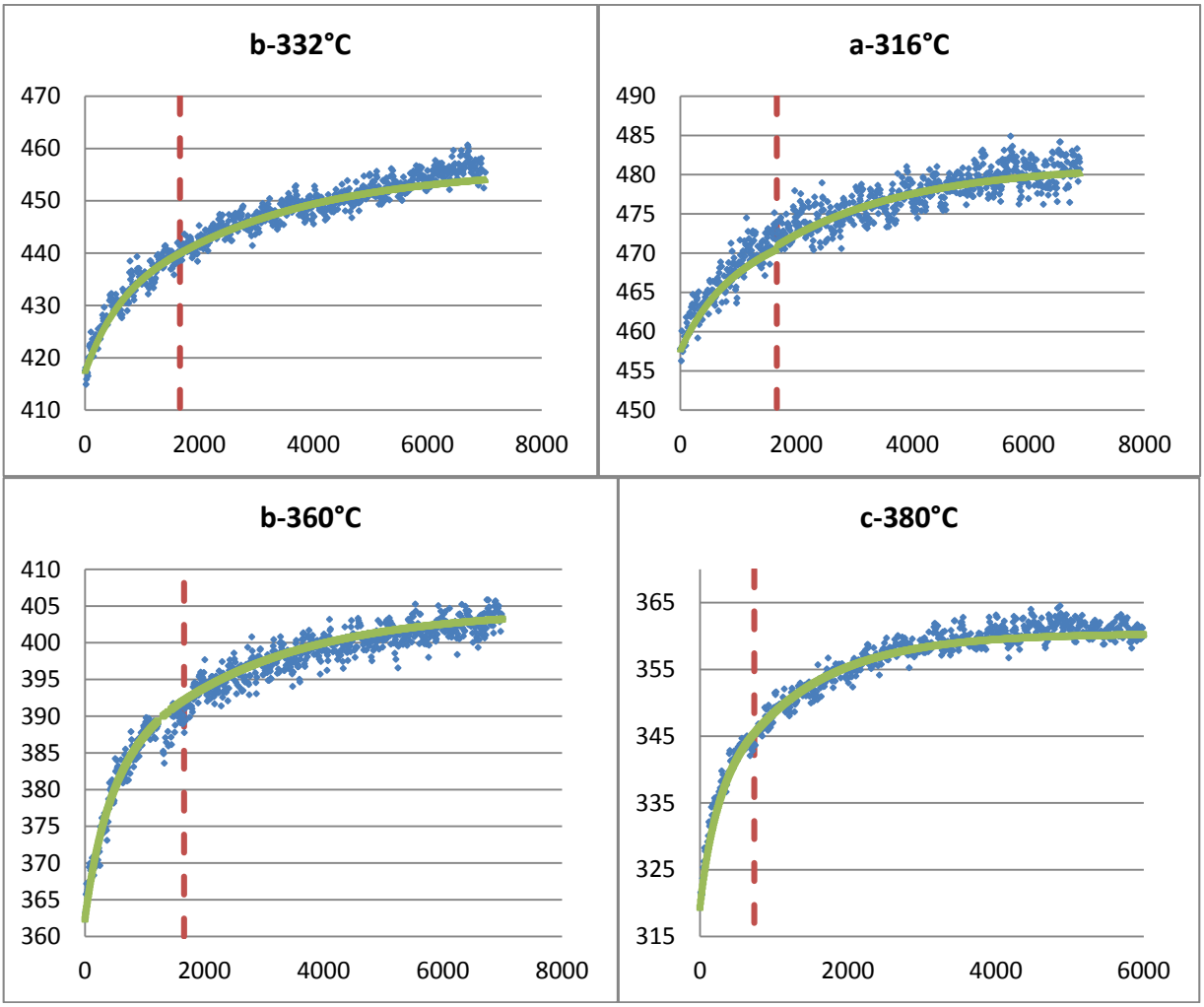


*Figure 3-36. Comparison of hydride evolution from the model done (with two regimes, shown in green) with the actual evolution (shown in blue), observed in situ at the APS on a 603 wt. ppm sample heated up to 550°C and cooled down to 316°C (a), 332°C (b), 360°C (c) and 380°C (d). In each case, the y axis represents the hydrogen content as hydrides in wt.ppm and the x axis represents the holding time at the given temperature in seconds.*

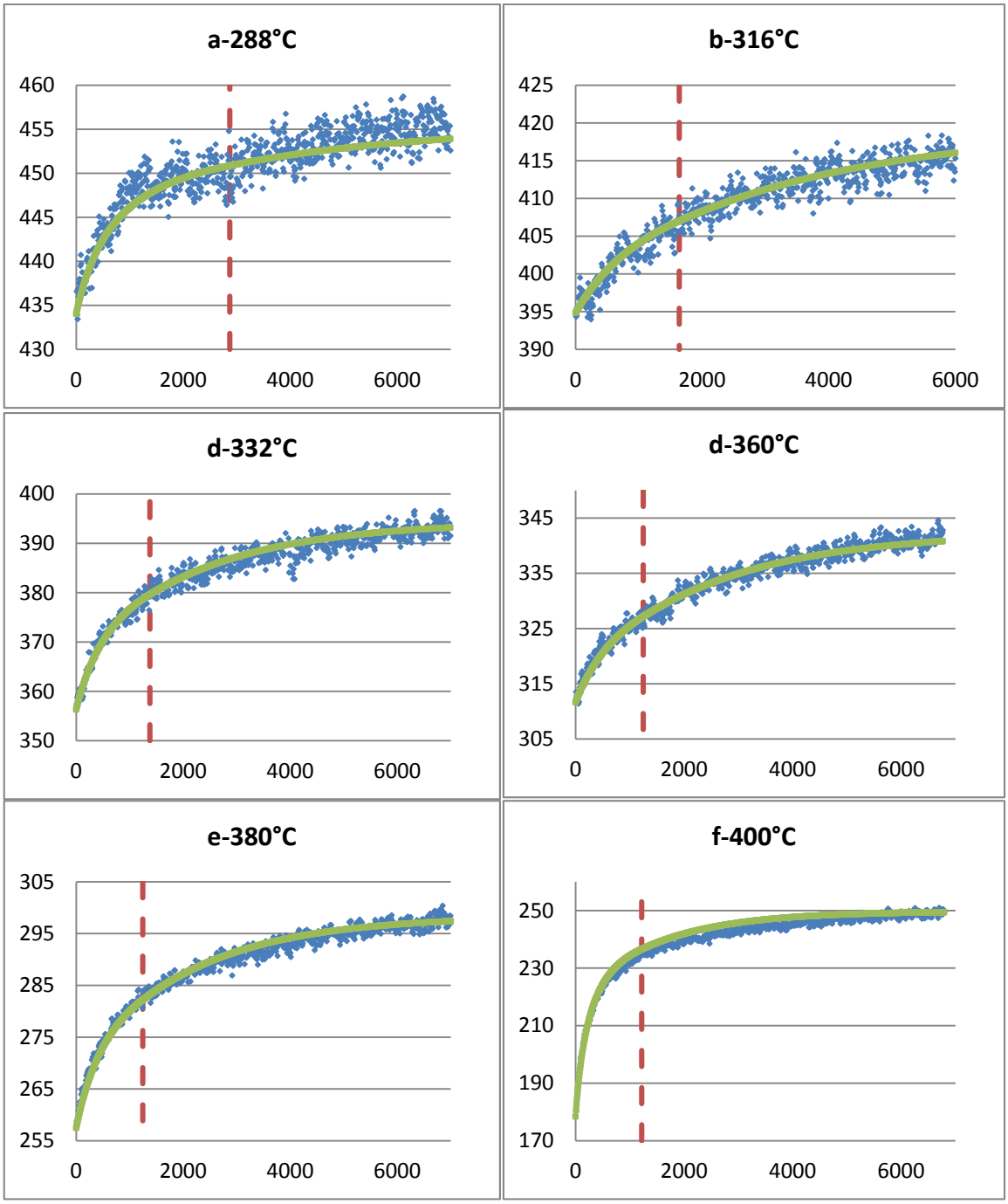


*Figure 3-37. Comparison of hydride evolution from the model done (with two regimes, shown in red) with the actual evolution (shown in blue), observed in situ at the APS on a 541 wt. ppm sample heated up to 550°C and cooled down to 288°C (a), 316°C (b), 332°C (c), 360°C (d), 380°C (e) and 400°C (f). In each case, the y axis represents the hydrogen content as hydrides in wt.ppm and the x axis represents the holding time at the given temperature in seconds.*

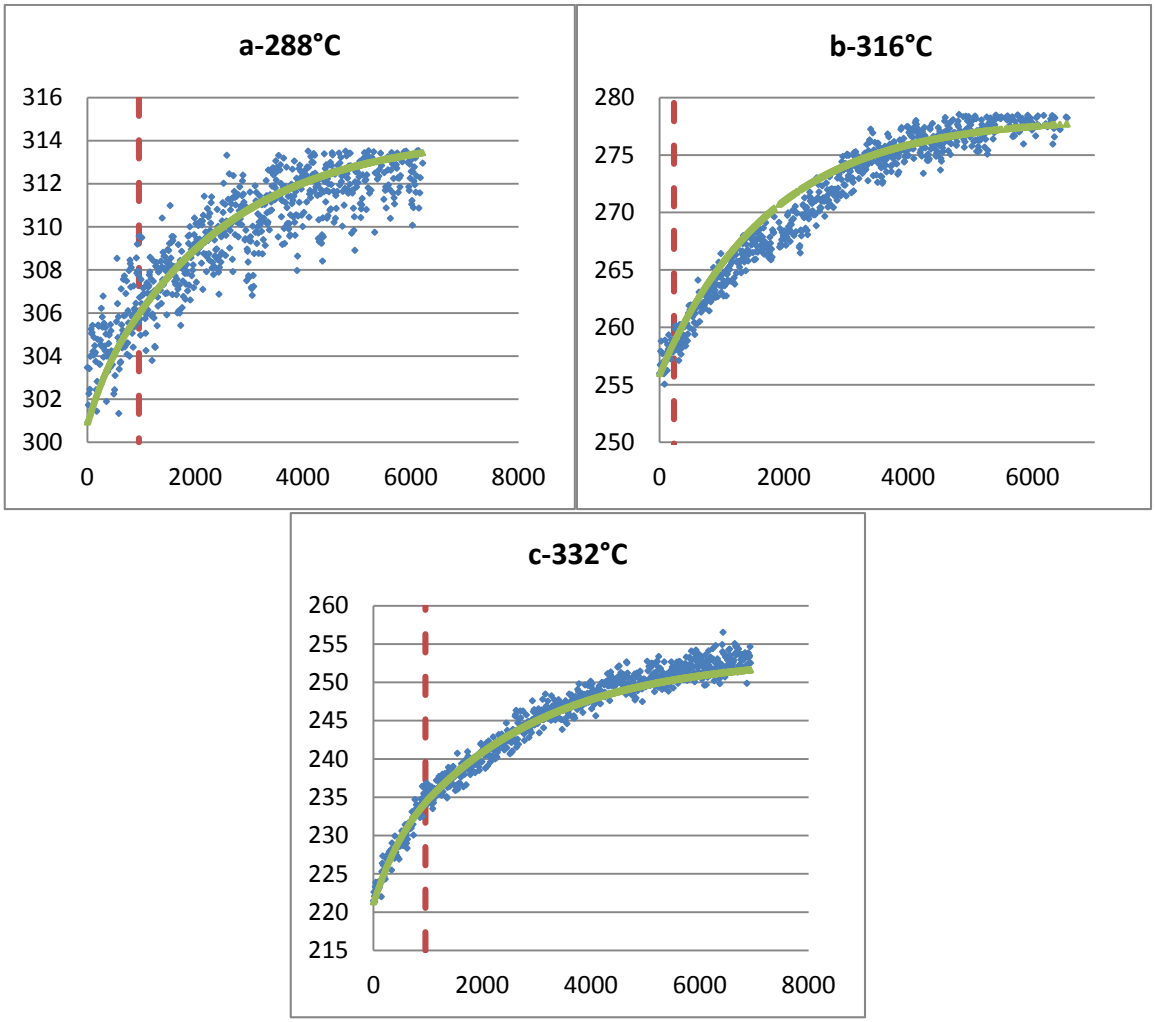


*Figure 3-38. Comparison of hydride evolution from the model done (with two regimes, shown in red) with the actual evolution (shown in blue), observed in situ at the APS on a 400 wt. ppm sample heated up to 550°C and cooled down to 288°C (a), 316°C (b) and 332°C (c). In each case, the y axis represents the hydrogen content as hydrides in wt.ppm and the x axis represents the holding time at the given temperature in seconds.*

All of the plotted graphs in Figure 3-36 to Figure 3-38 were plotted with their own individual pair of $\alpha^2$ and $\lambda^2$ values, with transition occurring at a specific time (showed by the red dashed line on each graph) that seem to be linked to supersaturated hydrogen content. The values of the supersaturated hydrogen content ($\Delta C$) at transition and the parameters $\alpha^2$ and $\lambda^2$ are noted for each sample and each holding temperatures in Table 3-9.

*Table 3-9 Precipitation parameters found for each samples and experiment runs at the Advanced Photon Source of the Argonne National Laboratory.*

| [H] content | Holding temp (°C) | $\lambda^2$ (x$10^{-5}$ $s^{-1}$) | $\alpha^2$ (x$10^{-4}$ $s^{-1}$) | ΔC (wt. ppm) |
|---|---|---|---|---|
| 400 | 288 | 2.27 | 4.00 | 8.25 |
| | 316 | 4.76 | 4.24 | 19.41 |
| | 332 | 2.87 | 5.57 | 17.94 |
| 541 | 288 | 6.13 | 2.76 | 4.47 |
| | 316 | 2.48 | 3.03 | 12.28 |
| | 332 | 2.85 | 4.45 | 14.74 |
| | 360 | 2.64 | 4.04 | 15.27 |
| | 380 | 3.01 | 4.88 | 16.16 |
| | 400 | 5.07 | 6.71 | 13.20 |
| 603 | 316 | 3.03 | 4.37 | 14.4 |
| | 332 | 2.13 | 3.65 | 17.06 |
| | 360 | 3.46 | 4.24 | 12.33 |
| | 380 | 5.79 | 8.64 | 15.02 |

As can be seen, a few of the plots in Figure 3-36 through Figure 3-38 show too much scatter in experimental data which made it difficult to use in detailed analysis. This is especially true for the data plotted in Figure 3-37(a), Figure 3-38(a) and (b). Figure 3-38(b) shows an apparent "plateau" in hydrogen precipitation around 2,000 seconds. It is unclear what caused this to happen, so it was decided to not use this data to determine the parameters of interest, as it would certainly affect the fit. Also, figures Figure 3-37(a) and Figure 3-38(a) show very scattered data points, which can cause errors when fitting. Therefore, it has also been decided not to use these plots to fit $\alpha^2$ and $\lambda^2$.

By performing this fit on all the experiments that were done during the APS trip, it was observed that the transition does not happen at a given time but rather, happens consistently near a particular supersaturated hydrogen content; more precisely when $\Delta C = 14.8 \pm 3.78\ \text{wt. ppm}$, where $\Delta C = C_{ss} - TSS_P$ is the average hydrogen in solid solution in super saturation state in all the considered samples (samples showed in Figure 3-36 through Figure 3-38 without plots (Figure 3-37(a), Figure 3-38(a) and (b))) and the error here is given to be two standard deviations (2σ) of the values of transitions. By examining the transition value of ΔC at transition of each sample at each holding temperature, a plot of ΔC versus temperature was obtained and is shown in Figure 3-39.

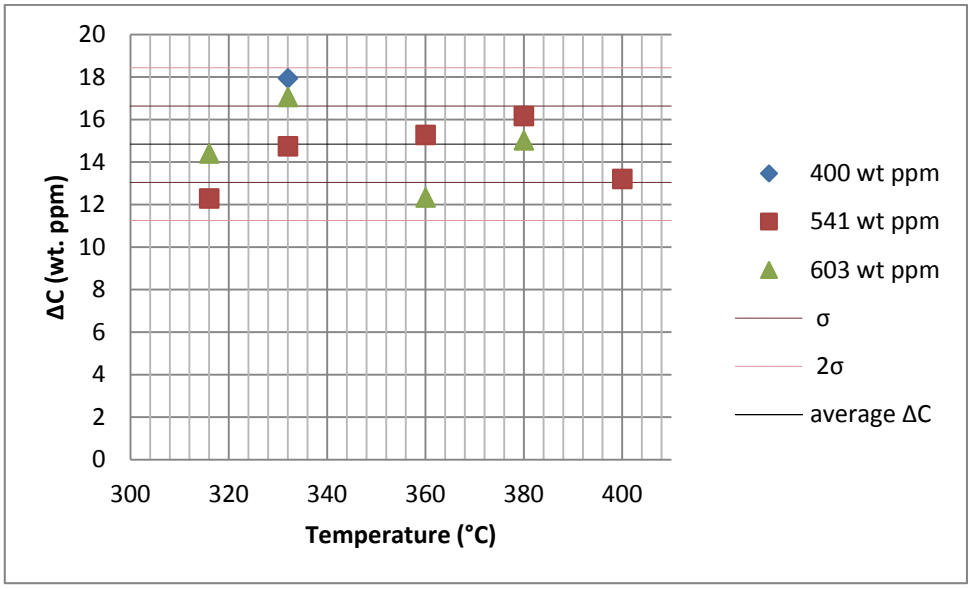


*Figure 3-39. Values of the super saturation of hydrogen in solid solution at transition for different samples and different temperatures.*

As can be observed, there is little effect of the temperature or overall hydrogen content on the transition supersaturated hydrogen content. Therefore, the value $\overline{\Delta C} = 14.8\ \text{wt. ppm}$ was used as the value for transition. One possible assumption is that the first regime comes from the nucleation of the hydrides and the second regime occurs when the driving force is not sufficient to create new nuclei and only growth happens. This would mean that the driving force is not sufficient to create new nuclei when the supersaturated hydrogen content in solid solution goes under 14.8 wt. ppm.

The values of $\ln(\alpha^2)$ and $\ln(\lambda^2)$ were plotted versus temperature (*Figure 3-40* and Figure 3-42) and seemed to fit Arrhenius laws, given by equations 3-36 and 3-37.

$$\alpha^2 = 0.055 \exp\left(-\frac{2927.6}{T[K]}\right) \qquad \text{Eq 3-36}$$

$$\lambda^2 = 0.107 \exp\left(-\frac{1843.8}{T[K]}\right) \qquad \text{Eq 3-37}$$

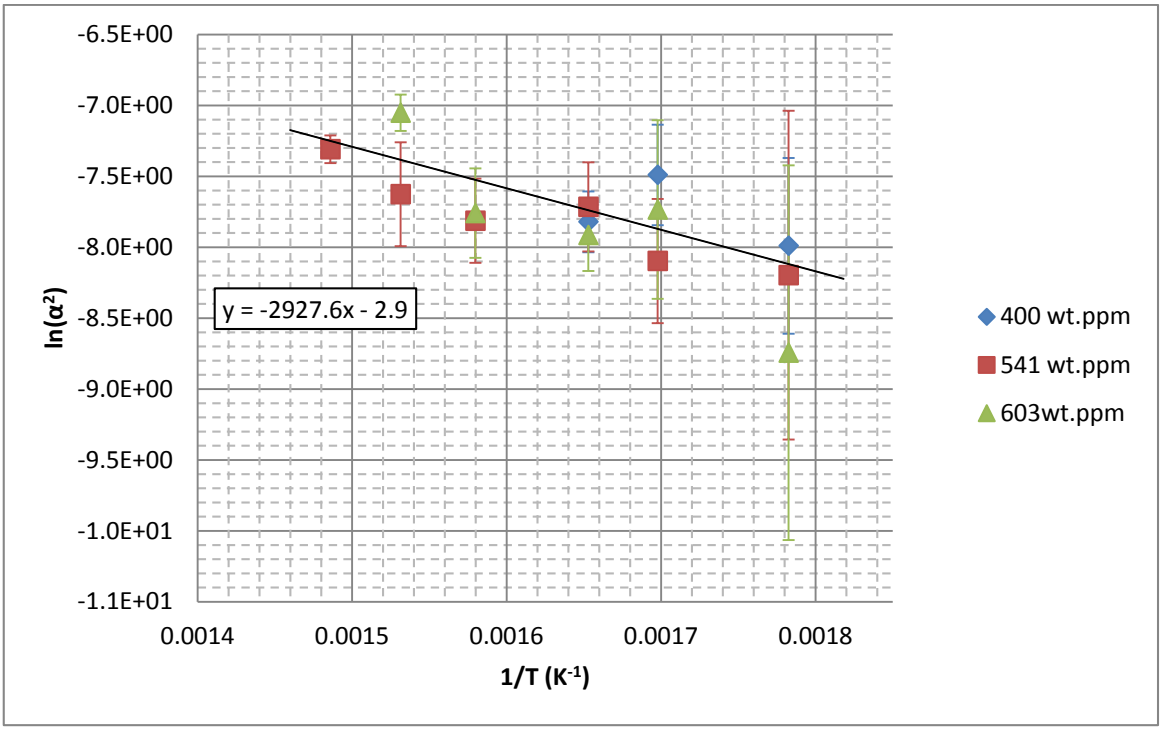


*Figure 3-40. Kinetic parameter in the second regime ln(α2) versus the inverse of temperature, for all three samples, studied during the APS experiment, at all temperatures to fit an Arrhenius law. Error bars are standard deviations from the fits of the curves in the second regime in the plots of Figure 3-32 and Figure 3-33.*

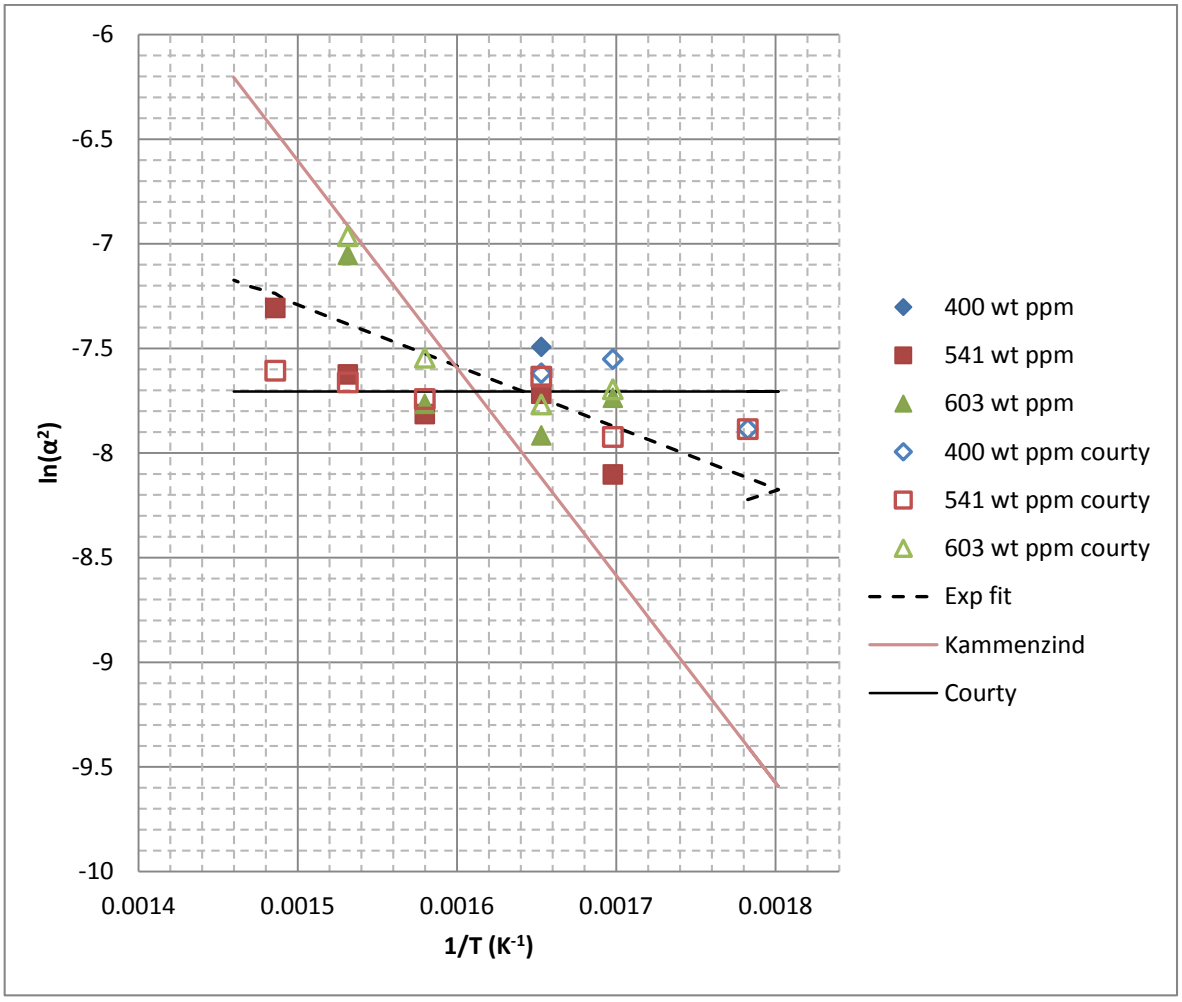


*Figure 3-41. Evolution of ln(α2) versus the inverse of temperature, for all three samples, studied during the APS experiment with O. Courty's analysis and the analysis done in this work. Kammenzind's reported Arrhenius law has also been included for comparison.*

According to equation 17, the range of variation of $\alpha^2$ between 288°C and 400°C is in general agreement with the values reported by Kammenzind [63]. The Arrhenius law found here has a weaker temperature dependence than observed by Kammenzind but the values in each work are within the same range. Kammenzind found $\alpha^2$ to be between $8.25 \times 10^{-5}\ s^{-1}$ at 288°C and $1.56 \times 10^{-3}\ s^{-1}$ at 400°C when the fit here gives values ranging from $2.68 \times 10^{-4}\ s^{-1}$ at 288°C and $7.19 \times 10^{-4}\ s^{-1}$ at 400°C. The plot in figure 3-41 compares graphically the values found with this analysis to the ones found both by Kammenzind and O. Courty. It also confirms that all of the values reported are within the same range but show different variation with temperature.

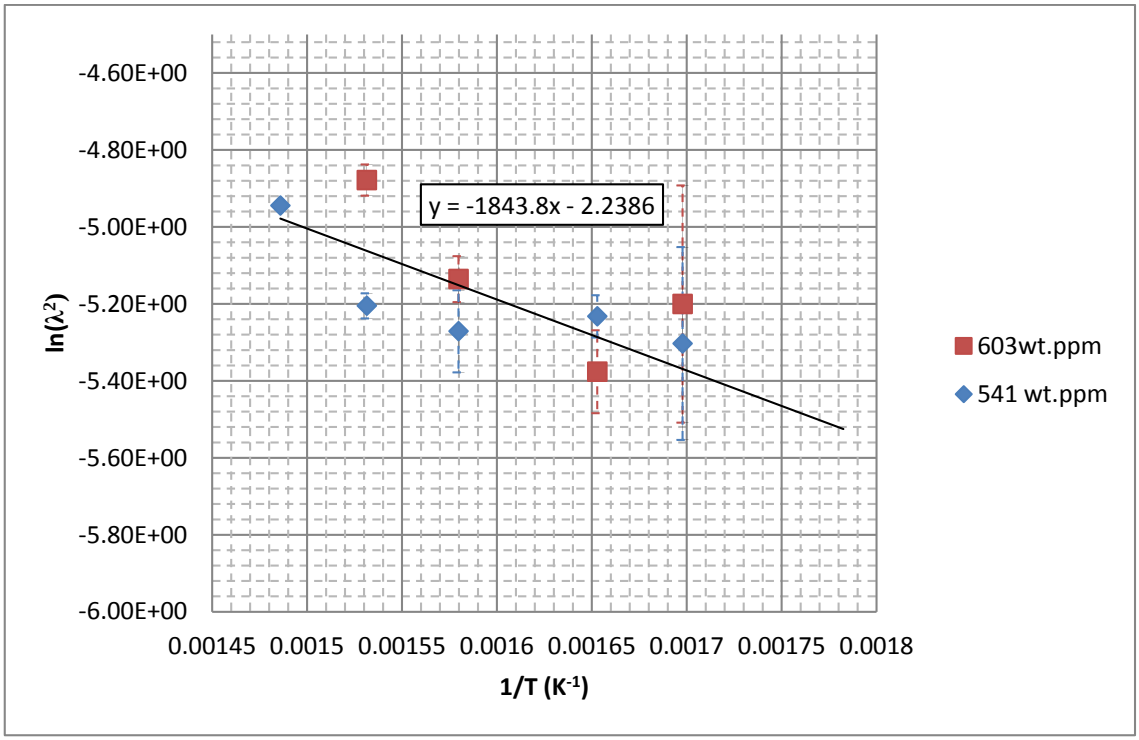


*Figure 3-42. Evolution of $ln(\lambda^2)$ versus the inverse of temperature, for all three samples, studied during the APS experiment, at all temperatures to fit an Arrhenius law. Error bars are standard deviations from the fits of the curves in the first regime.*

*Figure 3-40* and Figure 3-42 show that two different kinetics regimes are present during fast cooling and that they are both temperature dependent. Although it is unclear what the two regimes are, it has been observed that under fast cooling conditions something more than the Marino model is needed to satisfactorily model the precipitation kinetics of zirconium hydrides in zirconium alloys. The analysis also indicates that the Marino model is valid when the supersaturated hydrogen content in solid solution is below 14.8 wt.ppm.

## 3.2 Assembly of available PIE measurements of hydrogen distribution data

In the last report, an update to the hydrogen precipitation model was made. Since then, this model has been uploaded into BISON and was tested by simulating the life of two pins that were very well characterized in 1993 by J.H [20]. Zhang. His study showed the hydrogen distribution in 16 zones in each reactor fuel rods, described by Figure 3-43:

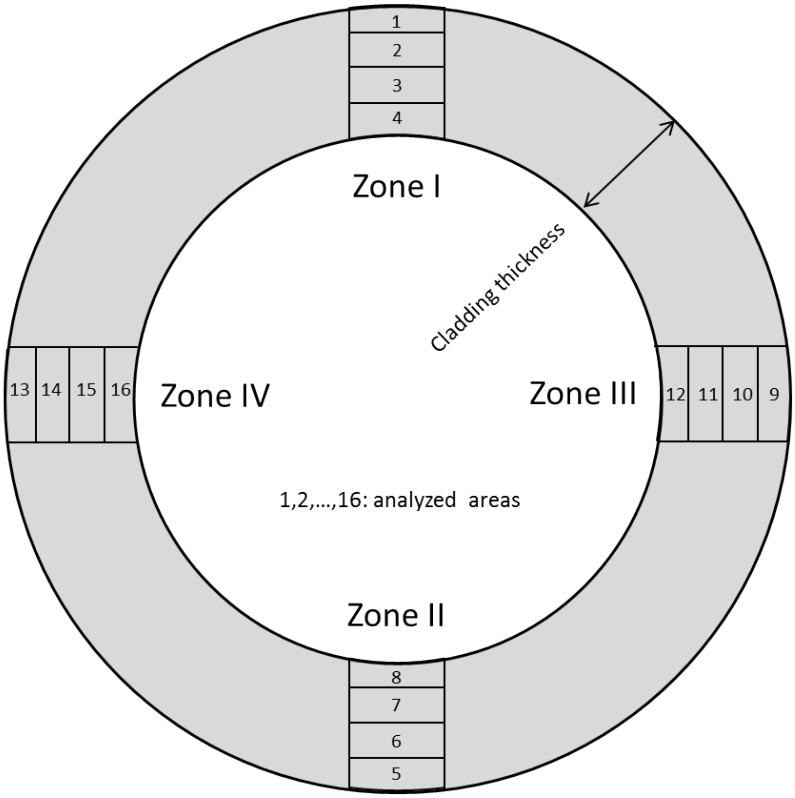


*Figure 3-43: Analyzed areas in Zhang's thesis [20]*

In the following part we will refer to areas 1, 5, 9 and 13 as layer 1; areas 2, 6, 10 and 14 as layer 2; areas 3, 7, 11 and 15 as layer 3 and the others as layer 4.

### 3.2.1 Gravelines

The Gravelines' fuel pin is characterized by the parameters given in table 3-10 and by the power profile given in Figure 3-44. Given this data plus the hydrogen content that was measured by vacuum hot extraction and by image analysis in hot cells by J.-H. Zhang [27], it is possible to simulate the hydrogen distribution in this portion of cladding with BISON and compare it to the experimental data reported in Table 3-10.

*Table 3-10 Gravelines' fuel pin and reactor characteristics*

| ***Clad Material*** | ***Zircaloy-4*** | ***Number of cycles*** | ***5*** |
|---|---|---|---|
| ***Fuel*** | *$UO_2$* | ***Enrichment (%5U)*** | *4.5* |
| ***Z position (mm)*** | *3250* | ***Burnup (MWd/tU)*** | *58230* |
| ***Outside diameter (mm)*** | *9.49* | ***Inside diameter (mm)*** | *8.36* |
| ***Pressure (bars)*** | *155* | ***Mass Flux (g cm-2s-1)*** | *314* |
| ***Inlet Enthalpy (J $g^{-1}$)*** | *1264* | ***Inlet Temperature (°C)*** | *286* |
| ***Outlet Temperature (°C)*** | *323* | | |

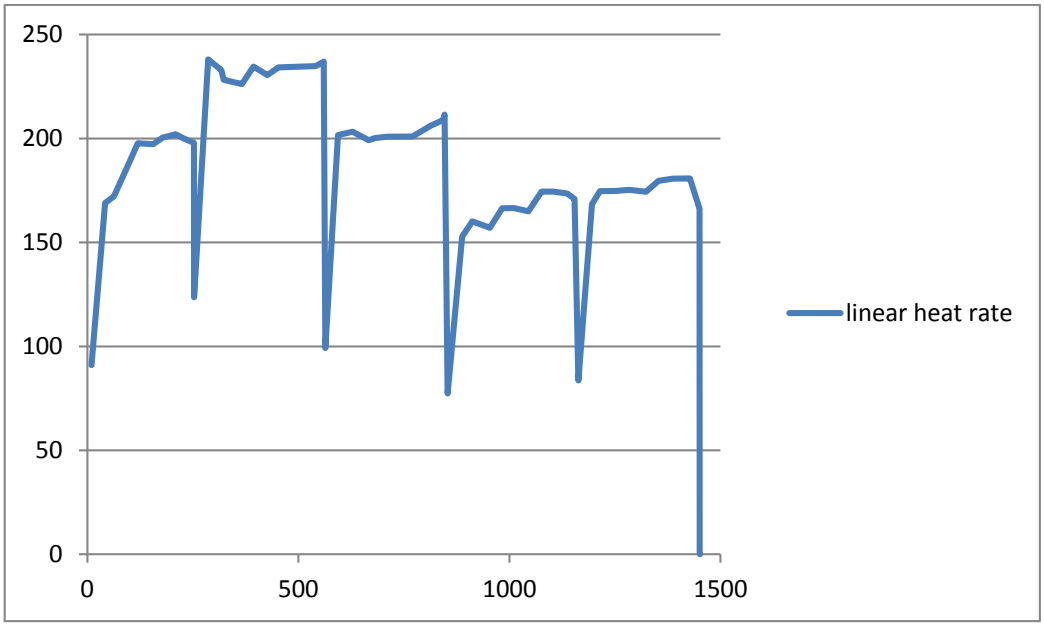


*Figure 3-44: Gravelines' power history*

*Table 3-11 Hydrogen experimental distribution determined by Image Analysis, quantities are given in wt.ppm.*

| Radial position (µm) | Top | Bottom | Right | Left | Average [H] per layer |
|---|---|---|---|---|---|
| **499** | 859* | 765* | 1311* | 1078* | **1003*** |
| **356** | 409 | 213 | 514 | 481 | **403±80** |
| **214** | 157 | 275 | 198 | 192 | **205±80** |
| **71** | 183 | 130 | 196 | 178 | **172±80** |
| **Average** | **402** | **346** | **554** | **483** | **392±40** |

*values calculated to account for the difference between the hydrogen content measured by VHE.

Since a hydrogen rim is formed, it cannot be measured well with image analysis; therefore, the excess amount of hydrogen is added in layer 1. This calculated content has been made in such way to keep the ratio of hydrogen present in each zone the same.

The data shows an azimuthal dependence here. However, no data was given as to neighboring pin power profile, presence of a water rod or the presence of spacer grids that could provoke these azimuthal variations. In that regard, only the averaged values over the azimuth were used.

### 3.2.2 Cruas

The Cruas' fuel pin is characterized by the parameters given in Table 3-12 and by the power profile given in Figure 3-45. Given this data plus the hydrogen content that was measured by vacuum hot extraction and by image analysis in hot cells by J.-H. Zhang [27], it is possible to simulate the hydrogen distribution in this portion of cladding with BISON and compare it to the experimental data reported in Table 3-13.

*Table 3-12 Cruas fuel pin and reactor characteristics*

| Clad Material | Zircaloy-4 | Number of cycles | 5 |
|---|---|---|---|
| Fuel | $UO_2$ | Enrichment (%5U) | 3.25 |
| Z position (mm) | 3083 | Burnup (MWd/tU) | 39635 |
| Outside diameter (mm) | 9.51 | Inside diameter (mm) | 8.35 |
| Pressure (bars) | 155 | Mass Flux (g cm-2s-1) | 314 |
| Inlet Enthalpy (J $g^{-1}$) | 1264 | Inlet Temperature (°C) | 286 |
| Outlet Temperature (°C) | 323 | | |

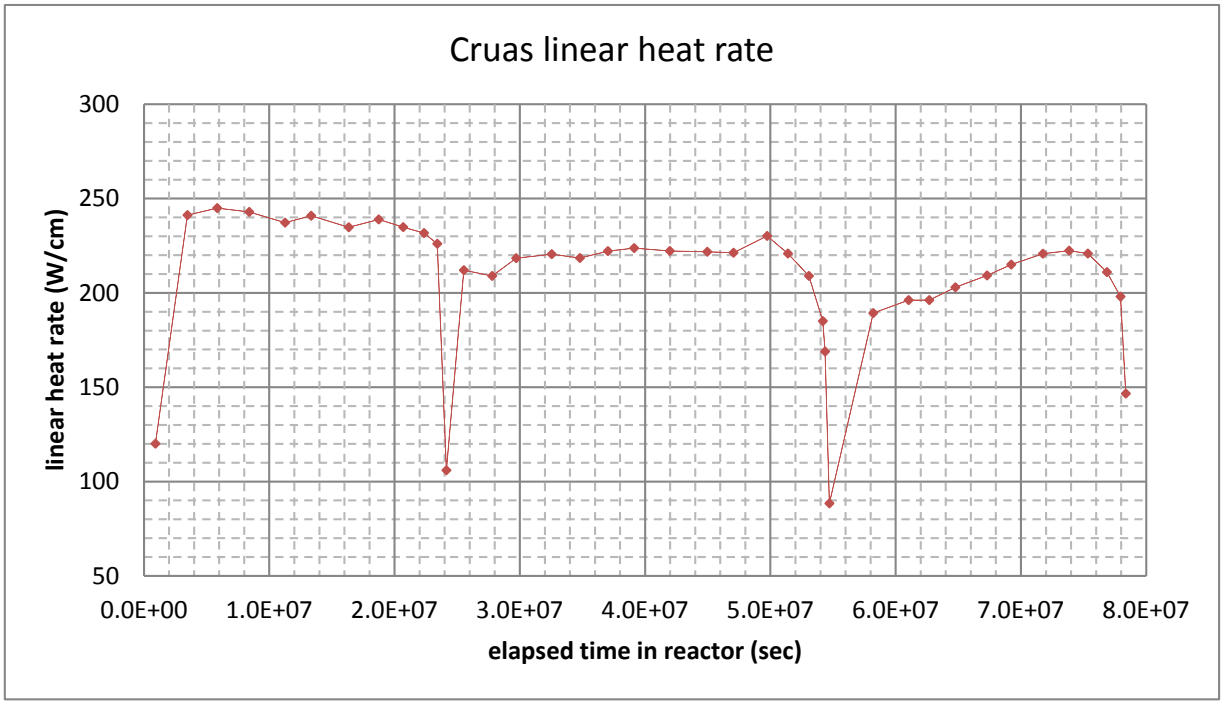


*Figure 3-45: Cruas' power history*

*Table 3-13 Cruas fuel pin and reactor characteristics*

| Radial position (µm) | Top | Bottom | Right | left | Average [H] per layer |
|---|---|---|---|---|---|
| **499** | 668 | 774 | 1243 | 651 | **834*** |
| **356** | 78 | 234 | 228 | 78 | **154±80** |
| **214** | 111 | 101 | 106 | 102 | **105±80** |
| **71** | 127 | 155 | 155 | 197 | **159±80** |
| **Average** | **246** | **316** | **433** | **257** | **313** |

*values calculated to account for the difference between the hydrogen content measured by VHE. Since a hydrogen rim is formed, it cannot be measured well with image analysis; therefore, the excess amount of hydrogen is added in layer 1. This calculated content has been made in such way to keep the ratio of hydrogen present in each zone the same.

## 3.3 Additional measurements and targeted experiments to use the code in range of temperature gradient and hydrogen concentration conditions

### 3.3.1 Literature Review

The work in this section was focused on making the model more robust. While the kinetics parameter $\alpha^2$ has been measured previously in this project, the model also depends on the different solubility values. The solubility values differ greatly in the literature. A literature review of the solubility limit measurements was made to find the best values and implement them in the BISON code. This study was interested in the work of Kearns [28] McMinn [35], Une [64], Tang [65], Vizcaino [66], Pan [34], Slattery [67], Colas [27], Zanelatto [68] and Sawatzky [69]. The solubility limits curves for precipitation and dissolution are given in Figure 3-46 and Figure 3-47.

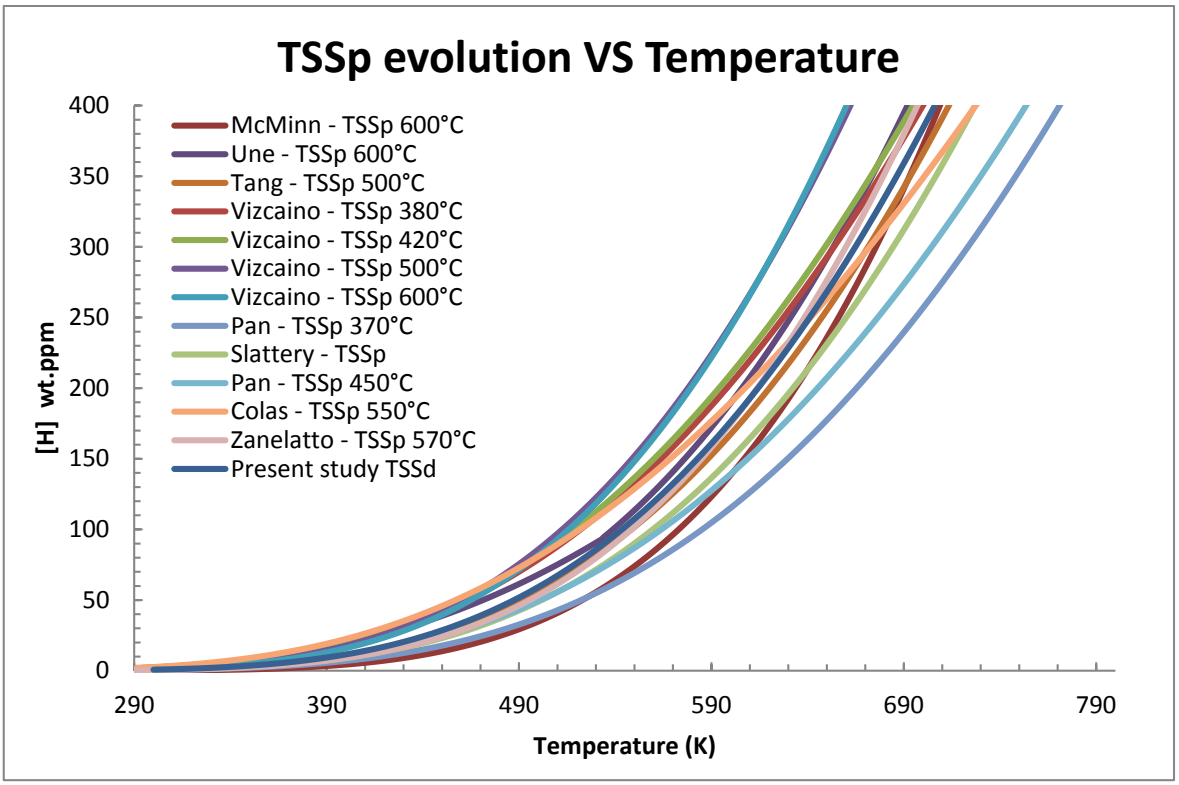


*Figure 3-46: Fitted values of $TSS_P$ from literature plotted versus temperature.*

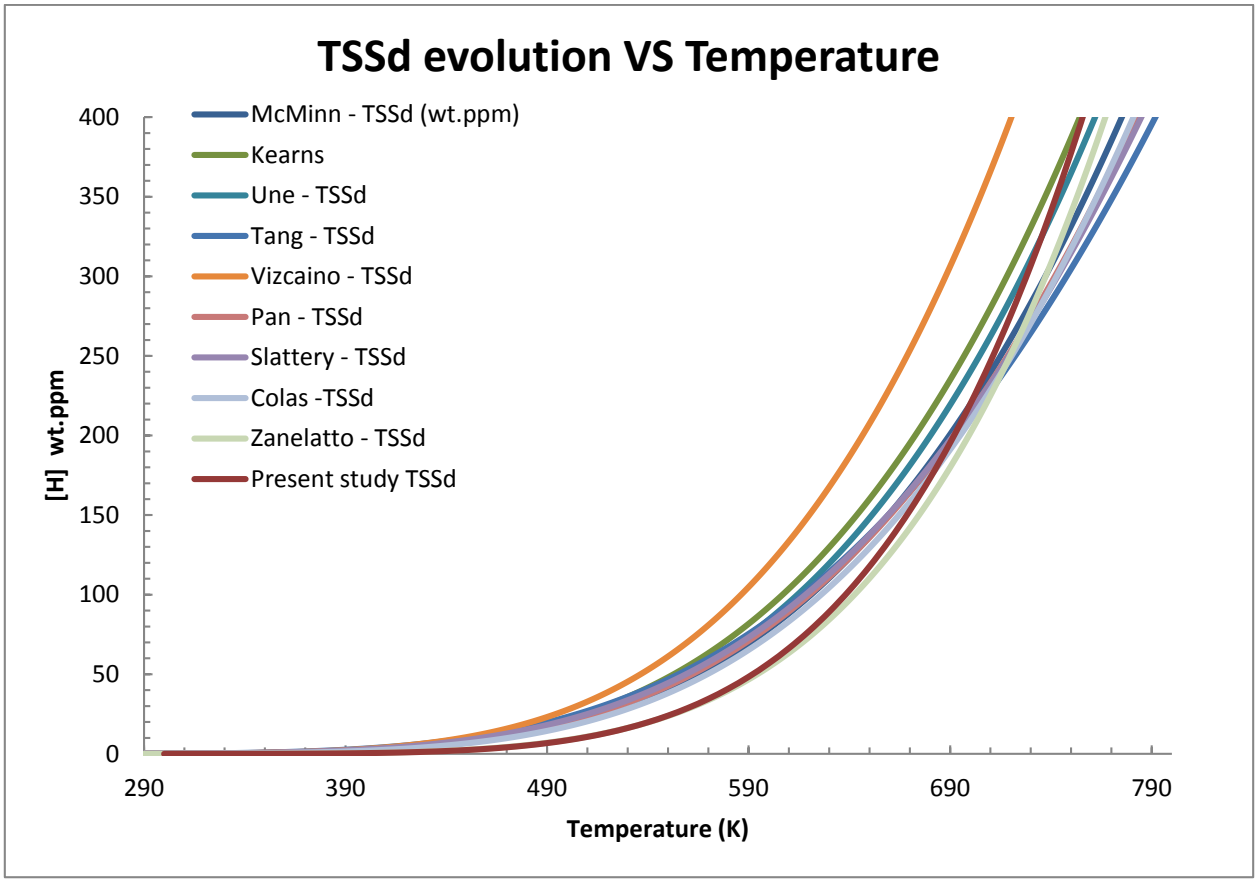


*Figure 3-47: Fitted values of $TSS_D$ from literature plotted versus temperature*

While the $TSS_P$ values found vary significantly, the $TSS_D$ values seem to show better agreement. The solubility limit can be modeled by an Arrhenius law in the form of:

$$TSS = C_0 \exp -\frac{Q}{RT}$$

The different $C_0$ and Q from literature were taken for $TSS_D$, averaged and the outliers (greater than the standard deviation) were removed. An average value of $TSS_D$ was then defined by:

$$\overline{TSS_D} = \overline{C_0} \exp \frac{\overline{Q}}{RT}$$

where $\overline{C_0}$ and $\overline{Q}$ are the average $C_0$ and average Q respectively. The equation obtained is the following:

$$TSS_D = 101999 \cdot \exp\left(-\frac{35458.67}{RT}\right)$$

The value for $TSS_P$ is harder to obtain since so much scatter is observed. The $TSS_P$ value chosen to be the best here was the one that lay close to the median of the different values. This value that satisfied this criterion was the value given by K. Une [64], with a slight modification. Une observed a change in slope in his values, which was not observed by any other authors. The value for $TSS_P$ chosen here did not include the change in slope. A graph representing different experimental data point versus the fits is represented in Figure 3-48.

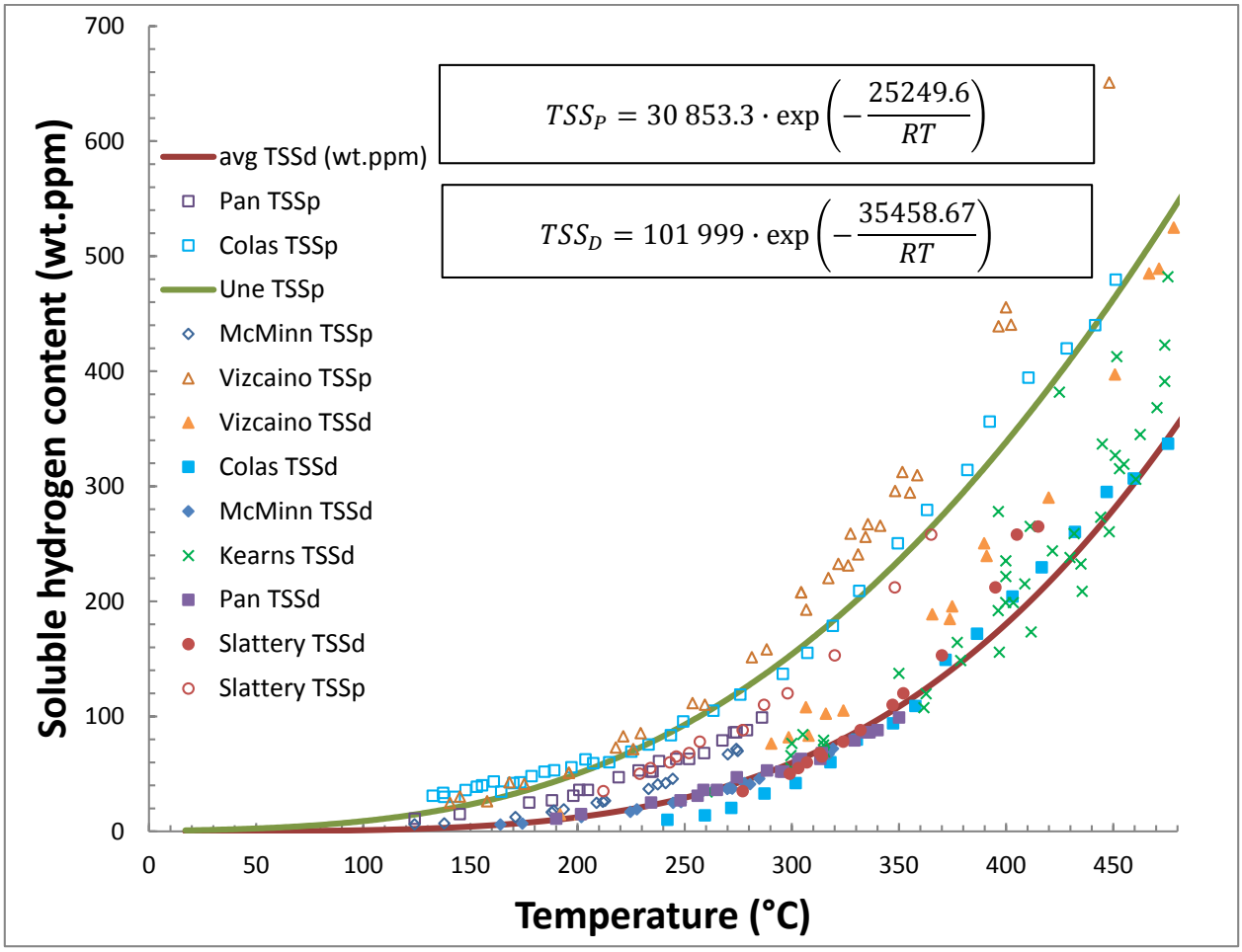


*Figure 3-48: Experimental values of solubility experiments compared to the average value determined in this study*

### 3.3.2 Advanced Photon Source (ANL) Experiments

During operating conditions however, the cladding can be subject to stresses and strains. It has been suggested in the past [70] that strains could change the hydrogen partial pressure in the cladding and therefore change the solubility limit. Therefore, a set of experiment was planned to be performed at Argonne National Laboratory, testing for stress influence on the solubility limits and the effect of thermal cycling on solubility as well.

Thermal cycling from 180°C to 540°C with a hold times of 10mn at high temperature and 20mn at low temperature was performed with no stress. Heating and cooling was performed at 10°C/mn. This experiment showed no influence of thermal cycling on the solubility limits. Little or no influence of stress was observed. All samples underwent 5 cycles: 1 cycle with no stress and 4 cycles at the chosen applied stress, with the applied stresses chosen to be 0, 100, 170 and 200 MPa. The results are given in Figure 3-49 through Figure 3-52.

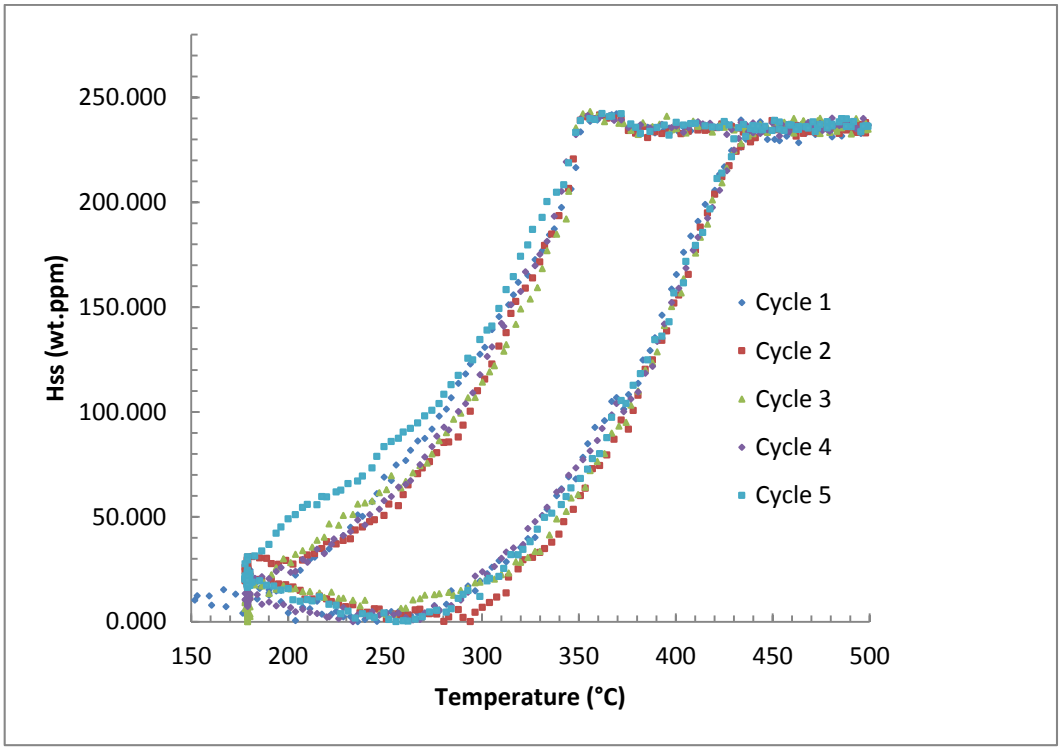


*Figure 3-49: Evolution of hydrogen in solid solution with an applied stress of 0MPa*

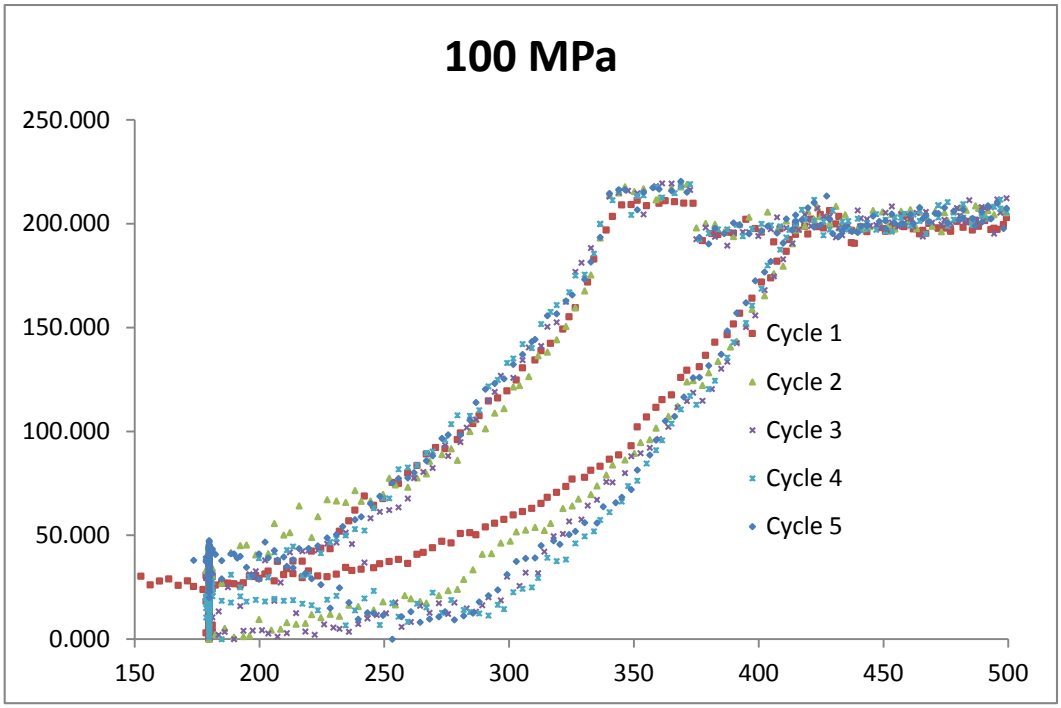


*Figure 3-50: Evolution of hydrogen in solid solution with an applied stress of 100MPa*

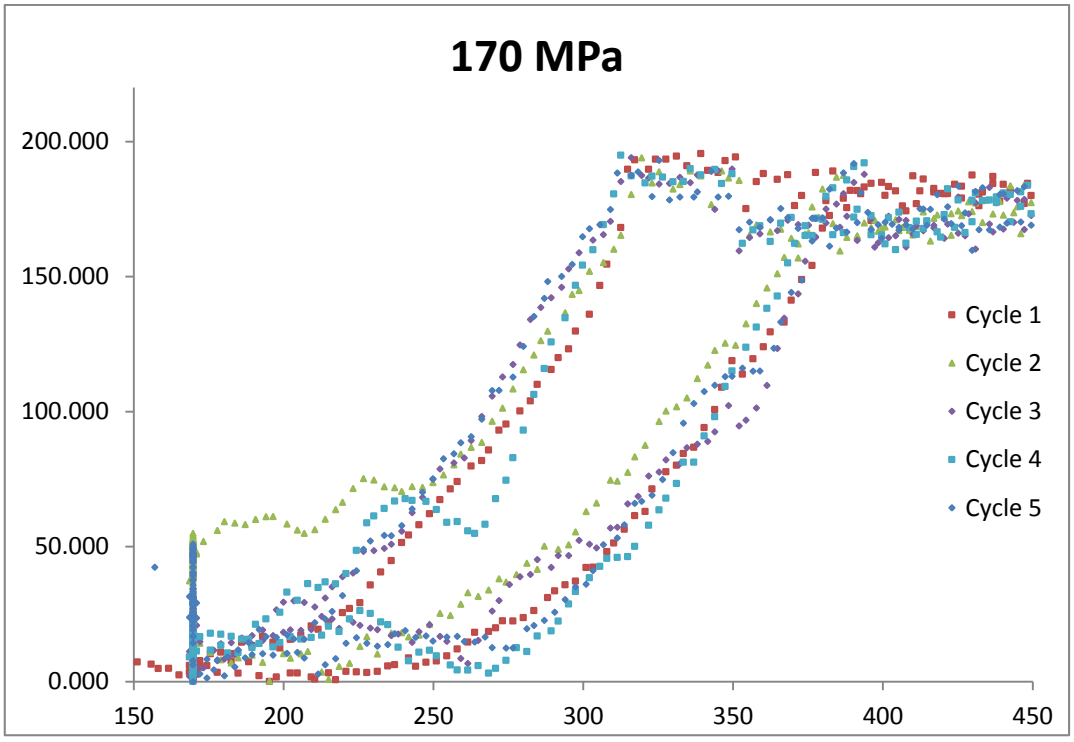


*Figure 3-51: Evolution of hydrogen in solid solution with an applied stress of 170MPa*

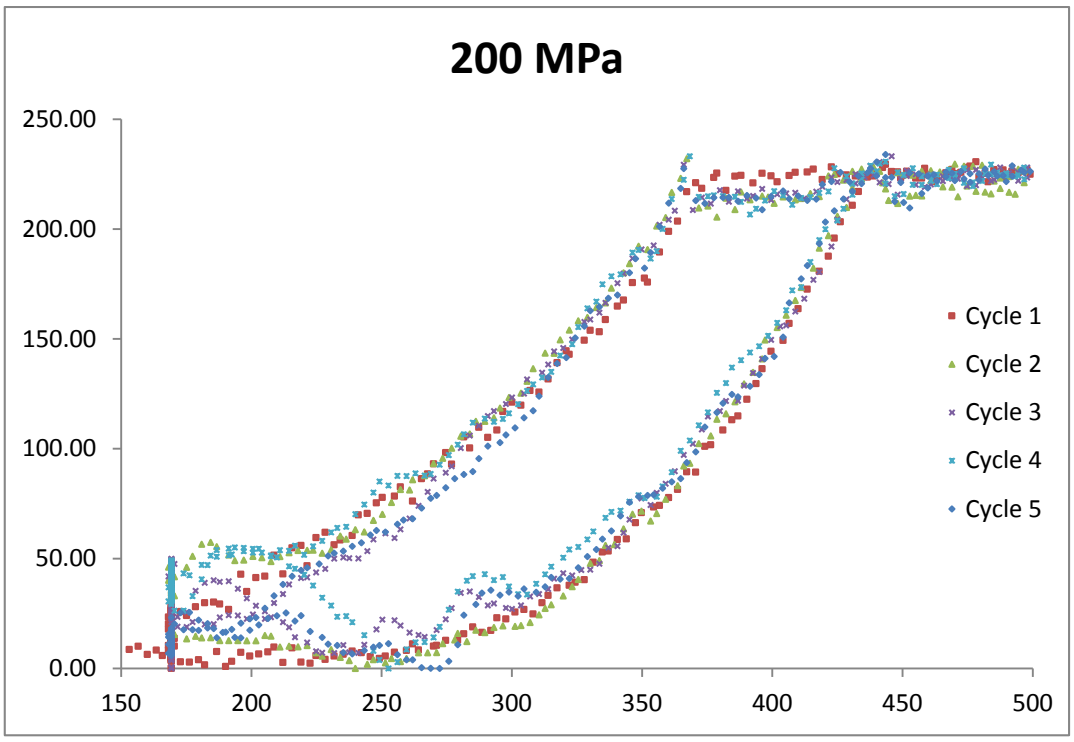


*Figure 3-52: Evolution of hydrogen in solid solution with an applied stress of 200MPa*

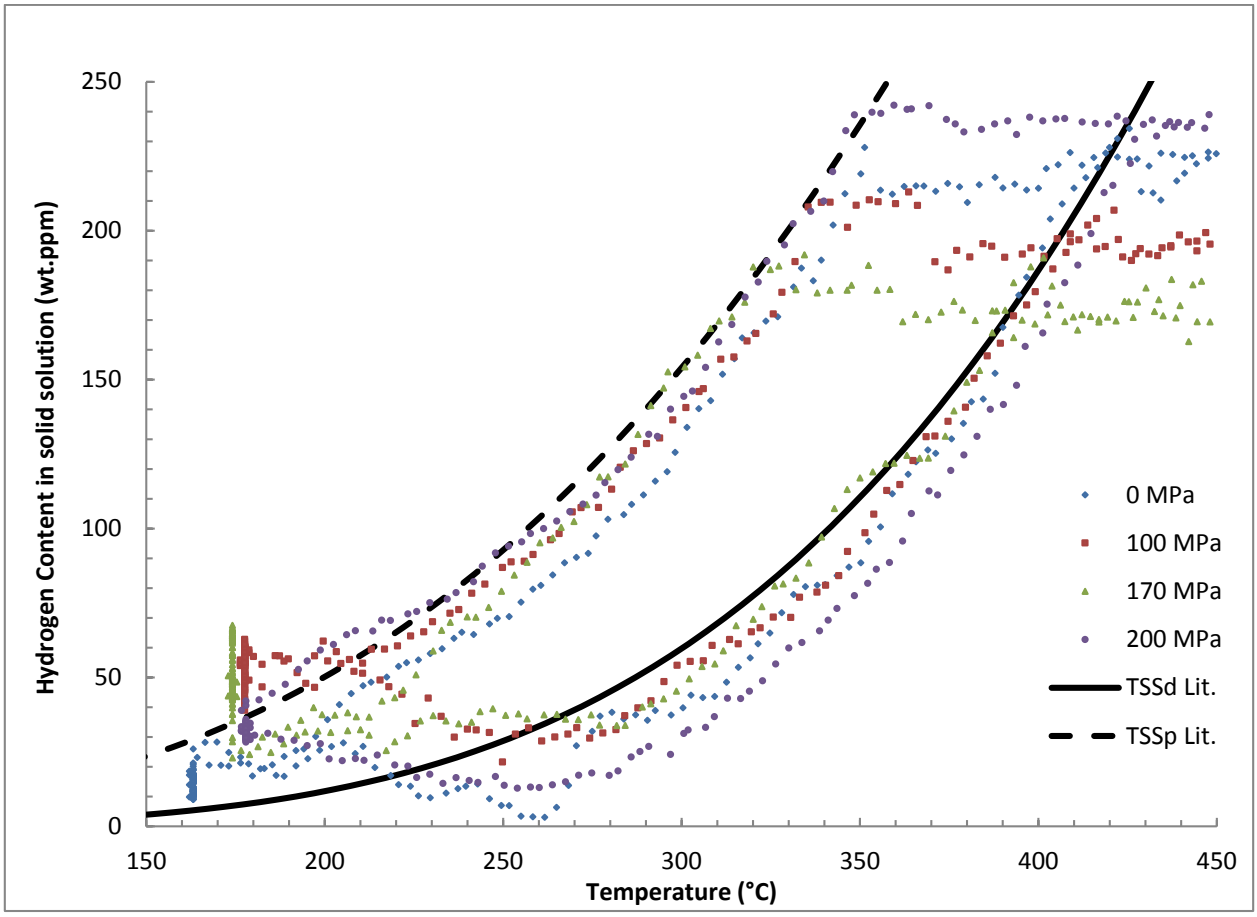


*Figure 3-53: Comparison of the evolution of the hydrogen content in solid solution on the last cycle for each sample.*

As it can be seen, thermal cycling does not seem to have a significant effect on hydrogen solubility. However, we can see in Figure 3-53 that the solubility of hydrogen at 200MPa is consistently lower than the other samples for dissolution, and that the solubility for precipitation is consistently lower in when no stress is applied.

As a conclusion, this study has showed that thermal cycling does not affect hydrogen solubility in the Zirconium matrix both for precipitation and dissolution. A little effect of stress has been observed on the solubility. It can be seen that when hydrides are reoriented, it is harder to dissolve them. On the other hand, it has also been observed that the hydrides are slightly easier to precipitate when no stress is applied.

### 3.3.3 Characterization of hysteresis

*Table 3-14 Heat treatment undergone by the sample studied at Argonne National Laboratory*

| step | Initial Temperature (°C) | Final Temperature (°C) | Hold time (mn) | Temperature rate of change (°C/min) |
|---|---|---|---|---|
| 1 | 27 | 425 | 10 | 10 |
| 2 | 425 | 170 | 20 | 10 |
| 3 | 170 | 385 | 10 | 10 |
| 4 | 385 | 285 | 20 | 10 |

| | | | | |
|---|---|---|---|---|
| 5 | 285 | 425 | 10 | 10 |
| 6 | 425 | 150 | 20 | 10 |
| 7 | 425 | 40 | 0 | Air cooled |

The material used for this experiment was a Zyrcaloy-4 sheet, hydrided by gaseous charging in an atmosphere of 12.5% Hydrogen and Argon balance. The sample was analyzed for hydrogen content using vacuum hot extraction by Luvak Inc. and was tested to hold 255±43 wt.ppm. The sample was then machined in a dog bone to be held at the 1-ID beamline at Argonne National Laboratory's Advanced Photon Source. 18 transmission X-Ray diffraction patterns were then collected every 9 seconds while a heat treatment described in Table 3-14 was applied to the sample. The evolution of the δ-hydride (111) peak integrated intensity was studied with respect to time and temperature. This thermal heat treatment was performed to study the hysteresis presence in the following way:

a) **Steps 1-2** allowed for the study of the behavior of the system when all hydrides were dissolved from room temperature and how the precipitation kinetics is with no hydrides present in the system.

b) **Steps 3-4** allowed for the study of the behavior of the system when hydrides are still present when precipitation occurs.

c) **Steps 5-6** allowed for the study of the behavior of the hydrides when heated up right after precipitation occurred.

The integrated peak intensity of the δ(111) were related to the hydrogen in solid solution by the following formulae:

$$C_{ss}(t) = C_{VHE}\left(1 - \frac{I(t) - I_{noise}}{I_m - I_{noise}}\right)$$

were $C_{SS}(t)$ is the hydrogen content in solid solution at a given time t, $C_{VHE}$ is the hydrogen content measured by Vacuum Hot Extraction, I(t) is the hydride integrated peak intensity at a given time t, $I_{noise}$ is the integrated peak intensity average noise (measured at high temperature) and $I_m$ is the maximum hydride peak measured throughout the experiment.

A plot of Css versus temperature is given in Figure 3-54. It is clear from this graph that hydrides start precipitating as soon as the temperature is lowered (path A-B), therefore confirming the result found by Colas 125[71]. Another interesting result found here is the reduction of the hydrogen content in solid solution when being held at temperature for twenty minutes at 283°C (path B-C in Figure 3-54). The hydrogen content in solid solution is initially about 120 wt.ppm (point B) and is about 97 wt.ppm when the temperature is increased to start step 5 (point C). This shows that the hydrogen in solid solution is going away from the $TSS_P$, suggesting that the $TSS_P$ may not be an equilibrium value.

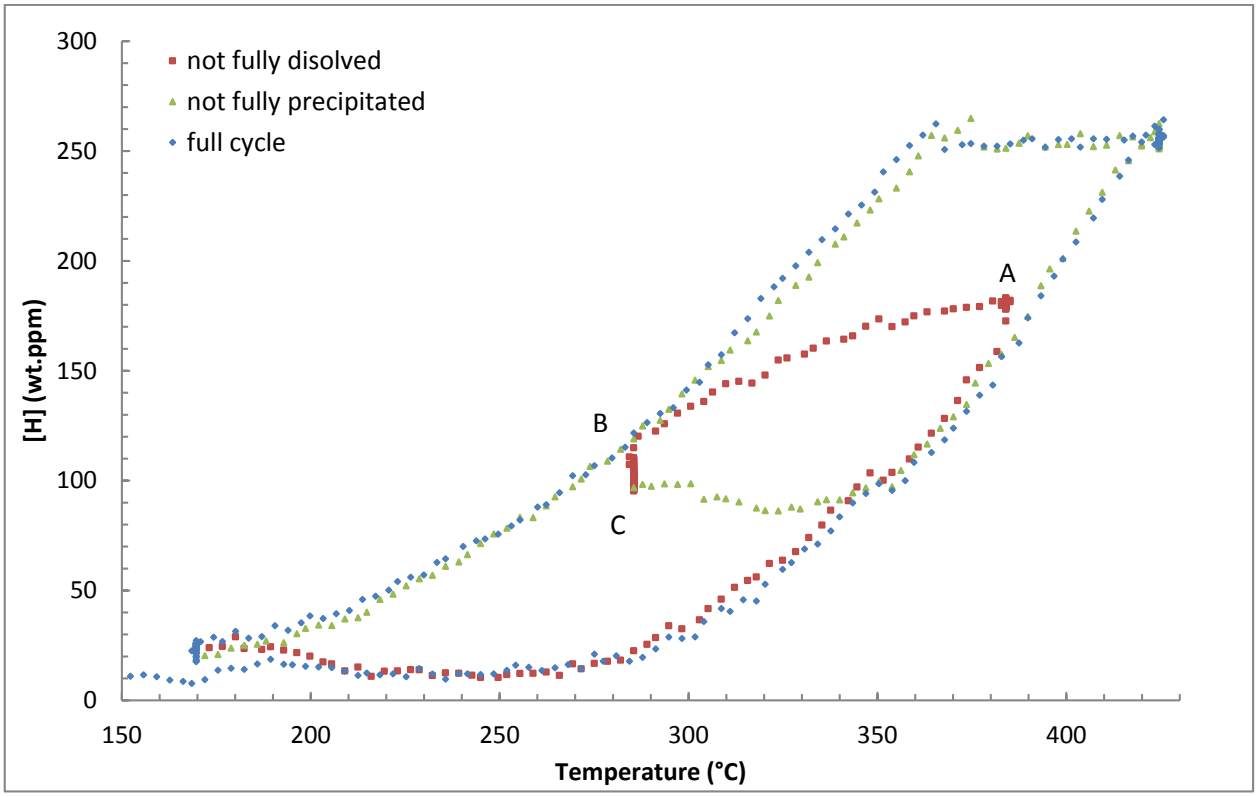


*Figure 3-54: Evolution of hydrogen content in solid solution versus temperature for the heat treatment presented in table 3-14.*

### 3.3.4 Dissolution parameter

Hydrogen precipitation has been studied before by Kammenzind, Courty or Marino. However, no measurements of the dissolution parameter have been performed. This part shows an attempt to measure zirconium hydride dissolution kinetics parameter $\beta^2$ as presented by courty [72]. The parameter was measured by using the data presented in Figure 3-57 during the dissolution phase. $TSS_D$ curves are very consistent in literature, as seen in Figure 3-57 and in [27] [28], [34], [35], [64], [68] and [73]. Considering the difference between the literature curves and the experimental curve, it is assumed that the dissolution here is limited by the dissolution mechanism and not the heating rate. Therefore, an attempt at calculating $\beta^2$ has been made.

According to O. Courty et al. [72], the dissolution is governed by the following equation:

$$\frac{dC_{ss}}{dt} = \beta^2(C_{SS} - TSS_D) \qquad \text{Eq 3-38}$$

To determine $\beta^2$ at each time step, equation 5 was discretized and was determined by solving:

$$\beta^2\left(t + \frac{\Delta t}{2}\right) = \frac{C_{ss}(t+\Delta t) - C_{ss}(t)}{\left(C_{SS}(t) - TSS_D\left(t + \frac{\Delta t}{2}\right)\right)\Delta t} \qquad \textit{Eq 3-39}$$

The value for $\beta^2$ obtained is therefore an averaged value over the time step and can therefore lead to errors. The time constant for dissolution is defined as being $\tau_D = \frac{1}{\beta^2}$. A Time Temperature Transformation diagram has been made using the dissolution data in Figure 3-57: Precipitation of hydrogen at different temperatures in a sample containing 541 wt.ppm of hydrogen. Evolution of the

hydrogen content in solid solution as a function of temperature, and is presented in Figure 3-55, for $5\tau_D$ corresponding to 99.3% of steady state.

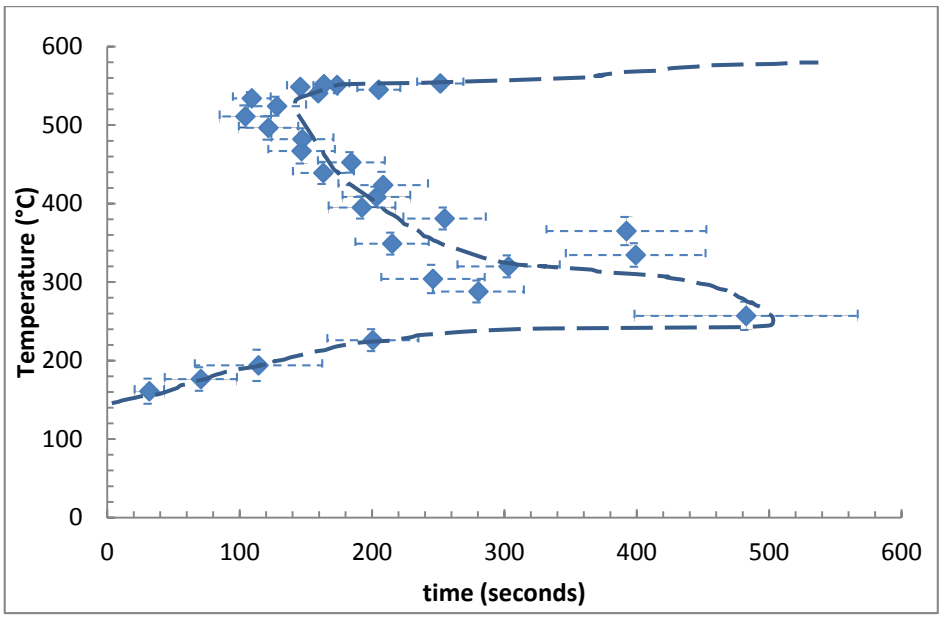


*Figure 3-55: Time Temperature Transformation diagram for zirconium hydride dissolution for T ϵ [161°C; 553°C] in a sample containing 541 wt.ppm of hydrogen, being heated from 120°C to 553°C at a rate of 1.8°C/s.*

This diagram shows the typical shape of a TTT diagram and offers a first measurement of dissolution kinetics. However, it is expected to see dissolution kinetics get slower at low temperatures as hydrogen is in hydride form at room temperature. The TTT diagram was therefore investigated on the two other samples that were used in Courty et al.'s experiments [60] to (i) measure the dissolution kinetics at lower temperatures and (ii) to investigate the dependence of dissolution kinetics on hydrogen content. The TTT diagrams for all three samples are presented in Figure 3-56.

It can be seen that the TTT diagram is hydrogen content dependent: a shift towards longer time scales can be observed with decrease in hydrogen content. It can also be observed that dissolution kinetics become very slow closer to room temperature. The TTT diagram for the sample containing 603 wt.ppm shows that, under 40°C, dissolution becomes very slow.

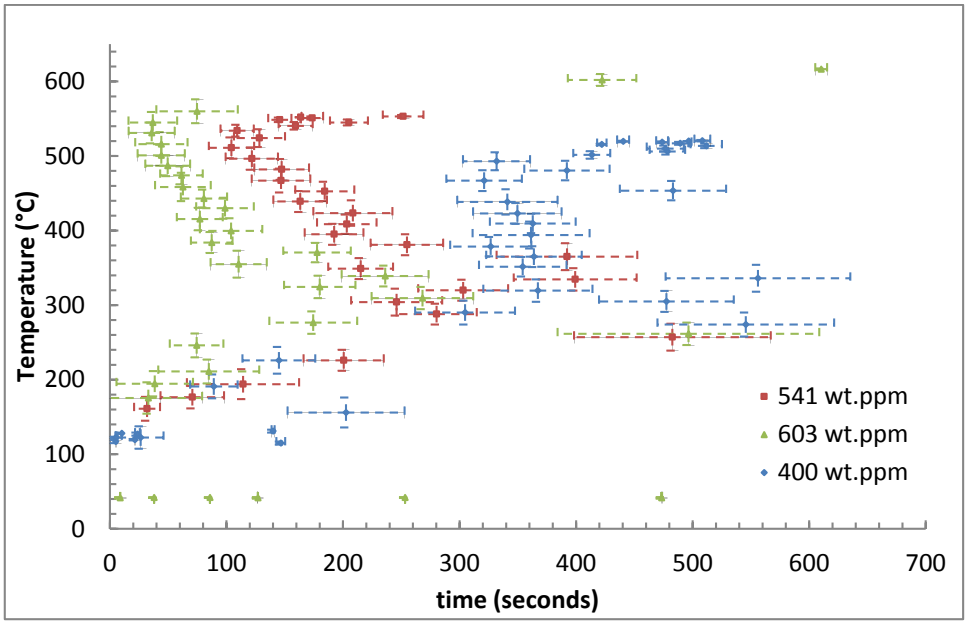


*Figure 3-56: Time Temperature Transformation diagram for zirconium hydride dissolution for three different samples, containing 603, 541 and 400 wt.ppm of hydrogen. The cooling rate in the experiments were*

### 3.3.5 Model modification

The direct onset of precipitation when hydrides are present coupled with the decrease of hydrogen in solid solution when the hydrogen content seems to be following the $TSS_P$ suggest that hydrogen precipitation is possible when the hydrogen content in solid solution is between $TSS_D$ and $TSS_P$. This is not in agreement with what had been suggested in the previous hydrogen models [72][74]. To verify if precipitation is occurring between the two TSS curves, O. Courty's data from his APS experiments [60] was plotted the same way the presented experiment was plotted in Figure 3-54. Figure 3-57 represents the data obtained for one sample (containing 541 wt.ppm) when hydrogen in solid solution is plotted versus temperature.

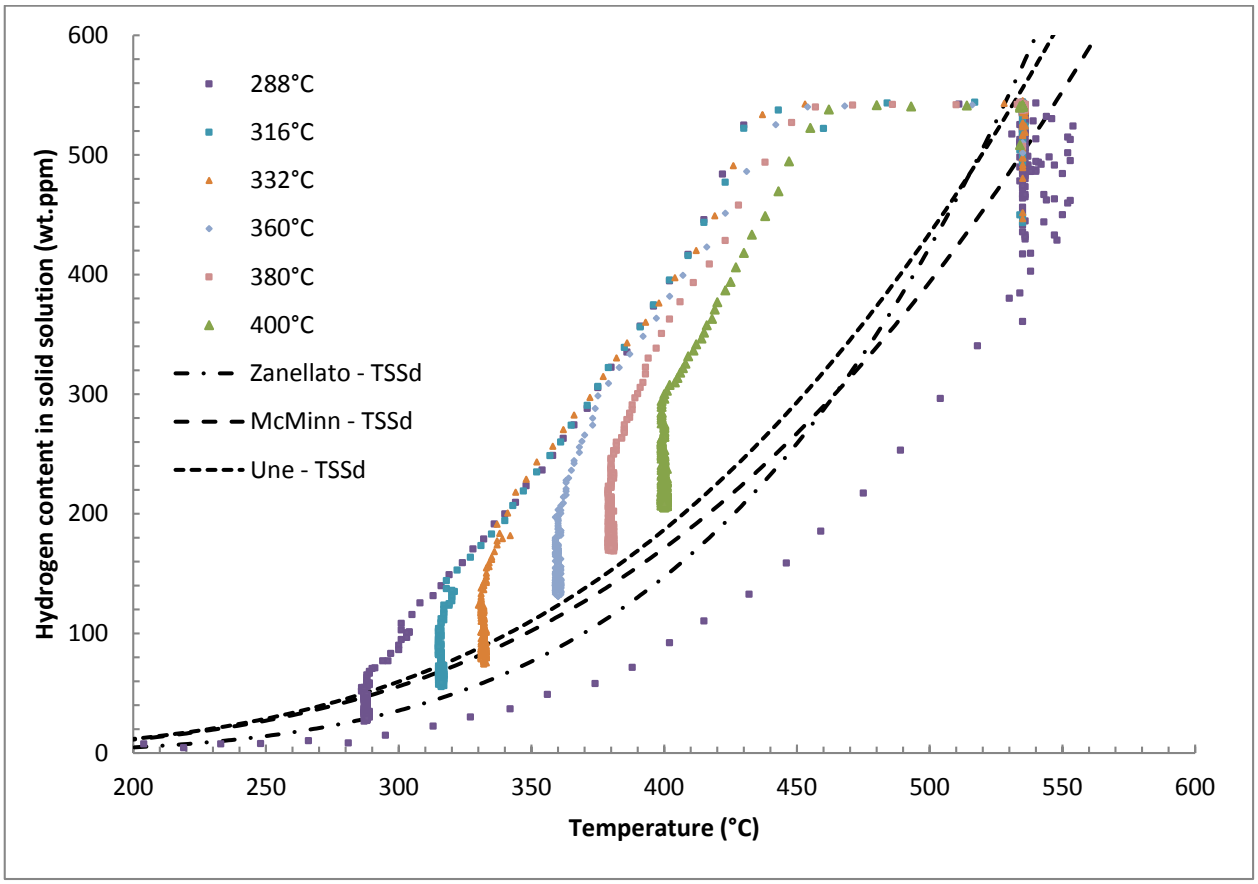


*Figure 3-57: Precipitation of hydrogen at different temperatures in a sample containing 541 wt.ppm of hydrogen. Evolution of the hydrogen content in solid solution as a function of temperature.*

It is clear from these plots that hydrogen in solid solution is also precipitating between the $TSS_P$ and the $TSS_D$ and that therefore, the $TSS_P$ is not the equilibrium value for precipitation, but rather a metastable equilibrium observed during precipitation. This curve is called a super saturation curve in different crystallization books [75] [76]. The approach used to model hydrogen precipitation in this study was chosen to follow the crystallization theory described in more detail in Mullin's and Myerson's books [75] [76].

### 3.3.6 New hydrogen precipitation understanding

The interpretation of the precipitation mechanisms given in the previous section implies changes in the model that was previously suggested by Courty and Stafford [72][74]. The changes will be following the precipitation theory given in the crystallization books referred to earlier [75][76]. Four different mechanisms will be discussed which are (1) the onset of the nucleation (2) nucleation and growth happening simultaneously (3) growth and (4) dissolution.

Dissolution has not been studied very much in literature. It is known to be a fast process and is therefore hard to measure. As a first approximation, the dissolution process was assumed to be instantaneous in this model.

Growth has been studied and a good model has been derived by Marino [38]. In his model Marino mentions that if there is no concentration or temperature gradient, $\frac{dC_P}{dt} = \alpha^2\left(C_{ss} - C_{eq}\right)$ where $C_P$ is

the hydrogen content present as hydrides, $C_{SS}$ is the hydrogen content present in solid solution, α is the precipitation kinetics parameter and $C_{eq}$ is the equilibrium concentration value. In previous models (Courty [72], Stafford[74]), the value for $C_{eq}$ was taken equal to $TSS_P$ (although Stafford did do a study with $TSS_D$ as equilibrium value[74]). In the model proposed here, $C_{eq}$ is taken to be $TSS_D$, in accordance with [75][76] .

The onset of nucleation is a delicate part to model. Even though many different models are proposed for nucleation in crystallization theories, a lot of them assume single crystals or homogeneous nucleation. In a Zircaloy material, this assumption would be wrong considering the amount of grain boundaries, dislocations or alloying elements, serving as nucleation sites. An empirical model is proposed and referred to as being the only justified model to explain the behavior of real systems. The model in [75][76] is described as being:

$$\frac{dC_P}{dt} = k_n \Delta C_{max}^n \quad (2)$$

where $\Delta C_{max}$ is the width of the metastable region at a given temperature, $k_n$ the nucleation kinetics parameter and n is the order of nucleation. The order of the nucleation is said to have no physical meaning in the way that it doesn't represent the number of atoms required to form a given phase. Nucleation is the only phenomenon occurring at the onset of precipitation (i.e. when $C_P=0$) but growth happens as soon as the first nuclei is produced. Therefore, growth precipitation kinetics was also added in the labile region.

# 4 Three-Dimensional Modelling of Hydride Distribution with Tiamat (MPACT/CTF/BISON)

## 4.1 Multi-physics coupling schemes and models

### 4.1.1 VERA

The CASL has a set of reactor analysis tools that they maintain and develop for the purpose of modeling LWRs. These tools fall under the Virtual Environment for Reactor Applications Core Simulator or VERA-CS [77]. The modeling of the hydrogen behavior in this study involved several multi-physics codes that were coupled together within VERA. Using them provided the advantage of the high fidelity modeling in the calculated results. The performed computations involved three codes. MPACT is a neutron transport code used within VERA. The code provides modeling capabilities for 3-D method of characteristics (MOC), 2-D/1-D time-dependent transport, and traditional 2-D lattice physics capabilities. The modernized version of COBRA-TF (COolant Boiling in Rod Array – Two Fluid) known as CTF is a multi-dimensional sub-channel thermal hydraulics code. It is being utilized in the CASL project for high-fidelity thermal-hydraulics calculations. BISON is the Idaho National Laboratory's multi-dimensional (2D and 3D), finite-element-based, fuel performance code. BISON can model temperature distributions, fission product swelling, densification, thermal and irradiation creep, mechanical properties, and fission gas production. Those codes were coupled by TIAMAT, a multi-physics coupling code that was developed within CASL project as part of the VERA. It was used to couple the three single physics codes described above to perform high fidelity coupled calculations.

### 4.1.2 The coupling scheme with TIAMAT

Tiamat couples together a thermal hydraulics sub-channel code, a neutronics code, and a fuel performance code [78]. This coupling was originally created to accurately model pellet-cladding interaction, but the high-fidelity of the code allows it to create the accurate temperature distributions required for hydrogen prediction.

MPACT is used to calculate the power inside the fuel rods and pass it to BISON for fuel performance calculations. BISON will return the fuel rod temperature to MPACT that will use it to update the cross sections inside the fuel. CTF will pass the coolant temperature and density to MPACT that will be used to update the cross sections inside the coolant. The code will pass the cladding outer surface temperature to BISON that will be used as a boundary condition for the fuel rods. And, in return, CTF will take the heat flux from BISON to calculate the flow conditions and heat transfer to update the coolant temperature. The coupling scheme used in TIAMAT is shown in Figure 4-1.

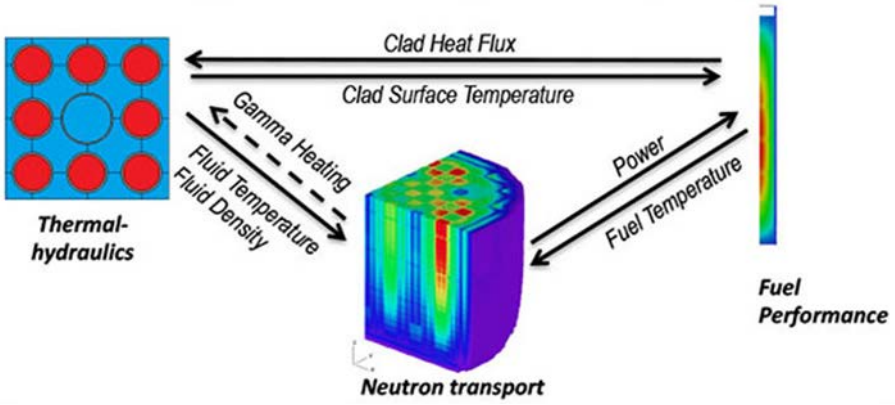


*Figure 4-1 Tiamat coupling scheme.*

## 4.2 Verification and validation of the coupled multi-physics code system, and testing the multi-physics coupling for the developed models

Two subassembly types were analyzed and reported here. One is a 3x3 subassembly with a guide tube in the center position. The other case is a 4x4 subassembly. Both cases include rods with different enrichments to induce azimuthal variation of temperature is a certain fuel rod of interest near the guide tube. Please note that 1% enrichment is used to represent a highly burnt fuel (fuel pin with high burnup) while 5% enrichment represent fresh fuel. A section of this rod is extracted and modeled in 3-D to investigate the azimuthal variation in the hydrogen distribution in the cladding.

### 4.2.1 The 3x3 sub-assembly VERA-Model

To investigate the azimuthal distribution of hydrogen, the outer cladding temperature should be azimuthally dependent. VERA is used to generate such a case in which a 3x3 sub-assembly is modeled. The sub-assembly contains eight fuel pins of different enrichments and a guide tube. The flow area is divided to 16 subchannels plotted in Figure 4-2.

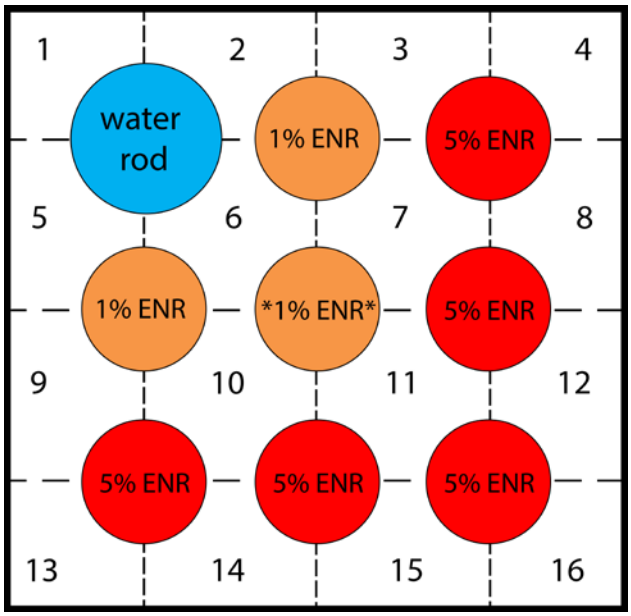


*Figure 4-2. VERA modeled 3x3 subassembly.*

The input parameters of VERA are scaled to the chosen subassembly. Such parameters are the array power, mass flow rate, spacer grids weight, etc. A summary of some of the important parameters used within the VERA model are summarized in Table 4-1.

*Table 4-1 Subassembly VERA input parameters.*

| Parameter | Value |
|---|---|
| System parameters: | |
| Reactor Type | PWR |
| Subassembly power (MW) | 0.535 |
| Average linear heat rate (kW/m) | 18.5 |
| Coolant pressure (MPa) | 15.5 |
| Mass flow rate (kg/s) | 3.2 |
| Inlet temperature (K) | 566 |
| Fuel pin parameters: | |
| Fuel type | $UO_2$ |
| Fuel density (g/cm$^3$) | 10.257 |
| Cladding type | Zircaloy-4 |
| Cladding density (g/cm$^3$) | 6.56 |
| Fill gas | Helium |
| Initial fill gas pressure (MPa) | 2.6 |
| Geometry: | |
| Fuel pellet radius (m) | 0.004096 |
| Cladding outer radius (m) | 0.00475 |
| Cladding thickness (m) | 0.00057 |
| Pin pitch (m) | 1.2 |
| Active fuel height (m) | 3.6 |
| Core height (m) | 4.06 |

The coupled computations were performed according to the scheme in Figure 4-1. The rod of interest in Figure 4-2 is R-5 in the center marked with two asterisks and has a 1% enrichment. It is surrounded by a group of rods having 5% and 1% enrichments and a guide tube. R-5 is divided to four quadrants. Each quadrant is part of one of the subchannels 6,7,10 and 11. The different rod types in those subchannels resulted in a different average coolant temperature in each of them. This leads to four different average outer cladding surface temperature for the same rod R-5 in each of the four quarters.

#### 4.2.1.1 Stand-alone 3D BISON model

It would be computationally impractical approach to try to model a full-length fuel rod in 3D using BISON. Therefore, a section of interest in the fuel rod around a spacer grid was extracted and modeled. The chosen spacer grid was the highest one covering the active length of the fuel at a height of 322 cm. The reason for this choice is to have a temperature gradient that is high enough to allow the investigation of the hydrogen diffusion and precipitation. Eleven discrete fuel pellets were modeled with the cladding outer surface temperatures as boundary conditions extracted from CTF. Table.4-2 summarizes the axial locations at which the temperature boundary conditions were computed by CTF and the corresponding temperature values.

*Table 4-2 CTF cladding temperature boundary conditions in each subchannel surrounding the*

*modeled rod section.*

| Axial height (m) | Ch. 6 | Ch.7 | Ch.10 | Ch.11 |
|---|---|---|---|---|
| 3.183 | 317.23 | 327.76 | 331.3 | 333.65 |
| 3.242 | 316.96 | 327.55 | 331.07 | 333.47 |
| 3.301 | 316.93 | 327.49 | 331.1 | 333.48 |

The average discrete temperatures provided by CTF had to be converted to a continuous domain on the cladding surface in order to be able to use them in the stand-alone 3D BISON model. To be able to do this, a parsed function was created and used to linearly interpolate the temperatures at the outer surface of the fuel between the specific CTF average temperatures as shown in Figure 4-3.

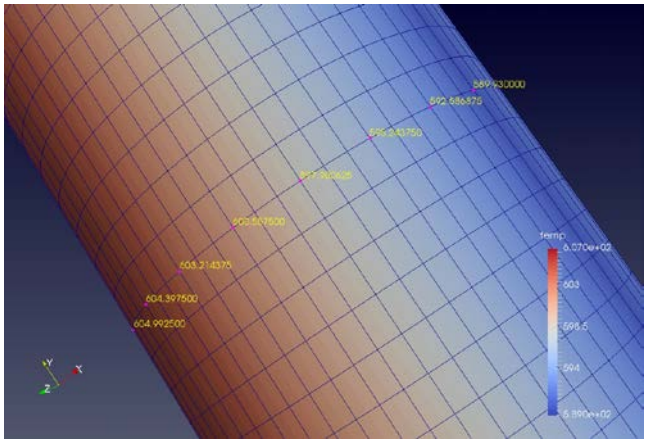


*Figure 4-3 Azimuthally asymmetric outer cladding temperature profile.*

The mesh on the extracted section of the fuel pin was created with CUBIT/TRELIS. A coarse mesh was used in the beginning to test the 3D model and modifications to it. The mesh was later refined to provide a higher resolution and more accurate representation of the hydride formation in the cladding. In order to investigate the formation of hydrides, the concentration of hydrogen has to increase beyond the TSSP limit at least at the lowest temperatures in the model domain. These temperatures are on the outer surface of the cladding. In this case study, the outer cladding surface temperature ranged from about 590 K to 606.7 K. We got a corresponding TSSP values of 123 to 149.5 wt.ppm respectively. Starting the simulations with zero wt.ppm concentration of hydrogen would not lead to the formation of hydrides in the cladding. The hydrogen pickup process would have taken a long time to allow this to happen. It is costly from a computation resources point of view to model this situation. An alternative approach was to assume a specific initial concentration of hydrogen in the cladding. This concentration should be high enough to allow the hydrogen precipitation process to take place. In this case, the initial hydrogen concentration was taken to be 150 ppm by weight.

#### 4.2.1.2 3x3 stand-alone 3D BISON results

The simulation time was taken to be $5x10^6$ seconds, which is around two months of irradiation, at a linear heat rate of 18.5 kW/m. In Figure 4-4 the hydrogen distribution is depicted at the end of the simulation. Hydrogen in the solid solution migrated to the lower temperature regions of the cladding where the concentration reached 132.5 wt.ppm. This value is lower than the initial concentration of 150 wt.ppm due to the formation of hydrides. The effect of the azimuthal variation of the temperature

is clearer when comparing Figure 4-3 and Figure 4-4. It can be seen the lower the temperature the higher the hydrogen concentration and vice versa.

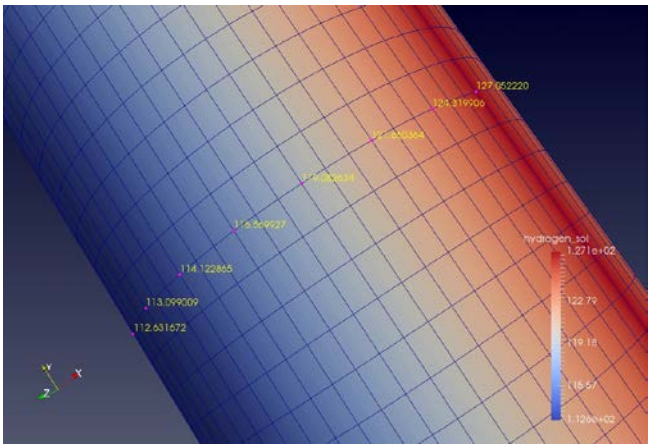


*Figure 4-4. 3D hydrogen distribution in the cladding.*

Axially, as shown in Table 4-2, the change of the temperature due to the space grid is lower than 1 K. This does not considerably affect the axial hydrogen distribution within the modeled section of the fuel pin. The regions in the cladding in contact with the inter-pellets gap in the fuel will be of relatively lower temperatures as shown in Figure 4-5. Those regions are favorable for the hydrogen to diffuse to then precipitate as hydride. Several rings of higher concentrations of hydrides are noticed on the outer surface of the cladding around those locations as shown in Figure 4-6. The concentration of hydrogen in the hydrides follows the same pattern of its concentration in the solid solution. In fact, the formation of hydrides is a consequence to the diffusion of hydrogen in the solid solution. That is because hydrogen concentration must first increase at certain locations above the TSSP value before it is possible for hydrides to be formed.

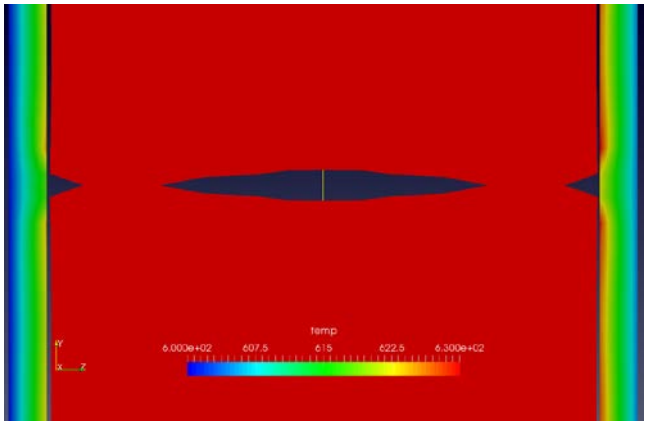


*Figure 4-5 Temperature profile in the cladding around a chamfered region of the fuel rod.*

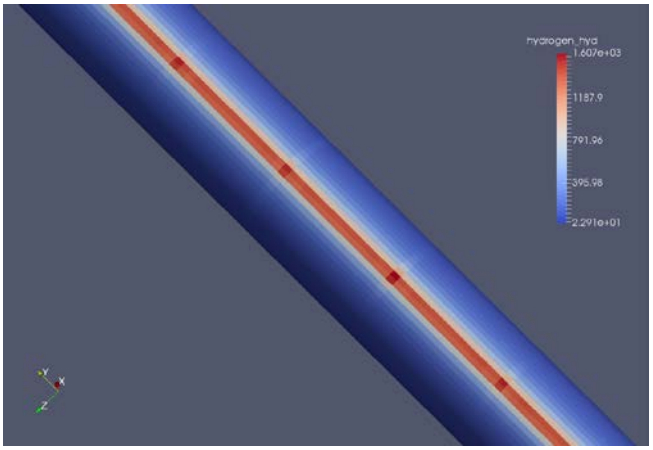


*Figure 4-6. 3D hydride distribution in the cladding.*

Figure 4-7 shows the hydrogen distribution in hydrides along an axial line on the outer surface of the cladding. The spikes in hydrides concentration corresponds to locations around the inter-pellets gaps. The lower hydride concentrations are in regions where the cladding is in contact with the right cylindrical section of the fuel pellets.

The azimuthal and radial distribution of the hydrogen in the solid solution and in the hydrides was investigated in a radial slice of the cladding. This slice was taken at an inter-pellets location where the distribution of hydrides reached a local axial maximum. Figure 4-8 depicts the temperature profile in this slice. The temperature is higher on the inner side of the cladding and decreases radially to reach the boundary condition temperatures. It varies azimuthally as well because of the imposed boundary conditions. This temperature variation will affect the hydrogen and hydrides distributions as shown in Figure 4-9 and Figure 4-10.

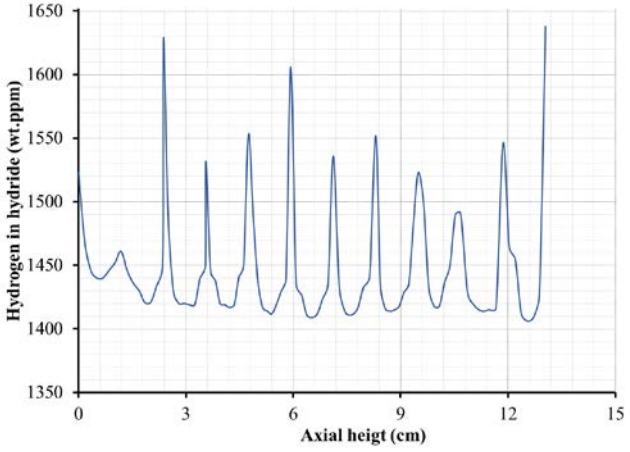


*Figure 4-7. Axial distribution of hydrogen in hydrides along the modeled section of the fuel pin.*

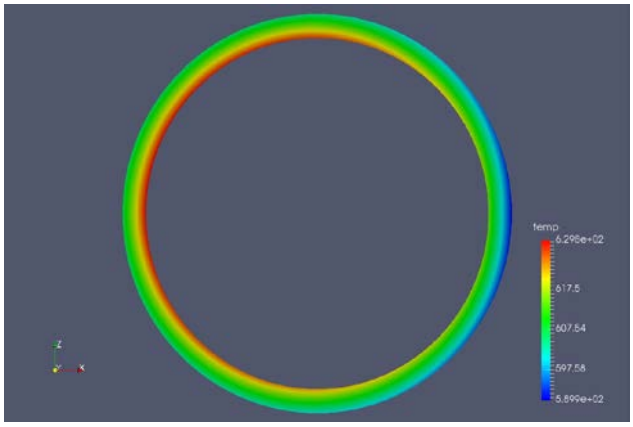


*Figure 4-8 Temperature profile in a horizontal slice in the modeled section of the fuel.*

In Figure 4-9 the hydrogen distribution in the slice is shown. Hydrogen migrates radially to the relatively cooler outer periphery of the cladding and azimuthally to the regions with lower temperature. As the hydrogen migrates to the lower temperature regions, the concentration in the warmer regions of the cladding falls below TSSD. Therefore, hydrogen cannot precipitate in those regions. Hydride precipitates was formed in regions with lower temperatures i.e. higher concentration of hydrogen and lower TSSP values as shown in Figure 4-10.

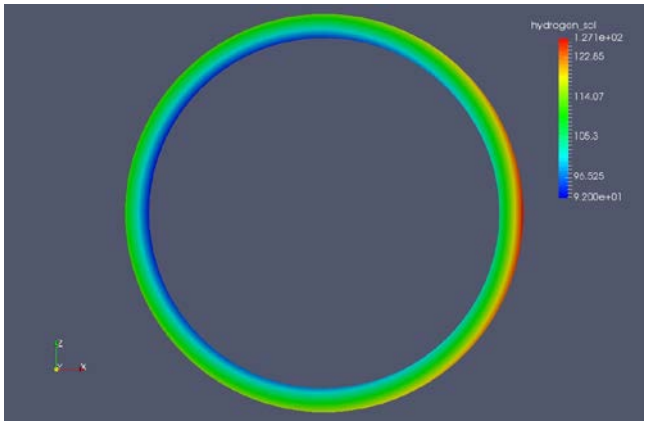


*Figure 4-9. Hydrogen distribution in solid solution at a slice of the cladding.*

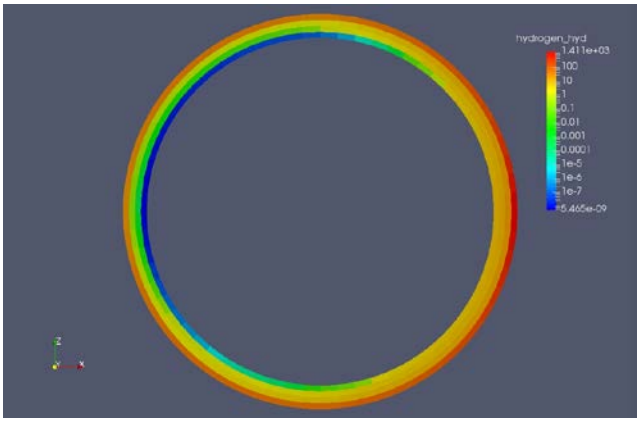


*Figure 4-10 Hydrogen distribution in hydride at a horizontal slice of the cladding.*

### 4.2.2 The 4x4 Sub-Assembly VERA Model

A full length 4x4 sub-assembly was first modeled using Tiamat, then parameters were taken from an area of interest near a spacer grid and used to create a single-pin, three-dimensional, BISON model of that area. The following section describes these modeling developments. Several cases were created to test the capability of the previously developed hydrogen distribution model to reproduce observed instances of hydrogen concentration in response to azimuthal temperature gradients. Two main cases were considered in which azimuthal temperature variations were established by an asymmetric distribution of fuel rod enrichment around the fuel rod of interest in a four-pin by four-pin sub-assembly. To test the hydrogen modeling capabilities of the BISON code, models were created that employed geometries and pin positioning that would induce large azimuthal temperature gradients. Sub-assemblies of 16 pins in a 4x4 pattern were used as shown in Figure 4-11.

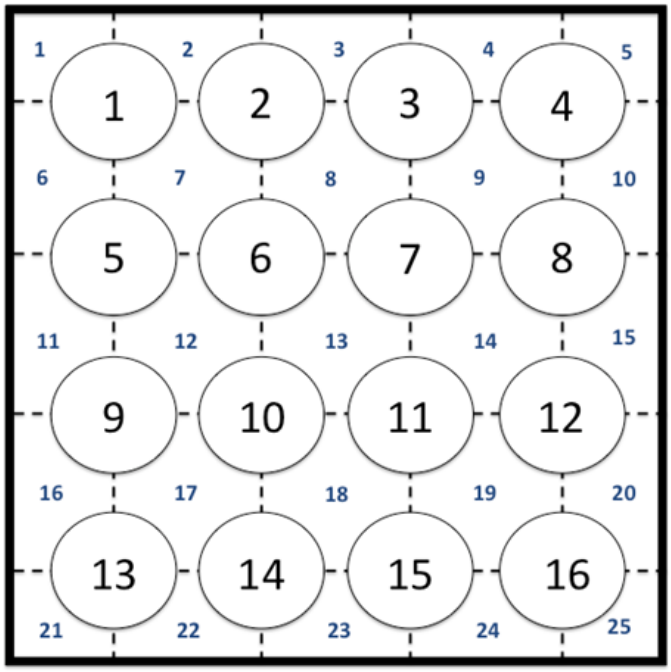


*Figure 4-11 Pin and Sub-Channel Numbering for the Coupled 4x4 Sub- Assembly Models [2].*

### 4.2.3 Tiamat Sub-Assembly Model description

Tiamat was first used to model a 16-pin sub-assembly, in order to achieve detailed power distributions (from MPACT) and sub-channel flow parameters (from CTF) with feedback between codes and from the fuel performance code BISON. The coupling simulated a full-length assembly including fuel, plenum, and spacer grids. The problem specifications can be seen in Table 4-3. The spacer grid position for the model can be seen in Figure 4-12 (plenum region not included in diagram). For the detailed hydrogen distribution, a single pin of interest was selected. The sub-assembly model employed geometries, and pin positioning that would induce large azimuthal temperature gradients to test the hydrogen modeling capabilities of the BISON code. The sub-assembly was modeled at a full 3.65 meter active fuel length height with upper and lower plenum also modeled. The planar pin orientation and enrichment can be seen in Figure 4-13.

*Table 4-3 Tiamat 4x4 Sub-Assembly Input Parameters Parameter*

| | **Value** | **Units** |
|---|---|---|
| **System Parameters** | | |
| Reactor Type | PWR | |
| Layout | 4 x 4 | |
| Array Power | 1.004 | MW |
| Average Linear Heat Rate | 18.225 | kW/m |
| Core Pressure | 15.5 | MPa |
| Mass Flow Rate | 4.88 | Kg/s |
| Beginning of Cycle boron loading | 1300 | ppm |
| Inlet Temperature | 565.9 | °K |
| Coolant | H2O | |
| **Fuel Rod Parameters** | | |
| Fuel | $UO_2$ | |
| Enrichment | | |
| High | 4.95 | % |
| Low | 1.00 | % |
| Fuel Density | 10.4 | g/cm3 |
| Percent Theoretical Density | 95 | |
| Burnable Poison | None | |
| Cladding | Zircaloy-4 | |
| Cladding Density | 6.55 | g/cm3 |
| Fill Gas | Helium | |
| Initial Fill Gas pressure | 2.62E6 | Pa |
| **Geometry** | | |
| Fuel Pellet radius | 4.096E-3 | m |
| Cladding Inner Radius | 4.18E-3 | m |
| Cladding Outer Radius | 4.75E-3 | m |
| Cladding Thickness | 5.70E-4 | m |
| Pin Pitch | 1.26E-2 | m |
| Active Fuel Height | 3.6576 | m |
| Core Height | 4.06 | m |
| Lower Plenum Height | 0.355 | m |

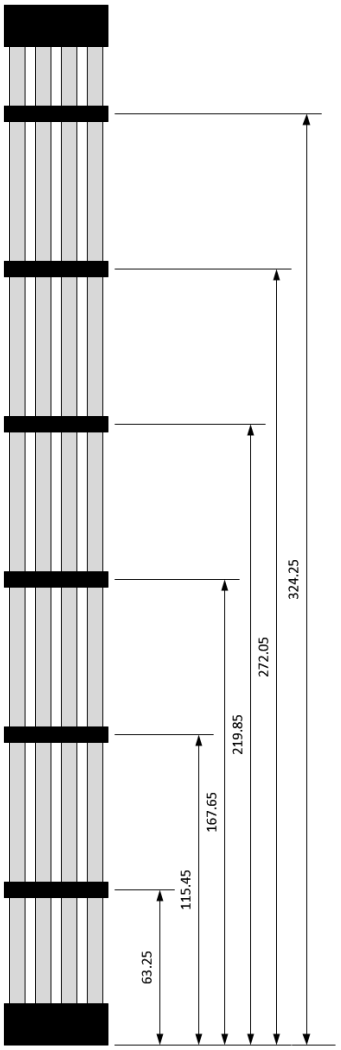


*Figure 4-12 Spacer Grid Positioning for Coupled 4x4 Tiamat Simulation-Dimensions in Centimeters –Figure Not to Scale*

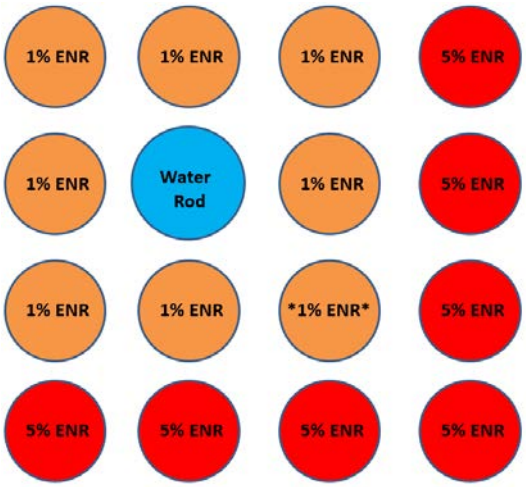


*Figure 4-13 Tiamat 4x4 Sub-Assembly X-Y Planar Layout*

### 4.2.4 Three-dimensional BISON model

Although the neutronics and thermal hydraulics portion of Tiamat are able to model the assemblies in three-dimensions, the coupling employs only a 2D RZ mesh and model for the execution of the BISON fuel performance code. This is done in order to acquire the benefits of the fuel performance feedback without greatly increasing the computational cost. For investigation of 3D effects in fuel cladding, the BISON case was expanded to three-dimensions in a separate model outside Tiamat. This was accomplished by obtaining information on the fission gas release, power history, and outer cladding temperature from the coupled calculation. This information was taken from a node directly above the spacer grid at an axial position of 2.199 meters relative to the bottom of the fuel stack. The information was saved as parameters vs. time in exterior files and was then applied to a 3D BISON model as functions and boundary conditions. The investigation was only concerned with a small portion of fuel rod above a spacer grid. For this reason, and to cut down on computational expense, only a portion of the rod of interest (rod position starred in Figure 4-13) was modeled. The axial portion used was a short length of the rod immediately downstream from a spacer grid. A single pin containing 5 fuel pellets used to model this portion with BISON as shown in Figure 4-14. This 3D model is oriented in a negative Z Cartesian coordinate system (as seen in Figure 4-14 ) with the fuel rod axis aligned with the Y-axis. The bottom center of the pin is located at the origin. The outer cladding temperatures were taken from the Tiamat output and applied to the 3D BISON model using a parsed function that estimated a linear temperature increase across the largest azimuthal gradient in the fuel. This gradient was quadrant 1 to quadrant 4 and was applied across the x-axis in the 3D BISON model.

A second model was created that simulated the cladding within the spacer grid. This included a portion upstream of the spacer grid, the full spacer grid, and a portion downstream of the spacer grid. The boundary conditions for this model were taken from the fuel pin of interest at a height of 2.721 meters. The same 2D to 3D BISON modeling process was used and was run using a three-dimensional outer cladding temperature boundary condition. This temperature distribution was calculated by the CTF portion of Tiamat where there is a clad surface temperature calculated at each node and each channel. At the spacer grid, there is a slight temperature drop associated with the pressure drop at that location. This required the temperature boundary condition to vary axially as well.

The 3D temperature distribution was applied to the BISON model by using a composite function, which multiplies two functions together. The temperature distribution caused by the azimuthal variation was symmetric and could be modeled by a parsed function, as previously performed. This was a linear function that varied with x position and modeled the temperature rise across the largest azimuthal gradient; quadrant 1 to quadrant 4. The axial variation was accounted for by using a piecewise bilinear function. This function contained a multiplier that varied with axial position and time. The composite function applied the bilinear multiplier to the parsed function output at every position along the outer cladding in order to create the outer cladding temperature boundary condition.

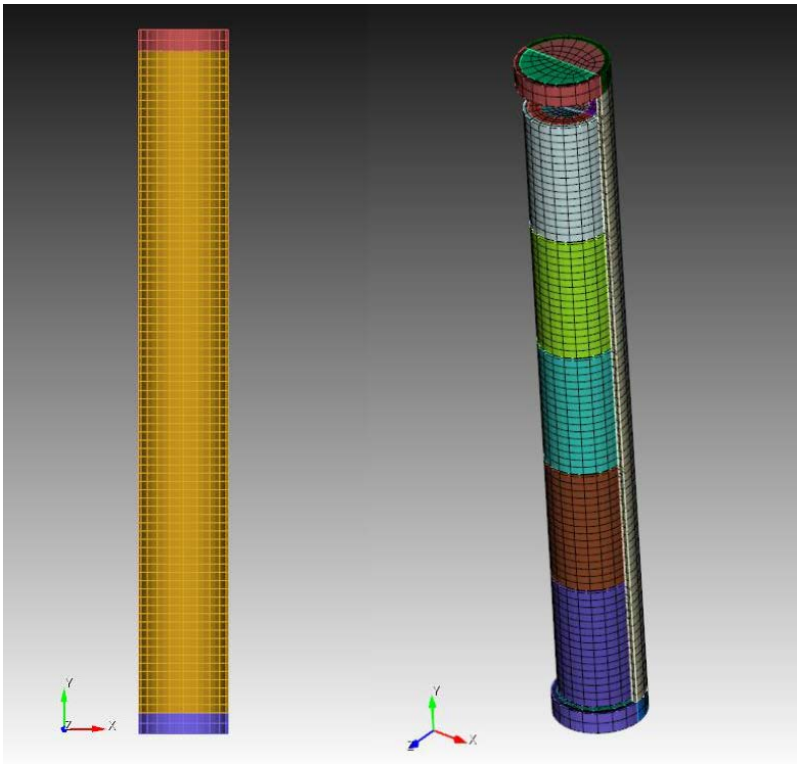

*Figure 4-14 3D Five Pellet BISON Model Left: Front View Right: Isometric View with Cladding Cut Away.*

### 4.2.5 BISON 3D Hydrogen Distribution with Tiamat Boundary Conditions

#### *4.2.5.1 Node above Spacer Grid*

This section discusses the results obtained in the 2D-to-3D modeling scheme [79]. Figure 4-15 shows the 3D distribution of hydride precipitate in the five-pellets fuel rod for the model of the pin area just above the spacer grid. Slight azimuthal variation can be seen as well as axial variation with defined rings of higher concentration at pellet interfaces where there is a lower temperature. Note that the ends of the model in Figure 4-15 provide erroneous hydride distribution. The end caps in the cladding are necessary for the model, but are not realistic and are unheated. The middle region displays accurate hydride distribution.

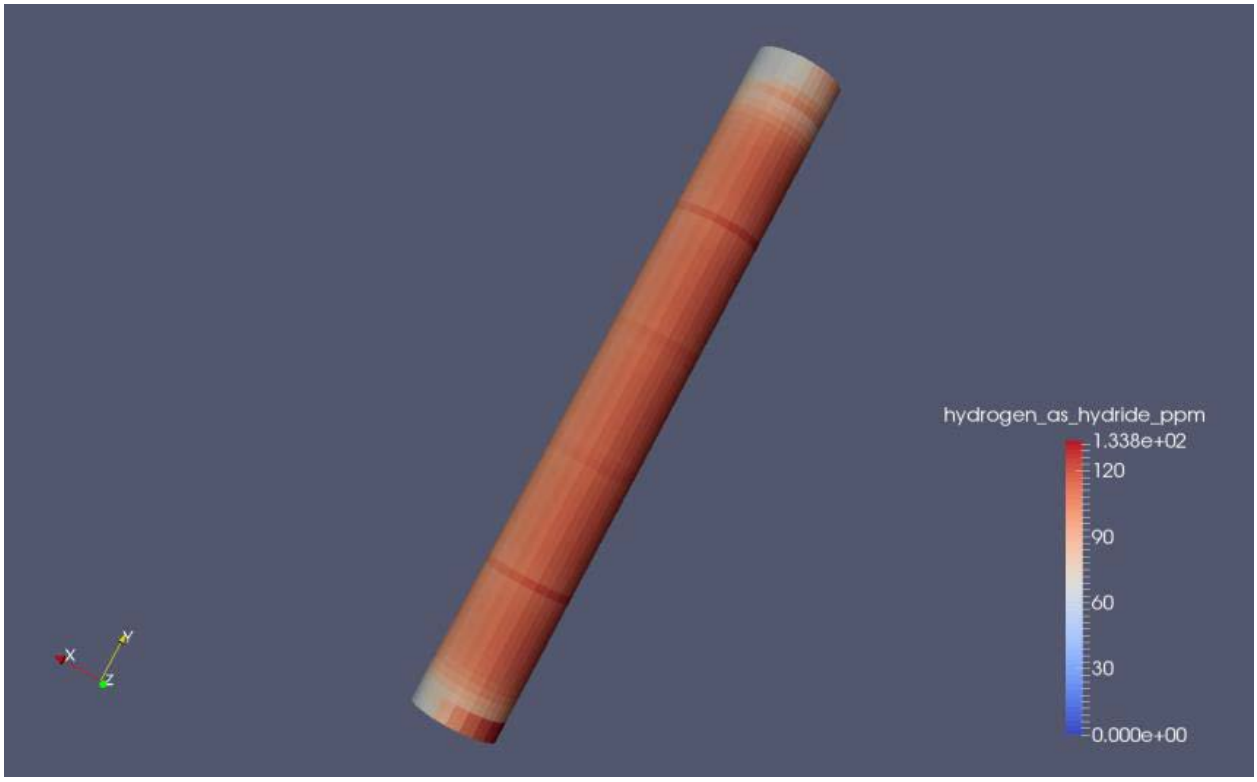


*Figure 4-15 3D Distribution of Hydride Precipitate on Outer Cladding Surface.*

*Table 4-4* shows the Tiamat temperature output at each cladding surface quadrant at nodes downstream of, at the location of, and upstream of the spacer grid located at 2.83 meters (this height includes the plenum height). Figure 4-16 shows the hydrogen and hydride distributions when this 3D outer cladding temperature model is applied. These mesh models were improved over the previous 3D case by applying the hydrogen model to only the cladding directly adjacent to the radial surfaces of the fuel pellets. The cladding 'caps' necessary for the pressure calculations in the BISON models acted as hydrogen sinks as they were at much lower temperatures than the cladding directly adjacent to the radial surface of the fuel. Slight variation in hydrogen distribution can be seen, however, due to higher temperatures on the inside of the cladding, the smaller temperature variation on the outside of the cladding is less noticeable. The hydride precipitation shows larger variation axially and azimuthally. This is due to the short simulation time of the problem. An initial hydrogen concentration of 200 ppm was set and the simulation was run for 1.6 x $10^5$ seconds. In this time, the hydrogen precipitates as would be expected at that concentration and temperature. The precipitation follows the set outer cladding temperature distribution and pattern of the fuel pellet interfaces.

*Table 4-4 Temperature Distribution around Spacer Grid*

| *Axial Position [m]* | | **Quadrant 1** | **Quadrant 2** | **Quadrant 3** | **Quadrant 4** |
|---|---|---|---|---|---|
| **Node Bottom** | **Node Top** | **[K]** | **[K]** | **[K]** | **[K]** |
| 285.91 | 293.97 | 603.6 | 606.79 | 606.79 | 608.71 |
| 282.1 SG | 285.91 SG | 602.71 | 605.84 | 605.84 | 607.74 |
| 274.03 | 282.1 | 603.01 | 606.27 | 606.27 | 608.2 |

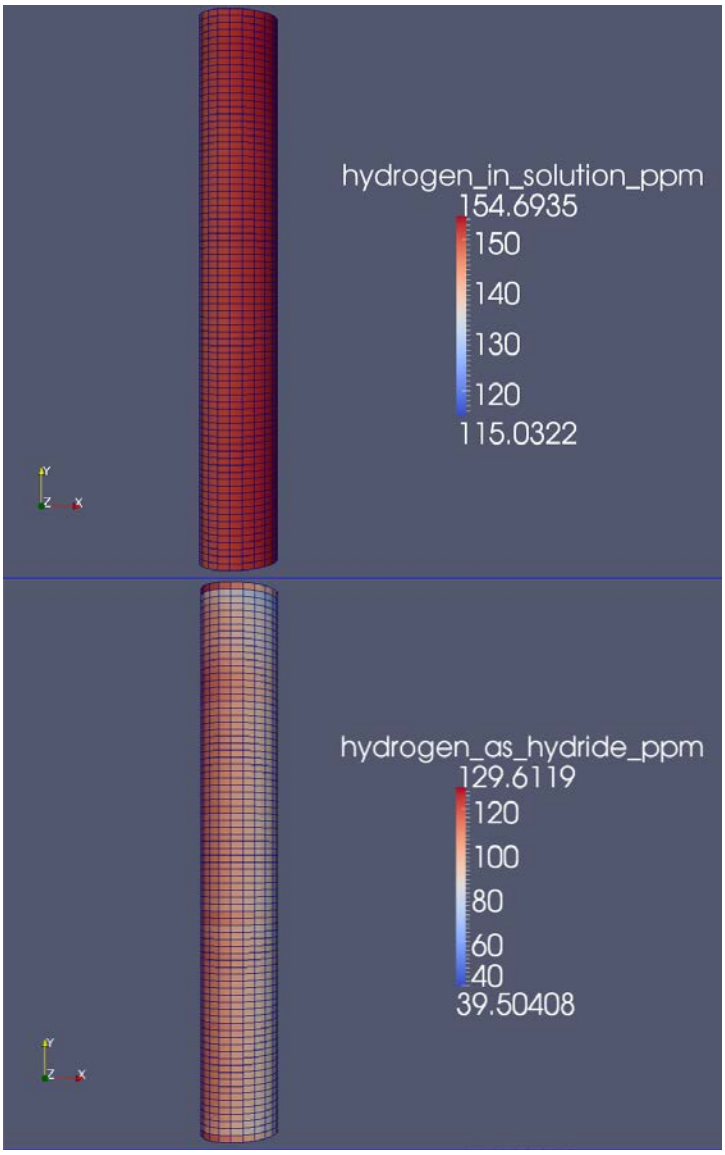


*Figure 4-16 Top: Hydrogen Distribution for 3D Spacer Grid Modeling Bottom: Hydride Distribution for 3D Grid Modeling.*

# 5 Refined modeling with MPACT/STAR-CCM+/BISON

## 5.1 Fuel assembly geometry

A 5x5 region of a 17x17 PWR fuel assembly was selected as test problem. Eight grid spacers with mixing vanes are present on the fuel assembly. A three-dimensional (3D) perspective of the spacer design is presented in Figure 5-1. The geometry and dimensions of the spacer design and mixing vanes are reported in Figure 5-2 and Figure 5-3. The dimensions of fuel pins and guide tubes are given in Table 5-1. Of all spacers present in the fuel assembly, only the top three including mixing vanes have been modeled with STAR-CCM+ in order to limit the required computation time. The axial locations of the grid spacers modeled in the present simulations are shown in Figure 5-4. The axial region selected for the explicit CFD modeling of the grid spacers exhibits the highest pin powers and cladding temperatures.

The numbering convention adopted to identify individual fuel rods is shown in Figure 4 (right). With respect to the coordinate system centered in rod #01, illustrated in Figure 4, the azimuthal angle theta is defined as equal to $0^o$ for (x =r; y = 0) where r is the radius of the rod, as $90^o$ for (x =0; y = r), $180^o$ for (x = -r; y = 0), and $270^o$ for (x = 0; y = -r).

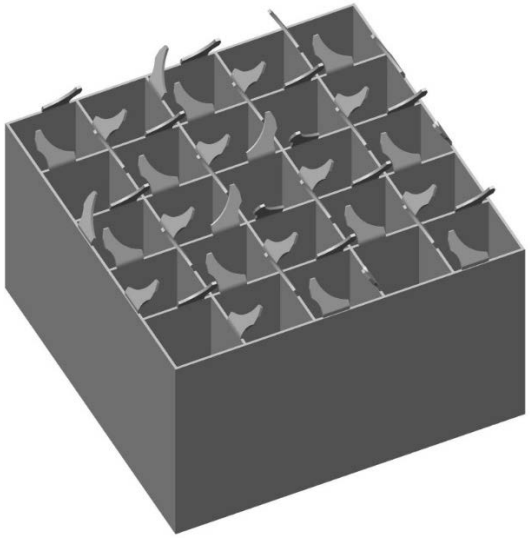

*Figure 5-1 CAD for 5x5 grid spacer with mixing vanes.*

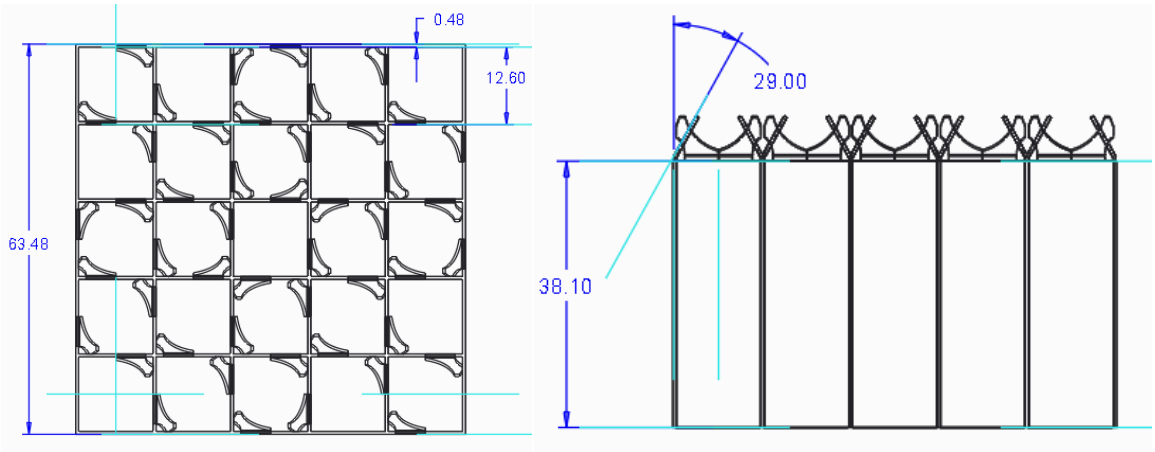


*Figure 5-2 Spacers geometry and dimensions in mm.*

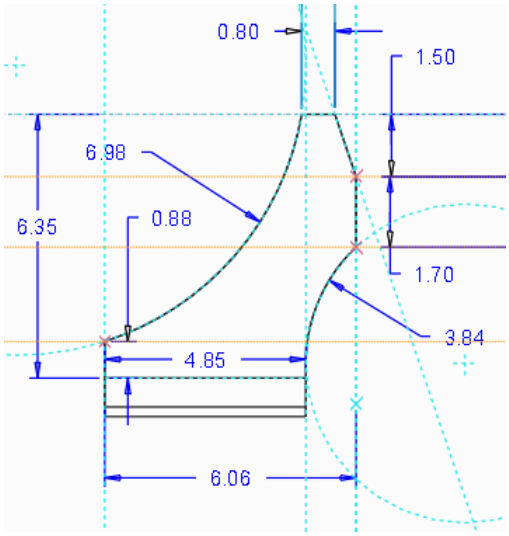


*Figure 5-3 Geometry of mixing vanes with dimensions in mm.*

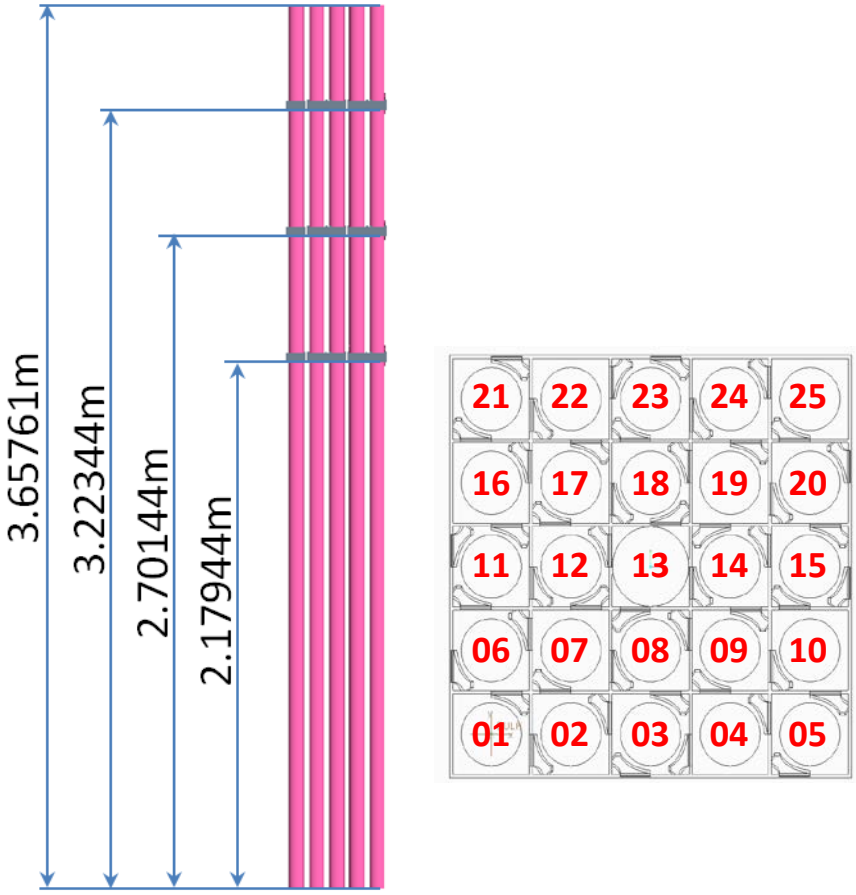


*Figure 5-4 Axial location of grid spacers (left) and adopted rod numbering (right).*

*Table 5-1 Dimensions of fuel pins and guide tubes.*

| Parameter | Value (cm) |
|---|---|
| Pin pitch | 1.26 |
| Fuel rod outer radius | 0.4096 |
| Fuel pellet outer radius | 0.4666 |
| Guide tube outer radius | 0.602 |
| Guide tube inner radius | 0.561 |
| Active fuel height | 365.76 |

## 5.2 STAR-CCM+ model

The STAR-CCM+ computational mesh consists of over 64 M polyhedral cells. A mesh base size of 0.4 mm was adopted with 4 prism layers in the proximity of the wall. The fuel solid region is modeled as well to solve for the heat conduction within the fuel. The distribution of mesh elements among coolant, fuel, cladding, and guide tubes is summarized in Table 5-2. A cross section of the mesh with zoom on a single pin is reported in Figure 5-5, while a detail of the mesh of the mixing vanes is reported in Figure 5-6.

An inlet velocity of 5.239 m/s and pressure boundary condition is imposed for the inlet and outlet axial planes of the coolant domain, respectively. Symmetric boundary conditions are imposed on the lateral surfaces of the water domain. No-slip conditions are imposed on the grid spacers, pin walls and on the outer cladding surface. A volumetric power source is used in the fuel domain. The fluid-dynamic simulation includes conjugate heat transfer for the calculation of the temperature distribution in the fuel and cladding domains. The convergence criteria were fixed at $10^{-6}$ for continuity, momentum, and energy.

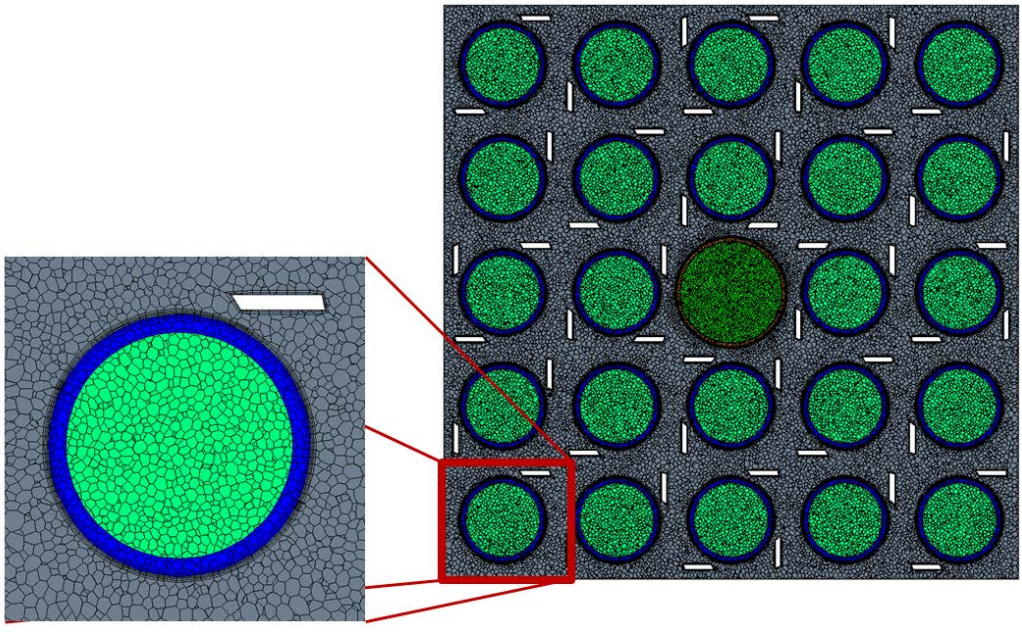

*Figure 5-5 Cross-section of the CFD computational mesh.*

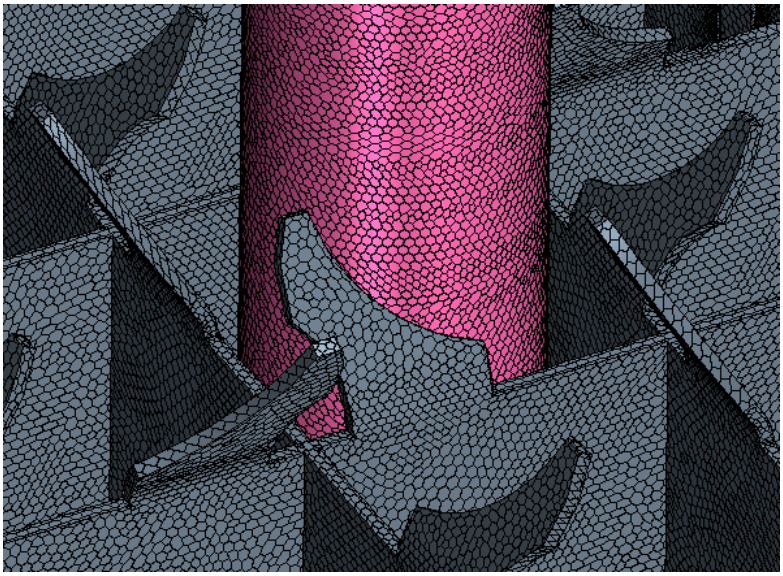

*Figure 5-6 Detail of CFD computational mesh of mixing vanes.*

*Table 5-2 Summary of CFD mesh*

| | Fluid | Cladding | Fuel | GT |
|---|---|---|---|---|
| **Cells** | 33,402,671 | 13,573,982 | 14,041,949 | 3,081,230 |
| **Faces** | 161,728,592 | 60,538,875 | 85,524,637 | 20,731,043 |
| **Vertices** | 112,379,469 | 45,224,451 | 70,251,624 | 17,608,914 |

The thermo-physical properties of fuel and cladding materials are summarized in Table 5-3. All properties are assumed to be constant, with the exception of the UO2 thermal conductivity which is assumed to be a function of the fuel local temperature. The adopted formulation is presented in Table 5-4, as are the coolant properties.

*Table 5-3 Thermo-physical properties of materials.*

| Material | Property | Value |
|---|---|---|
| **Fuel** | Density [kg/m$^3$] | 10400.0 |
| | Specific Heat [J/kg-K] | 300.0 |
| **Fuel Rod Cladding** | Density [kg/m$^3$] | 6500.0 |
| | Specific Heat [J/kg-K] | 350.0 |
| | Thermal Conductivity [W/m-K] | 17.0 |

*Table 5-4 Fluid properties and $UO_2$ thermal conductivity.*

| | |
|---|---|
| $\rho(T) = -1670.325859 - 4.84697 * T + 0.01225 * T^2 - 1.16905 * 10^{-5} * T^3$, $\rho_{sat} = 594.17 \frac{kg}{m^3}$ | (1) |
| $\mu(T) = 3.111 + 0.03026 * T - 0.8131 * 10^{-4} * T^2 + 0.4635 * 10^{-7} * T^3 + 1.677 * 10^{-9} * T^4 - 0.3094 * 10^{-12} * T^5 + 0.151 * 10^{-15} * T^6$, $\mu_{sat} = 7.287 * 10^{-5} \frac{Pa}{s}$ | (2) |
| $c_p(T) = \frac{T - 59160}{-167.5 + 4.091 * 10^{-4} * T^2} + 3659$, $c_{p\,sat} = 8513 \frac{J}{kg * K}$ | (3) |

| | |
|---|---|
| $k(T) = \frac{0.1183*10^{12} + 0.2419*10^{9}*T}{1 - 0.4177*10^{13}*T + 0.138*10^{11}*T^{2}}$, $k_{sat} = 0.45833\frac{W}{m*K}$ | (4) |
| $k_{UO2}(T) = 100 * \left(\frac{1}{11.8 + 0.0238 * T} + 8.775 * 10^{-13} * T^{3}\right)$ | (5) |

## 5.3 STAR-CCM+ model – mesh sensitivity study

The criteria and parameters used to generate the mesh for the 5x5 model were based on previous sensitivities studies carried out on a 4x4 model of similar geometry. The 4x4 sensitivity studies were performed using six different polyhedral meshes of increasing refinement in which either the number of prism layers in the wall proximity or the base size of the computational mesh was varied (see Table 5-5 for more details on the mesh parameters). A seventh mesh (v7 in Table 5-5) was included in the study as well, characterized by the same parameters as the polyhedral finest mesh (v6), but employing trimmed elements instead of polyhedral. The different meshes were compared by analyzing the magnitude of the velocity field computed on a cross-section right above the mixing vanes of one of the grid spacers. The results are reported in Figure 5-7. The location of the cross-section is shown on the top left corner of the figure. It can be observed that with a relative coarse mesh, characterized by a base mesh size of 0.4 mm (mesh v4), the velocity field can be reproduced with acceptable accuracy. Comparing mesh v6 with v7, it can also be concluded that with a given mesh base size and number of prism layers, trimmed meshes give results which are identical to the ones obtained with polyhedral meshes but require a slightly lower number of computational cells to cover the same domain.

*Table 5-5 CFD mesh sensitivity study for rod bundle with grid spacer and vanes.*

| Case | Cells number* [M cell] | Base size, m | Number of prism layers | Mesh type |
|---|---|---|---|---|
| **v1** | 1.9 | 6.0E-4 | 4 | polyhedral |
| **v2** | 2.5 | 5.0E-4 | 4 | polyhedral |
| **v3** | 5.0 | 3.5E-4 | 2 | polyhedral |
| **v4** | 5.6 | 4.0E-4 | 4 | polyhedral |
| **v5** | 6.7 | 3.5E-4 | 4 | polyhedral |
| **v6** | 25.4. | 2.0E-4 | 4 | polyhedral |
| **v7** | 23.4 | 2.0E-4 | 4 | Trimmed |

(* - Cells number is given for fluid domain for single spacer)

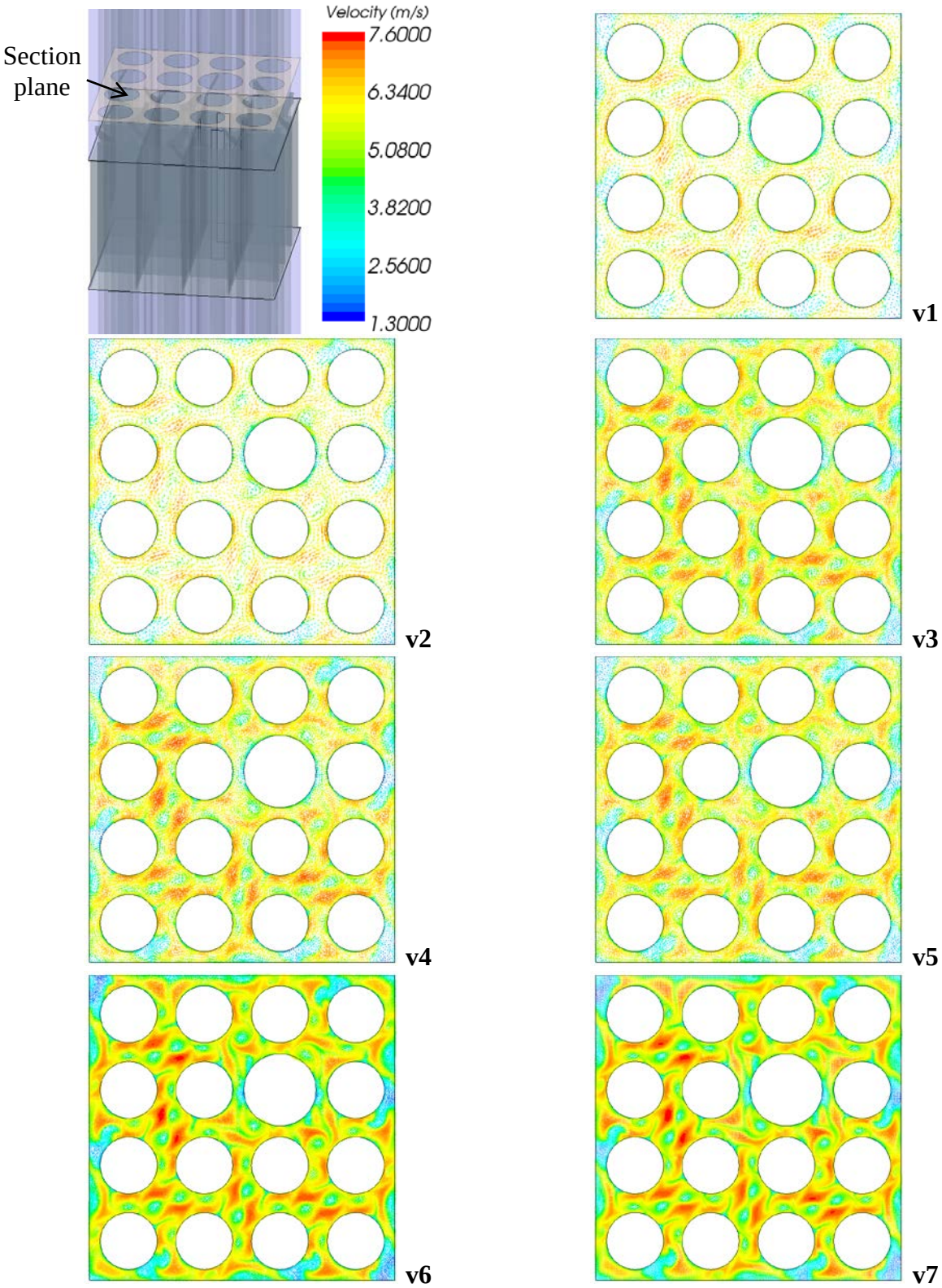


*Figure 5-7 Magnitude of the velocity field above a grid spacer.*

## 5.4 STAR-CCM+ model – results

A typical cladding temperature computed by STAR-CCM+ is reported in Figure 5-8. The rows of pins are numbered following the convention depicted in Figure 5-4, so in Figure 5-8 pin #1 is the first on the left, and pin #25 is the last on the right. The middle pin in row #3 is occupied by the water rod, and therefore it is not shown. The effect on the cladding temperature distribution due to the flow swirl induced by the mixing vanes is clearly visible.

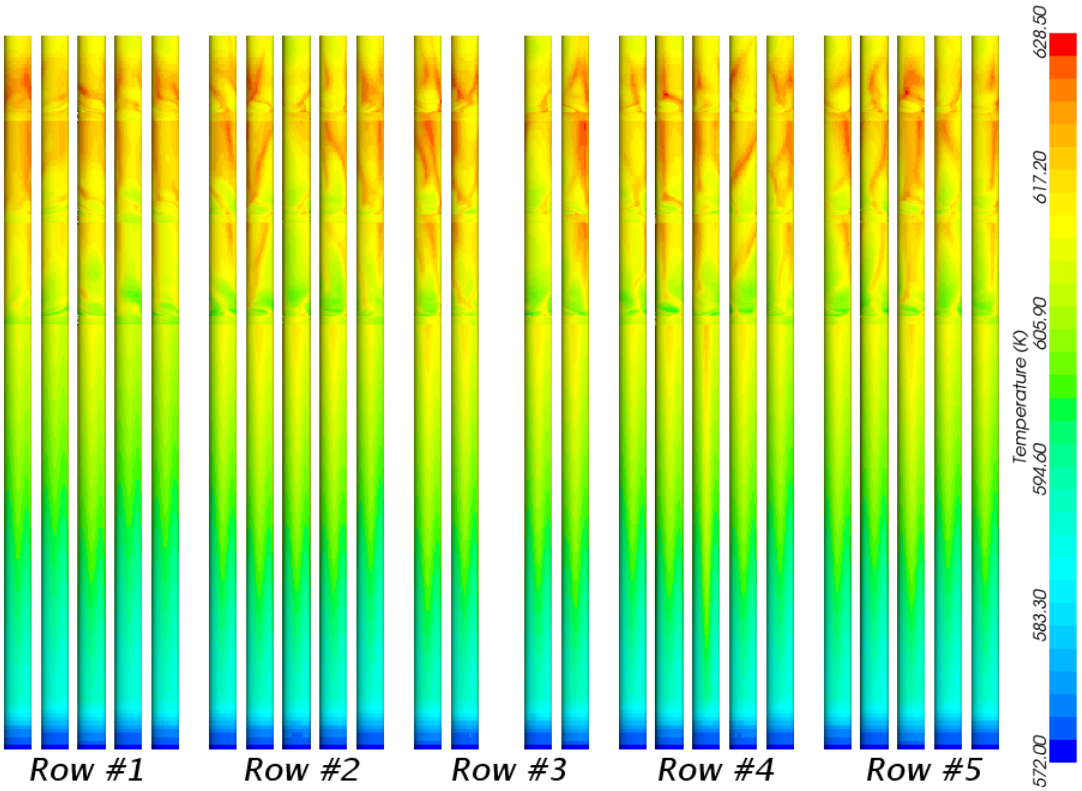


*Figure 5-8 Cladding temperature distribution.*

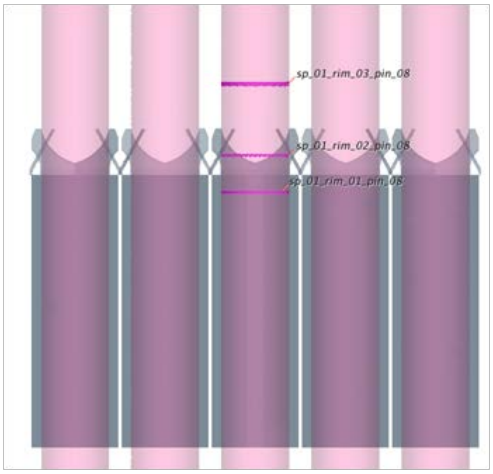


*Figure 5-9 Axial location along grid spacer for azimuthal distributions of Figure 5-10.*

The azimuthal temperature distributions for pin #8 at three different elevations in the proximity of spacer #1 of the modeled spacers (see Figure 5-4 for exact axial location) are reported in Figure 5-10. The locations of the three elevations are illustrated in Figure 5-9, with rim 1 being upstream and rim 3 downstream of the mixing vanes. Upstream of the mixing vanes, the azimuthal variations of the

cladding temperature are due by the different amount of coolant that is surrounding the pin surface in view of the subchannel geometry. Downstream of the mixing vanes, the temperature azimuthal variations are amplified by the flow swirl that the vanes induce. The flow swirl causes also a phase shift in the azimuthal temperature distribution.

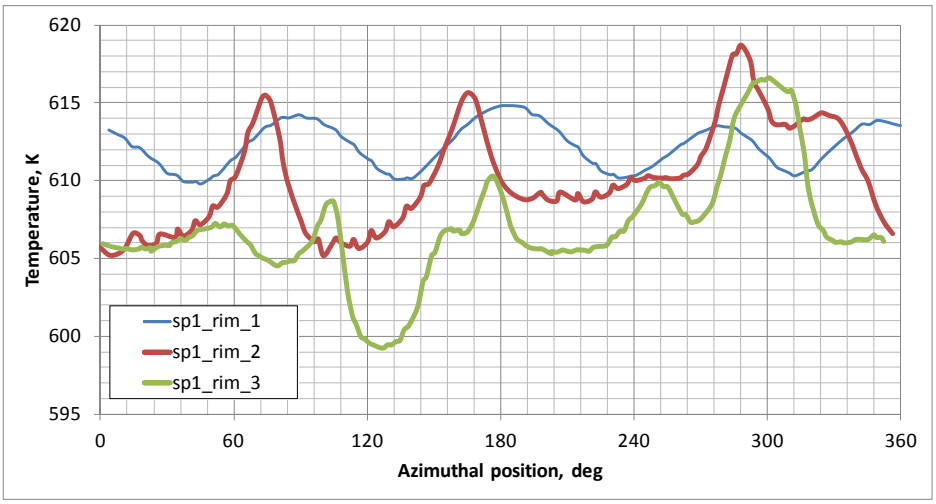


*Figure 5-10 Azimuthal distribution of cladding temperature for pin #8, spacer 1*

# 6 Validation of multi-physics models by prediction of hydrogen distribution in cladding and comparison with experiment

## 6.1 Model benchmarking

The hydrogen precipitation model was made and implemented into BISON and was tested by simulating the life of two pins that were very well characterized in 1993 by J.H. Zhang [20]. His study showed the hydrogen distribution in 16 zones in each reactor fuel rods, described by Figure 6-1. In the following part we will refer to areas 1, 5, 9 and 13 as layer 1; areas 2, 6, 10 and 14 as layer 2; areas 3, 7, 11 and 15 as layer 3 and the others as layer 4.

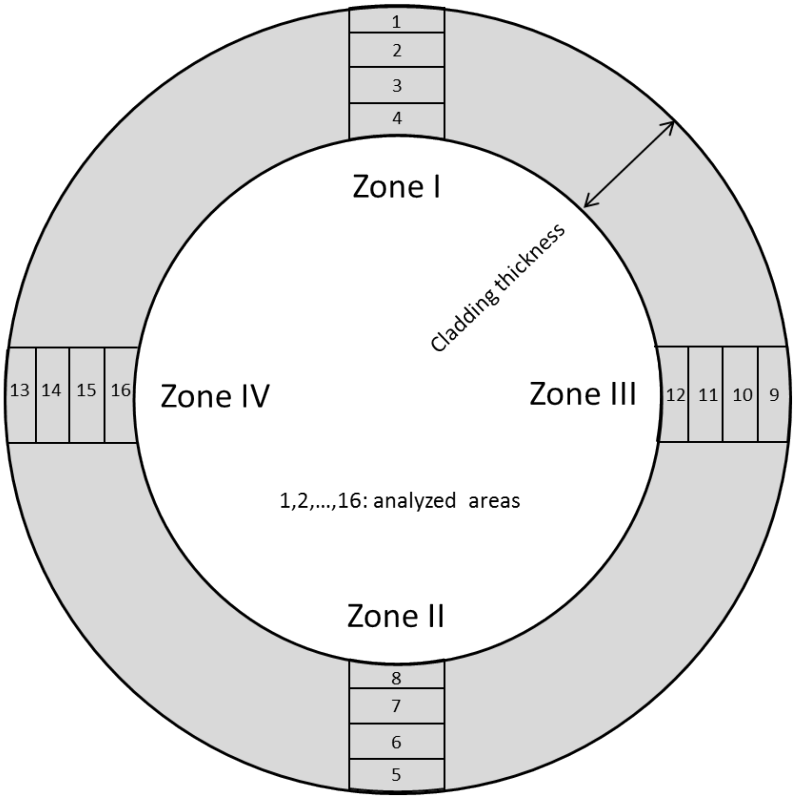


*Figure 6-1 Analyzed areas in Zhang's thesis [20].*

### 6.1.1 Gravelines

The Gravelines' fuel pin is characterized by the parameters given in Table 6-1 and by the power profile given in Figure 6-2. Given this data plus the hydrogen content that was measured by vacuum hot extraction and by image analysis in hot cells by J.H. Zhang [20], it is possible to simulate the hydrogen distribution in this portion of cladding with BISON and compare it to the experimental data reported in Table 6-2.

*Table 6-1 Gravelines' fuel pin and reactor characteristics.*

| | | | |
|---|---|---|---|
| **Clad Material** | Zircaloy-4 | **Number of cycles** | 5 |
| **Fuel** | $UO_2$ | **Enrichment (%5U)** | 4.5 |
| **Z position (mm)** | 3250 | **Burnup (MWd/tU)** | 58230 |
| **Outside diameter (mm)** | 9.49 | **Inside diameter (mm)** | 8.36 |
| **Pressure (bars)** | 155 | **Mass Flux (g cm-2s-1)** | 314 |
| **Inlet Enthalpy (J $g^{-1}$)** | 1264 | **Inlet Temperature (°C)** | 286 |
| **Outlet Temperature (°C)** | 323 | | |

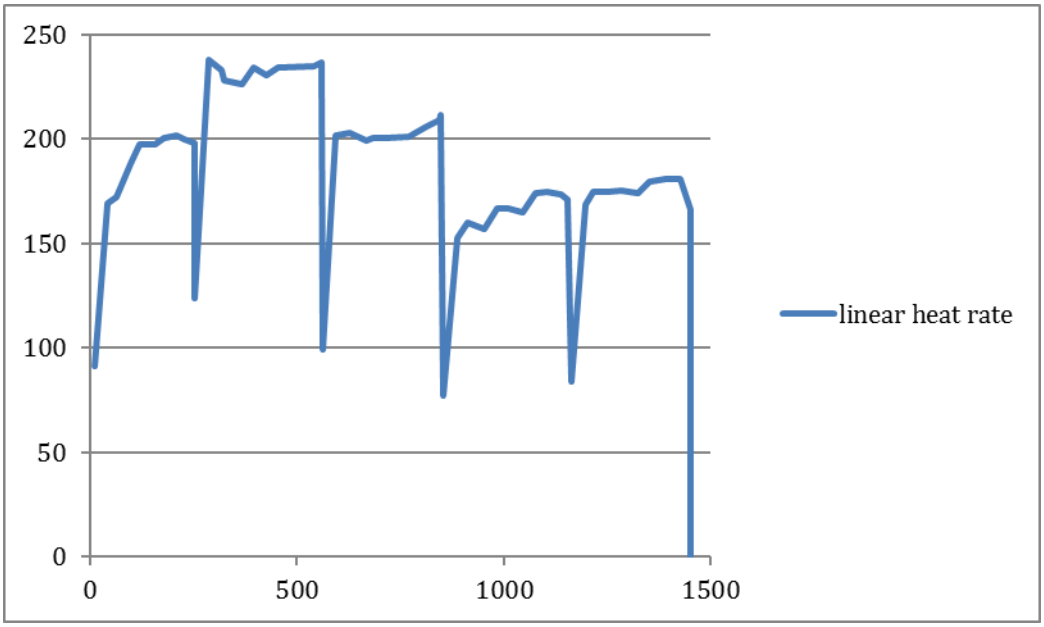


*Figure 6-2: Gravelines' power history.*

*Table 6-2 Hydrogen experimental distribution determined by Image Analysis, quantities are given in wt.ppm.*

| Radial position (µm) | Top | Bottom | Right | Left | Average [H] per layer |
|---|---|---|---|---|---|
| **499** | 859* | 765* | 1311* | 1078* | **1003*** |
| **356** | 409 | 213 | 514 | 481 | **403±80** |
| **214** | 157 | 275 | 198 | 192 | **205±80** |
| **71** | 183 | 130 | 196 | 178 | **172±80** |
| **Average** | **402** | **346** | **554** | **483** | **392±40** |

* values calculated to account for the difference between the hydrogen content measured by VHE.

Since a hydrogen rim is formed, it cannot be measured well with image analysis; therefore, the excess amount of hydrogen is added in layer 1. This calculated content has been made in such way to keep the ratio of hydrogen present in each zone the same. The data shows an azimuthal dependence here. However, no data was given as to neighboring pin power profile, presence of a water rod or the presence of spacer grids that could provoke these azimuthal variations. In that regard, only the averaged values over the azimuth were used.

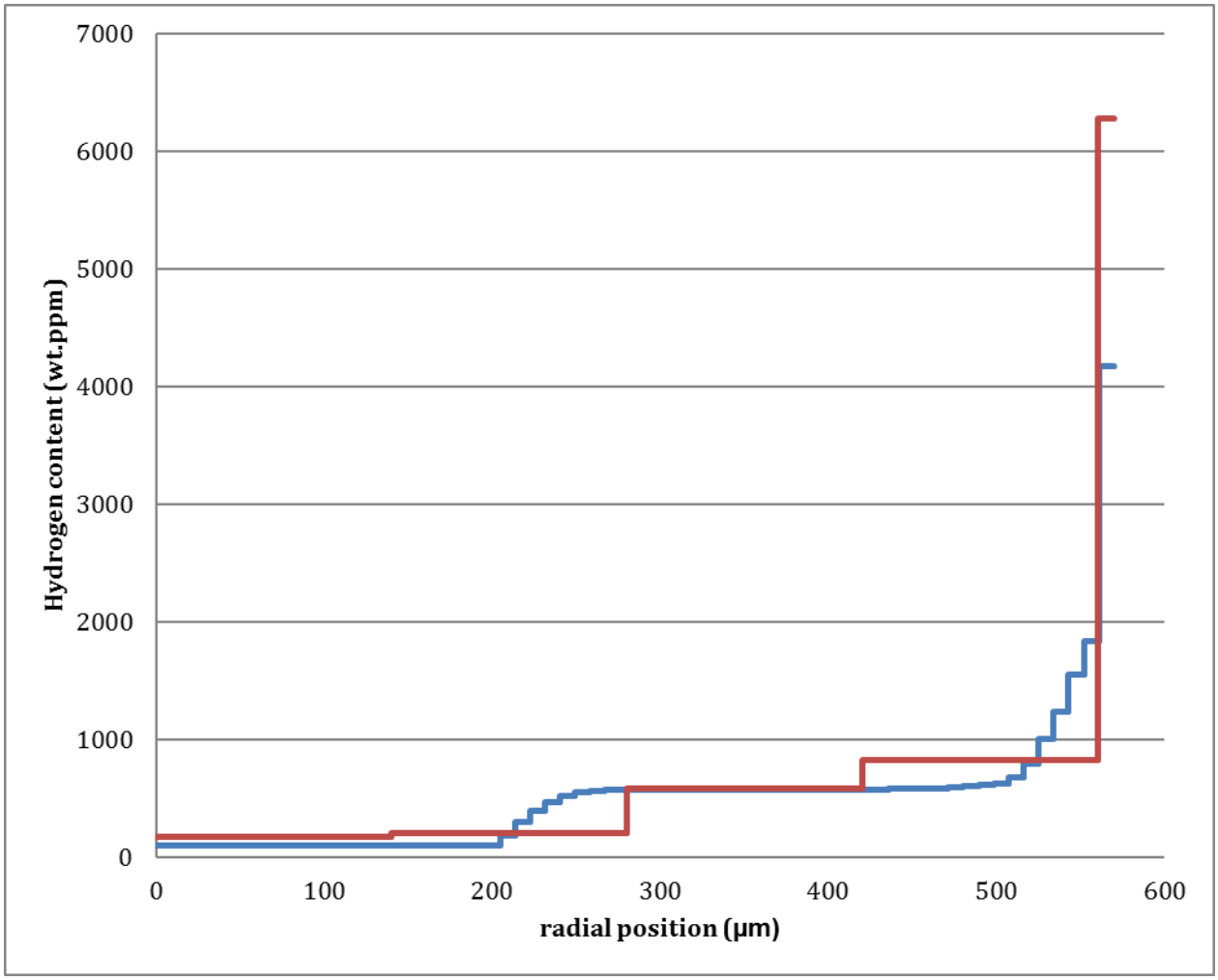


*Figure 6-3: BISON results (blue) versus experimental observations (red).*

As we can see in Figure 6-3, the results match the experimental data very well. However, the hydride rim hydrogen content seems to be underestimated by BISON. This may come from the homogeneous hydrogen distribution in the cladding instead of the slow introduction of hydrogen with oxide growth. This has been done and explained in a previous report, showing that if the hydrogen comes through the oxide/metal interface, all the hydrogen precipitates within the first few mesh cells from the metal/oxide interface. This comes from the fact that BISON does not take into account the randomness of nucleation as explained in a previous report and in [79], which implies that hydrides can precipitate without the need of zirconium hydride nuclei, and thus precipitate at the coldest spot possible.

### 6.1.2 Cruas

The Cruas' fuel pin is characterized by the parameters given in Table 6-3 and by the power profile given in Figure 6-4 . Given this data plus the hydrogen content that was measured by vacuum hot extraction and by image analysis in hot cells by J.-H. Zhang [20], it is possible to simulate the hydrogen distribution in this portion of cladding with BISON and compare it to the experimental data reported in Table 6-4. This comparison is shown in Figure 6-5.

*Table 6-3 Cruas fuel pin and reactor characteristics.*

| | | | |
|---|---|---|---|
| **Clad Material** | Zircaloy-4 | **Number of cycles** | 5 |
| **Fuel** | $UO_2$ | **Enrichment (%5U)** | 3.25 |
| **Z position (mm)** | 3083 | **Burnup (MWd/tU)** | 39635 |
| **Outside diameter (mm)** | 9.51 | **Inside diameter (mm)** | 8.35 |
| **Pressure (bars)** | 155 | **Mass Flux (g cm-2s-1)** | 314 |
| **Inlet Enthalpy (J $g^{-1}$)** | 1264 | **Inlet Temperature (°C)** | 286 |
| **Outlet Temperature (°C)** | 323 | | |

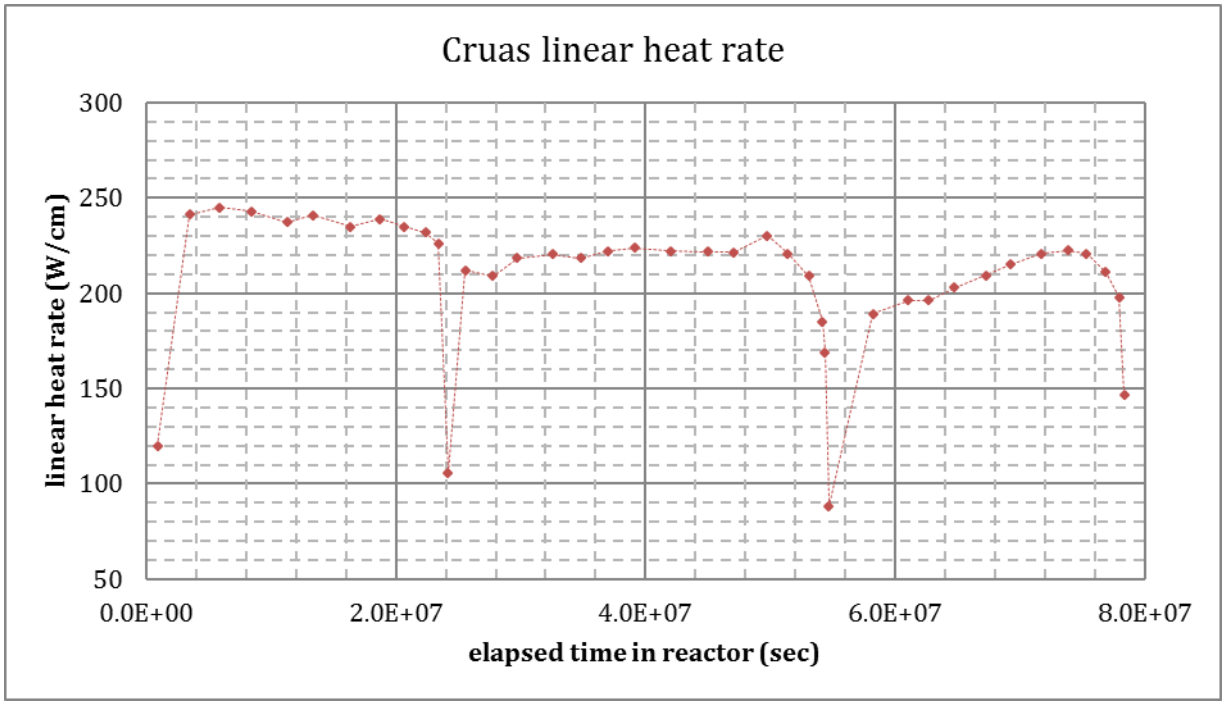


*Figure 6-4: Cruas' power history.*

*Table 6-4 Cruas fuel pin and reactor characteristics*

| Radial position (µm) | Top | Bottom | Right | left | Average [H] per layer |
|---|---|---|---|---|---|
| **499** | 668 | 774 | 1243 | 651 | **834*** |
| **356** | 78 | 234 | 228 | 78 | **154±80** |
| **214** | 111 | 101 | 106 | 102 | **105±80** |
| **71** | 127 | 155 | 155 | 197 | **159±80** |
| **Average** | **246** | **316** | **433** | **257** | **313** |

* values calculated to account for the difference between the hydrogen content measured by VHE.

Since a hydrogen rim is formed, it cannot be measured well with image analysis; therefore, the excess amount of hydrogen is added in layer 1. This calculated content has been made in such way to keep the ratio of hydrogen present in each zone the same.

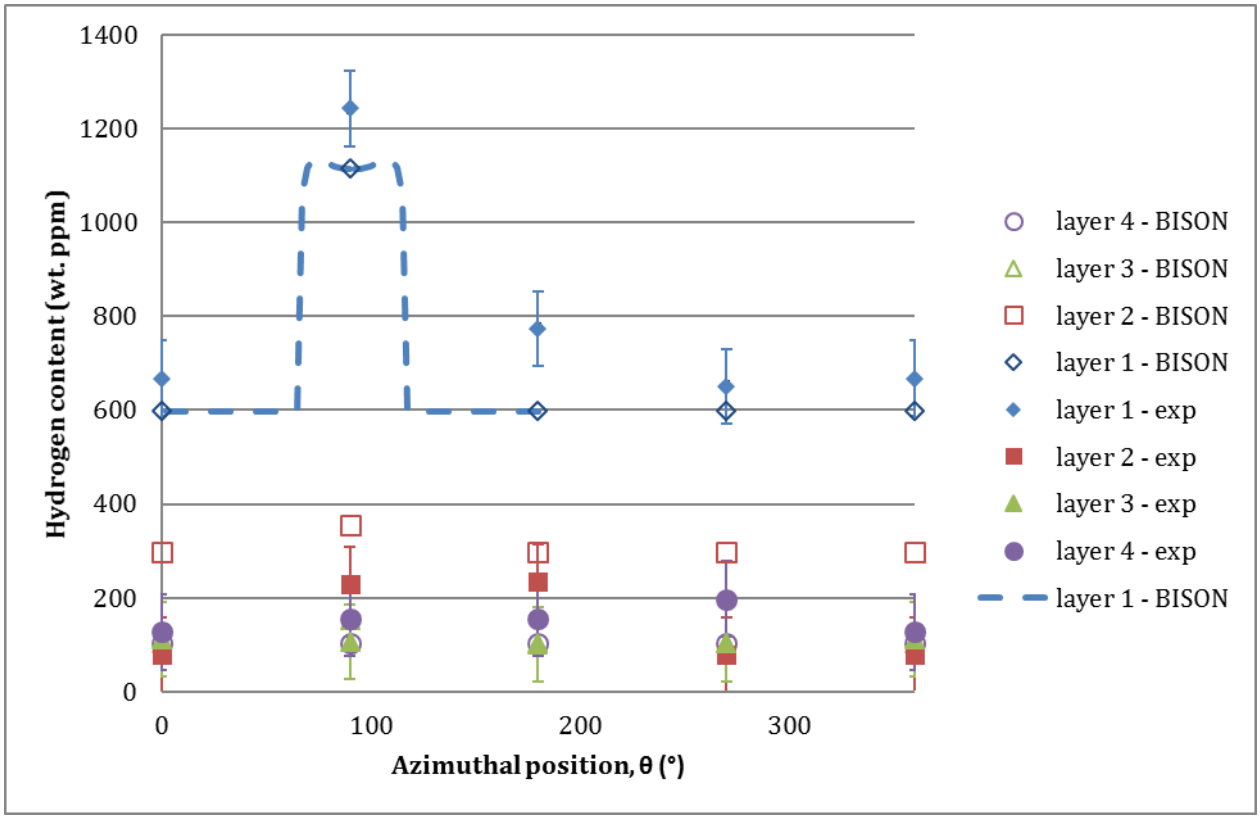


*Figure 6-5 Azimuthal hydrogen distribution. The points at 0° and 360° are the same.*

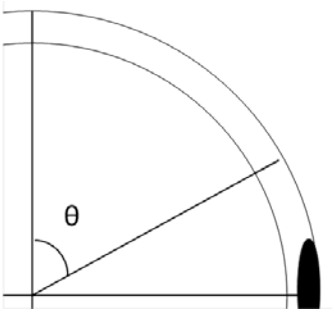


*Figure 6-6 definition of theta.*

θ is defined by Figure 6-6. It can be seen that the results are very close to the hydrogen content observed in the reactor data. A few differences are observed like the underestimation of the hydrogen content in layer one, which was already observed in the previous run. However, it is seen that the hydrogen migration towards the spalled region is well represented.

Some experimental data like the 78 wt.ppm of hydrogen in the layer 2 are very surprising. When the reactor is on, the outside cladding thickness is about 600K at these axial positions. At this temperature, the hydrogen in solid solution is about 140 wt. ppm. so considering that hydrogen present precipitates upon shutdown, one would expect to see at least that amount of hydrogen, if not more, as seen in layer 2 at $\theta = 180°$.

A study of the influence of the oxide spallation on the hydrogen distribution has been made from the hydrogen distribution given by BISON, given how close the hydrogen distribution given is from experimental data. 5 radial distributions at 5 different azimuthal positions were studied and were

plotted in Figure 6-7. The first position is nearly 90° away from the middle of the blister and each other azimuthal position are closer to the blister until being in the center of the spalled region.

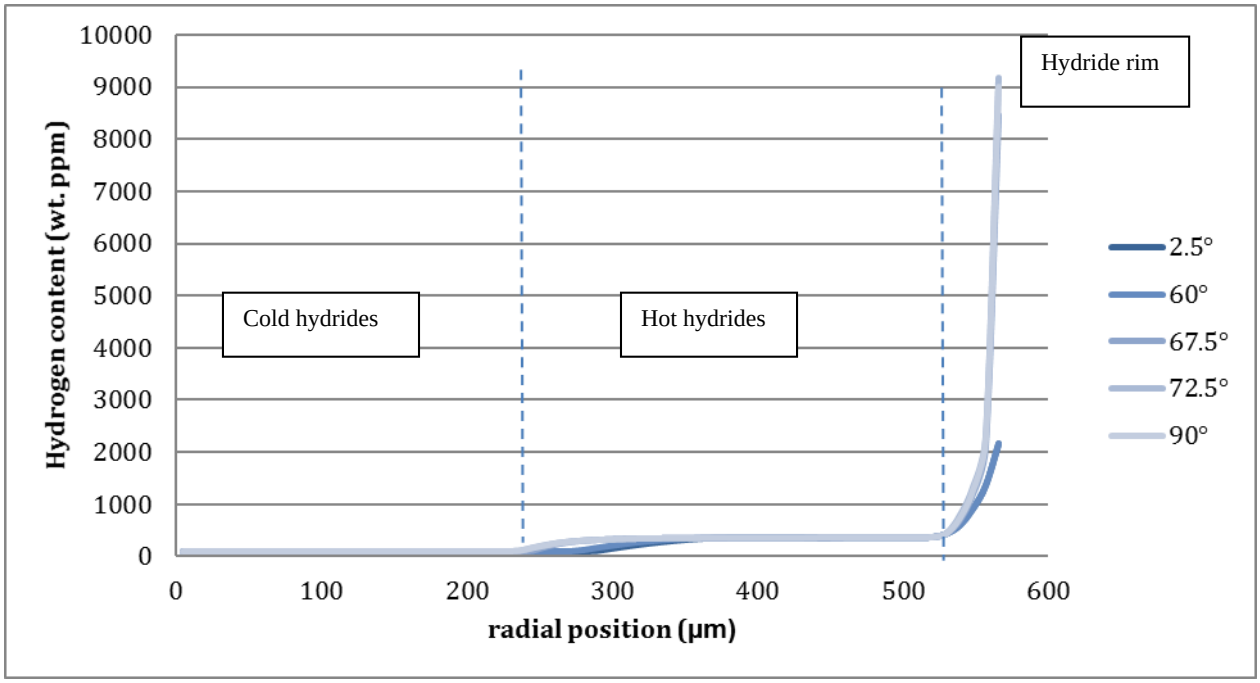


*Figure 6-7 radial hydrogen distribution at different azimuthal position.*

As it can be observed, there is a very big variation of hydrogen in the range of the cladding. Therefore, the plot of two closer windows has been made to evaluate better what is going on. These two regions are represented by Figure 6-8 and Figure 6-9. Three regions are represented in the hydride distribution. They were called cold hydride region, hot hydride region and hydride rim.

a) The cold hydride region is characterized by a low hydrogen content that corresponds to hydrogen in solid solution during reactor operation that precipitate as the reactor shuts down, typically ~150 wt. ppm

b) The hot hydride region is characterized by a higher hydrogen content that depends on the total hydrogen content of the sample. Here the hydrogen content of that region is about 350 wt.ppm

c) The hydride rim region is the very high hydrogen content region, and is defined here as the moment when the hydride content starts to increase after the hot hydride region. Its content is usually in 1,000s of wt.ppm [72] and only present in a small region. Here, by the standards explained, the rim is about 40 µm thick.

Figure 6-7 and Figure 6-8 show the evolution of the transition between each region. Figure 6-7 shows the transition between the cold to hot hydride regions and Figure 6-8 shows the transition between the hot hydride to hydride rim regions. By plotting these regions at different azimuthal position, we can see the influence of the spalled oxide on these transitions.

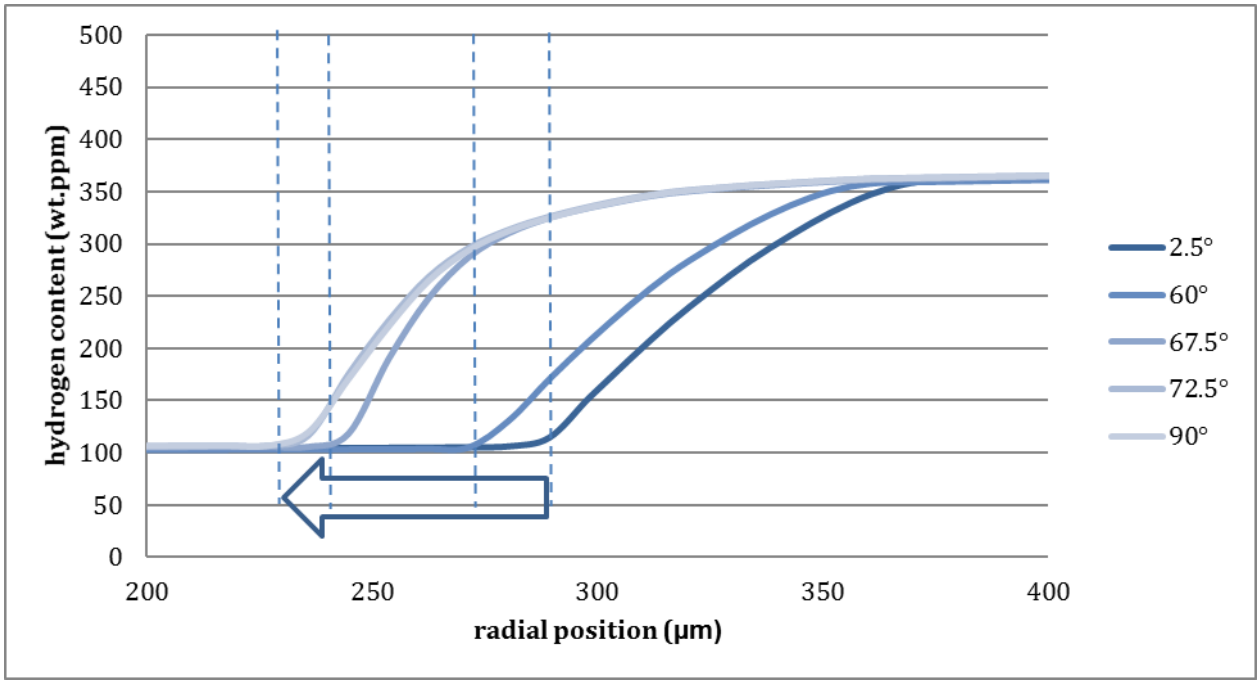


*Figure 6-8 evolution of the transition between the hot and cold hydride region with respect to the distance from the spalled oxide region.*

As we can see, as the cold spot (from oxide spallation) comes closer, the transition happens further away from the metal/oxide interface. Moreover, we can see that the hydride content varies in a much sharper way in the spalled region (67.5° and above). If we consider that the 2.5° region does not "see" the cold spot, we have the "normal" transition distance that is 289 µm. A summary of the transitions is shown in Table 6-5.

*Table 6-5 transition position between hot and cold hydride regions evolution with azimuthal position.*

| Azimuthal position | Transition distance (from oxide/metal) |
|---|---|
| 2.5° | 281 µm |
| 60° | 290 µm |
| 67.5° | 300 µm |
| 72.5° | 334 µm |
| 90° | 334 µm |

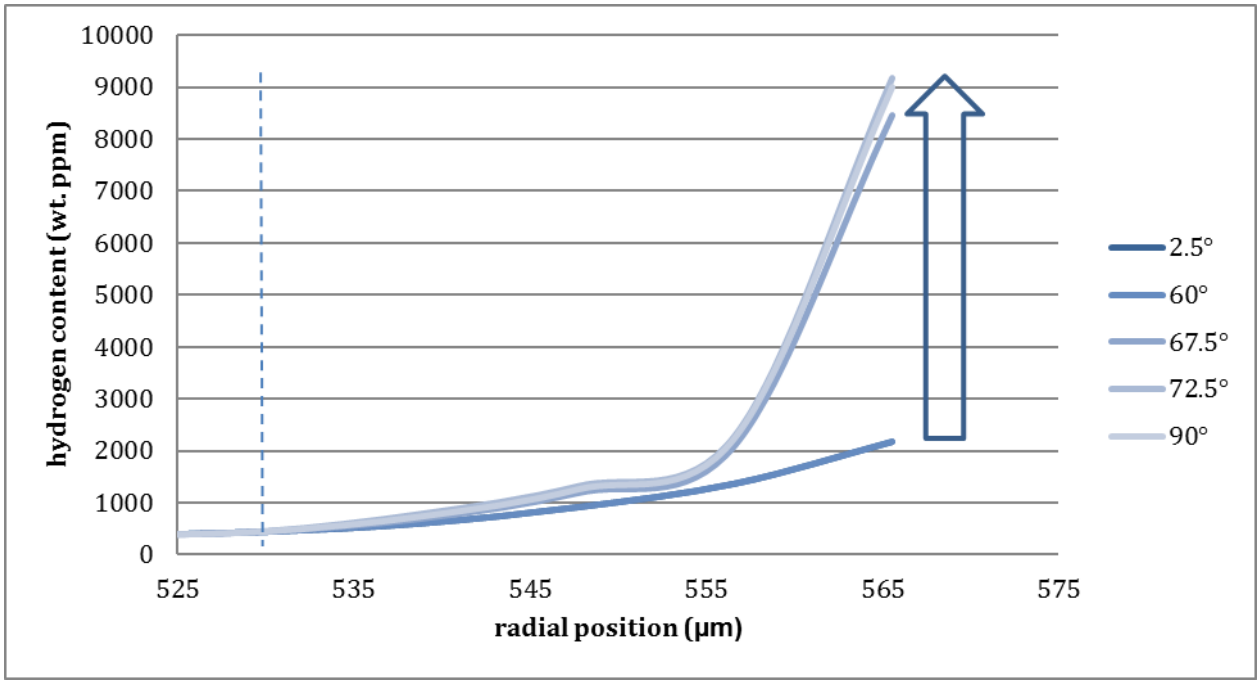


*Figure 6-9 evolution of the transition between the hot hydride and hydride rim regions with respect to the distance from the spalled oxide region.*

In Figure 6-9, we can see that the transition seems to be the same regardless of the position, happening at r ≈ 530 µm. however, the hydrogen content increases drastically from 2,172 wt. ppm to over 9,000 wt. ppm. Considering the history of the model under-predicting the hydride rim hydrogen content, it is probable that the hydrogen content in the rim is very close to being a pure hydride blister, which has been observed before when the oxide spalled previously. It is to be noted that the hydrogen under-prediction in the rim would probably be fixed by the implementation of a nucleation model in BISON, thus allowing for hydrogen to come in through the metal/oxide interface.

# 7 Sensitivity analysis of the hydrogen behavior in the cladding to the level of resolution of the high fidelity codes

This chapter describes the performed comparative analysis between the hydrogen distribution results from BISON based on boundary conditions obtained from CFD code STAR-CCM+ to the results based on boundary conditions obtained from the CTF part of the coupled multi-physics system using TIAMAT within VERA. The boundary conditions from CFD have much higher resolution than the data from the subchannel code CTF. The goal of this analysis was to investigate how sensitive is the hydrogen distribution to the level of resolution of the implemented boundary conditions. The analysis performed follows the same principles described in chapter 4.

## 7.1 Modeling and simulations

The VERA model was a 5x5 subassembly with a guide tube in the center rod surrounded by 3.2% enriched UO2 fuel used in PWRs as shown in Figure 8-1. The parameters of the model are based on Godfrey[80]. The VERA parameters described in used in the analysis described in chapter 4 and summarized in Table 4-1 are implemented in this analysis here with only some parameters differ based on the size of the 5x5 sub-assembly. The assembly power was 1.64 MW and the coolant mass flow rate was 0.06025 MLbs/hr. The fuel enrichment was taken to be uniform over all the fuel rods and equal to 3.2% .A STAR-CCM+ based model was generated for the same parameters as described in chapter 5. The cladding outer surface temperature computed by the CTF part of TIAMAT was fed as a boundary condition to BISON. The same was done for the temperatures obtained from CFD.

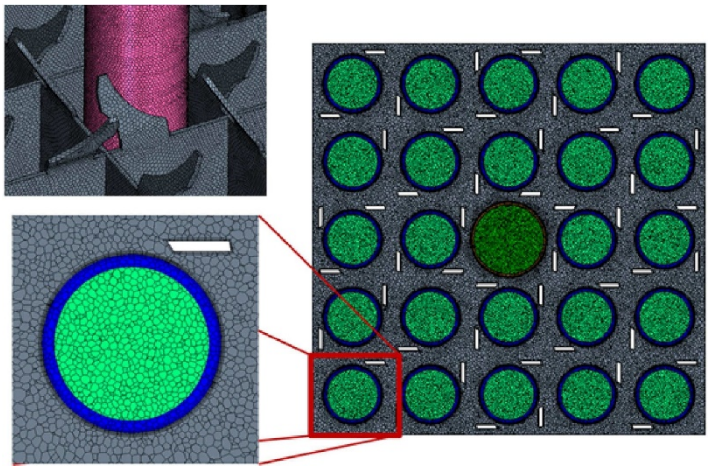

*Figure 7-1 plane view of the modeled sub-assembly.*

As done in Chapter 4, The boundary conditions from the multi-physics codes are fed to a stand-alone Bison model. Those BCs were extracted from the rod marked in Figure 8-1 to the north of the guide tube. The modelled partial rod is constituted of a five-pelleted fuel pin at a certain elevation of interest in the fuel. This section was at a location where a spacer grid with mixing vanes was located. It was important to investigate the effects of the drastic change in the temperature profile due to the mixing vanes on the exact locations to which the hydrogen diffuse or precipitate as hydrides. The chosen grid-spacer was the one with its mid-section located at a fuel height of 219.85 cm as shown in

Figure 4-3. The height of the modeled 5 pellets was 5.84 cm. and was extracted between fuel elevations of 217.0 cm at the bottom of the first pellet and 222.8 cm at the top of the upper pellet.

The mid-section of the spacer grid coincides with the mid slice of the modeled five pellets. The cladding outer surface temperature from TIAMAT was implemented in BISON using a parsed linear interpolation function. This function was used to perform interpolation between the four average temperatures on the outer surface of the cladding computed by CTF in each of the four subchannels surrounding the fuel rod of interest. Those are channels 9,10,15,16 illustrated in Figure 8-1. For the data obtained from STAR-CCM+, The number of data points implemented were around 2000 data point along the azimuthal and axial directions on the fuel surface. The interpolation between those data points was performed using the multilinear interpolation function implemented in MOOSE on the Cartesian coordinates.

The purpose of the analysis was to investigate the diffusion of hydrogen in 3D and its precipitation as hydrides. To do this, the rod is assumed to have an initial uniform hydrogen concentration in the solid solution of 150 ppm was assumed. The irradiation time was taken to be 13 days ($1.25x10^7$ s) as this is the range of time at which the data from Star-CCM+ were provided. This time, along with the chosen initial hydrogen concentration, was enough to lead to hydrogen diffusion and precipitation. This was sufficient to serve the purpose of assessing the functionality of the hydrogen model implemented in BISON. The hydrogen behavior based on the different sets of boundary conditions implemented was compared to assess the sensitivity of the hydrogen model to the level of resolution of the used temperature boundary conditions.

## 7.2 Hydrogen model with TIAMAT BCs

The sub-channel code CTF provided four average cladding outer surface temperature values for each of the subchannels that includes rod-7 in them. As shown in Figure 8-1, channels 9 and 10 have the same fuel rods enrichment for each of the four rods constituting them. The temperature on rod-7 surface in each of the channels is expected to be equal. The same is true for channels 15 and 16. Those have 3 fuel rods with equal enrichments plus a guide tube. The temperature on the fuel surface in each of them is expected to be equal too. The four temperature data points collected from CTF are provided in Table 8-1.

*Table 7-1 Average cladding surface temperature in each CTF subchannel*

| | Subchannel 9 | Subchannel 10 | Subchannel 15 | Subchannel 16 |
|---|---|---|---|---|
| Temperature(K) | 614.5 | 614.5 | 613.4 | 613.4 |

When interpolating the temperature value, the interpolation is expected to occur between the two channels between which the temperature changes from one value to another. That is between (channels 9 and 15) and (channel 10 and 16). The data from CTF did not show a large temperature gradient to drive a significant hydrogen gradient azimuthally. This case mainly to provide basis for comparison with the case based on the CFD data. This is shown Figure 8-2. The relatively colder region on the cladding is around the two subchannels containing the guide tube. The hotter region is between the two channels containing fuel pins only. The gradient in temperature is due to the interpolation between the two regions

In Figure 8-3, the re-distribution of Hydrogen in the fuel pin is depicted. The difference in the concentration between the hotter and cooler regions of the fuel is not so strong. This is due to the temperature gradient not being high enough to lead to excessive migration of the hydrogen from the cooler to the hotter regions. Nevertheless, the hydrogen distribution is consistent with the temperature profile shown in Figure 8-2.

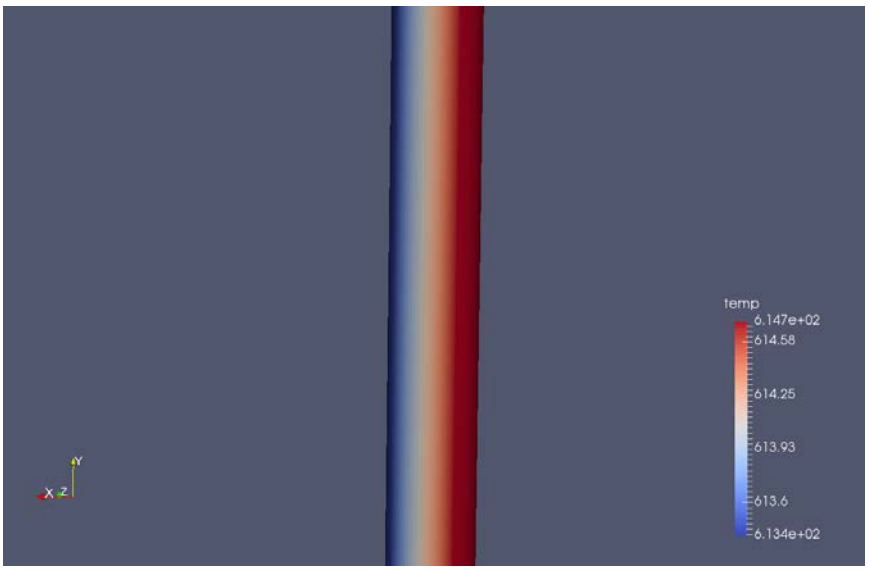


*Figure 7-2 Temperature profile on the outer surface of the cladding based on TIAMAT.*

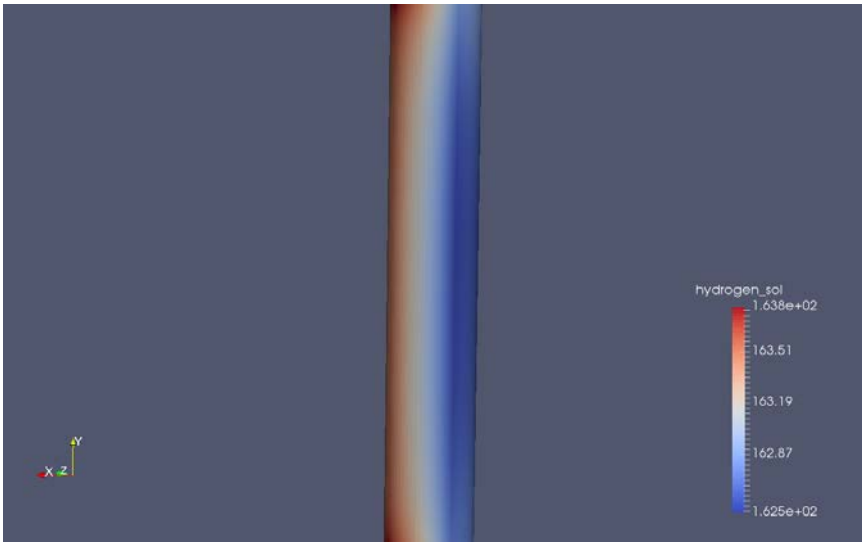


*Figure 7-3 Hydrogen distribution on the outer surface of the cladding.*

In Figure 8-4-a, the concentration of hydrogen in the hydride phase can be seen. We notice that there are rings with higher concentration of hydrides. Those rings are in the vicinity of the inter-pellet locations in the fuel. Around the inter-pellet regions, the temperature on the inner surface of the cladding is lower as shown in Figure 2-8. Hydrogen tends to migrate to those locations and precipitate on the form of hydrides. There can be noticed two axial lines as well with higher concentration of hydrogen in the hydrides. This is expected because those points represent the points after which the temperature does not vary in the azimuthal direction as shown in Figure 8-4-b. This leads to the loss of the power of the temperature gradient as a driving force for the migration of hydrogen in this

isothermal region which leads to the two axial lines of high concentration of hydrogen in the hydride phase.

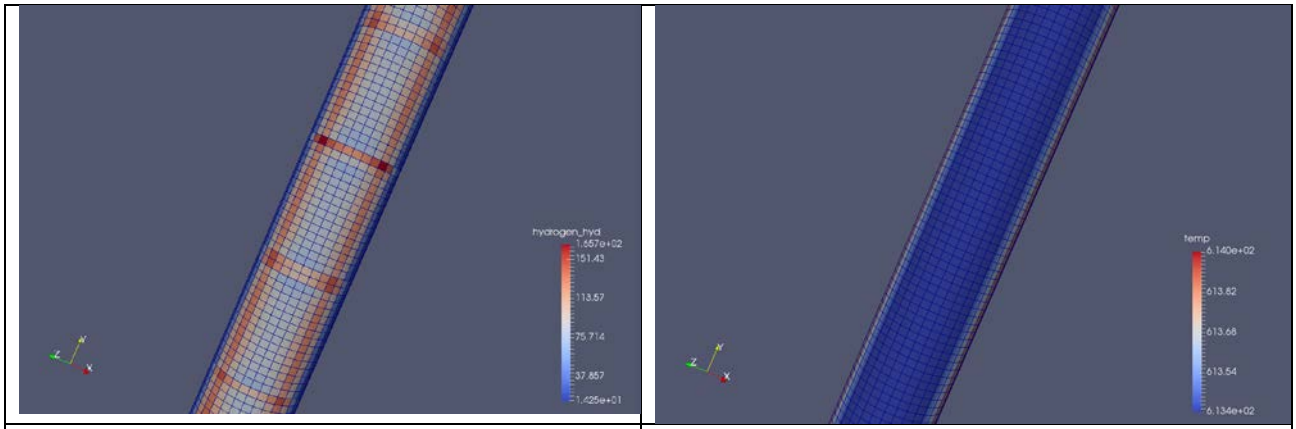


(a) (b)

*Figure 7-4 (a) Hydride formation on the outer surface of the cladding (b) the temperature profile with focus on the colder region.*

Figure 8-5 illustrates this azimuthal distribution of hydrogen explained above in a radial slice of the fuel pin. It can be seen that the change in the azimuthal distribution of hydrogen in the hydrides is the region where the temperature does not change is lower than the quick change on the other side. This is because when the temperature is constant, the diffusion of hydrogen is driven by the mass diffusion only while in the other region where the temperature changes, the hydrogen is driven by both the temperature and concentration gradients.

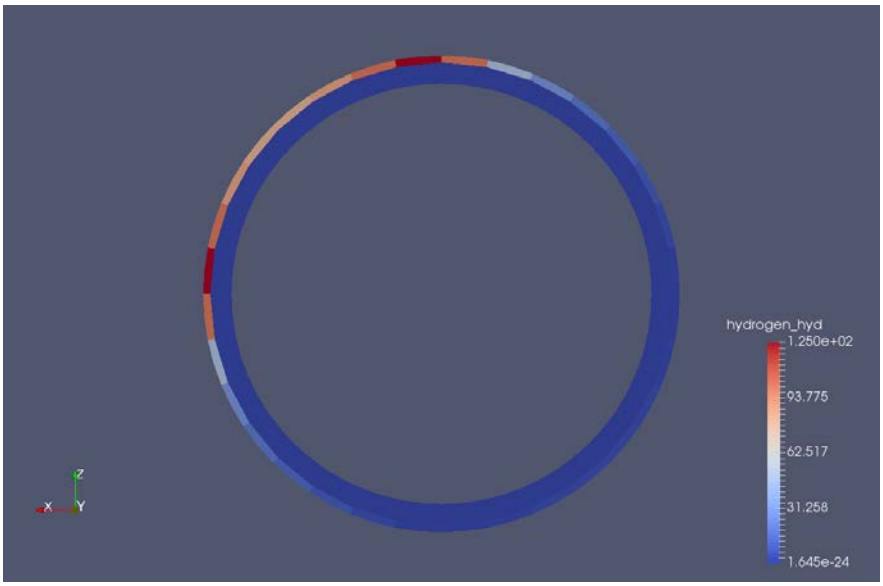


*Figure 7-5 The hydride formation in a radial slice of the fuel rod.*

## 7.3 Hydrogen model with STAR-CCM+ BCs

In this section, the boundary conditions obtained from the MPACT-STAR-CCM+-BISON coupling (chapter 5) were fed to the stand alone five-pellet partial fuel pin model. Similar work to what was done in section 8.2 was performed. The difference is that more than 1800 data points were used on the outer cladding surface in the azimuthal and axial directions. Between those points, a multi-linear

interpolation function was used to interpolate between the given data points. The space between the data points is small and the temperature difference between two adjacent points is not large enough to cause a significant error in the interpolation process. The same analysis as the one performed in section 8.2 was performed. The results obtained based on the hydrogen model were evaluated and analyzed here.

In Figure 8-6 the temperature profile on the outer cladding surface of the fuel pin is depicted. The level of details of the temperature profile in the azimuthal direction is obvious. On the top part of the fuel after the grid-spacer location, the effect of the mixing vanes is clearly seen. The significant decrease in the temperature and the redistribution of the hot and cold locations on the cladding surface due to the mixing vanes can be seen. The high-resolution level of details about the cladding outer surface temperature lead to a high-resolution hydrogen distribution in the cladding as well as shown in Figure 8-7.

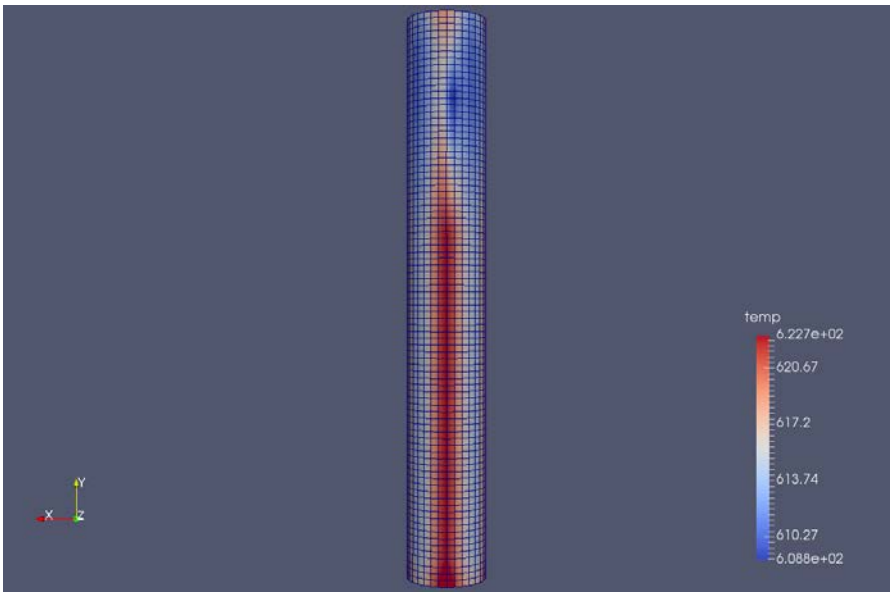


*Figure 7-6 Temperature profile on the outer cladding surface based on STAR-CCM+ data.*

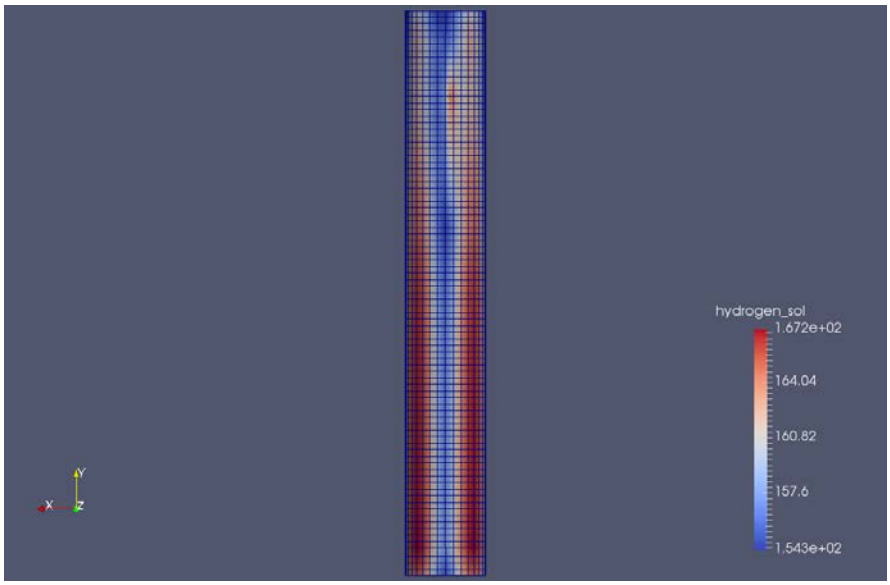

*Figure 7-7 Hydrogen distribution on the outer surface of the cladding.*

In Figure 8-7, the hydrogen distribution can be seen and its temperature dependence is clear when compared to Figure 8-6. The hydrogen migration to the lower temperature locations is obvious. The increase in the concentration of the hydrogen at the cooler spots will lead to an increase in the hydride formation due to two reasons. One is the lower temperature means lower TSSP values which leads to easier formation of hydrides. The other is the high abundance in the hydrogen compared to the lower TSSP limit will lead to more formation of hydrides. The formation of hydrides is illustrated in Figure 8-8. The relatively much lower temperature in the upper section of the rod (above the mixing vanes) leads to a high concentration of hydrides as explained in the previous paragraph. There are two axial lines of hydrides are formed as well due to the cooler regions around the cladding below and at the location of the grid-spacer.

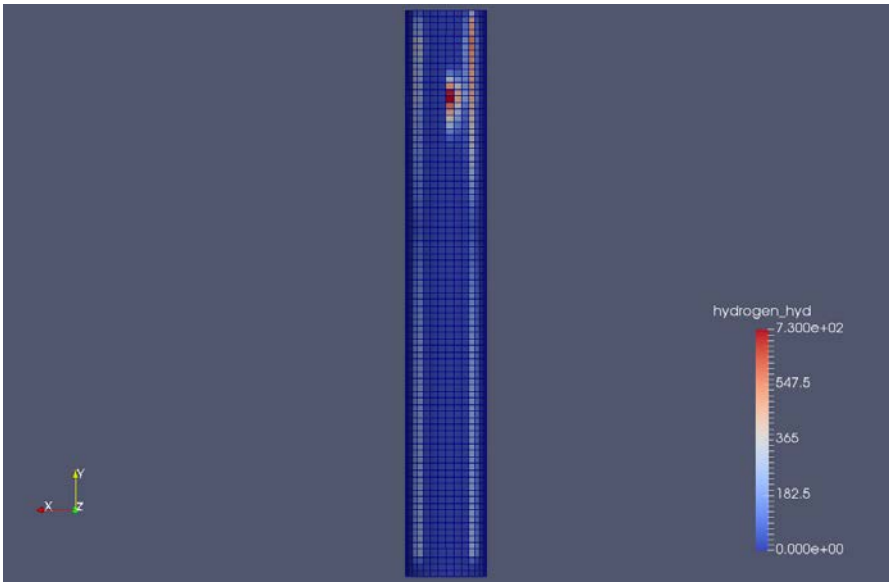


*Figure 7-8 Hydride formation on the outer surface of the cladding.*

A radial slice of the cladding was extracted at the location with the most hydrides formed (The strongest red color) in Figure 8-8. This is a location above the grid-spacer with the mixing vanes. This slice was extracted to demonstrate the radial and azimuthal distribution of the hydrogen and the formation of the hydrides and is depicted in Figure 8-9. It can be noticed in this figure how the high resolution outside temperature of the cladding affects even the temperature on the inner most points in the cladding. The hydrogen distribution (Figure 8-10) depends on this temperature profile and high-resolution distribution of hydrogen is obtained leading to a more accurate prediction of the exact locations to which hydrogen tends to migrate.

The locations at which hydrides are formed along with the concentrations of the hydrogen in hydrides is shown in Figure 8-11. The location with higher concentration of the hydrogen in solid solution are the locations in which more hydride phase is formed. The rim of hydrides on the outer surface of the cladding can be noticed along with the higher and lower concentration of hydrides in the rim depending on the temperature and concentration of the hydrogen in the solid solution.

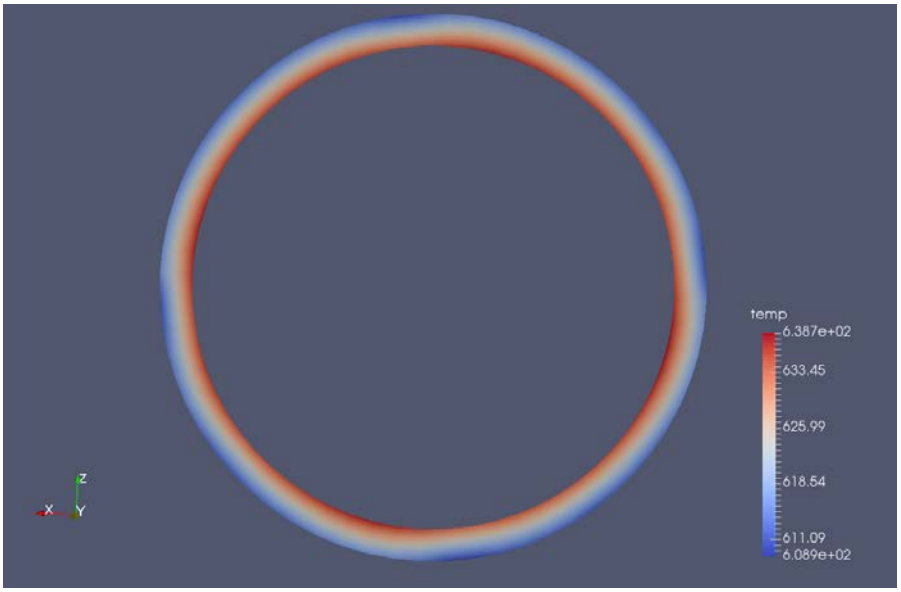


*Figure 7-9 Temperature profile in a radial slice of the cladding.*

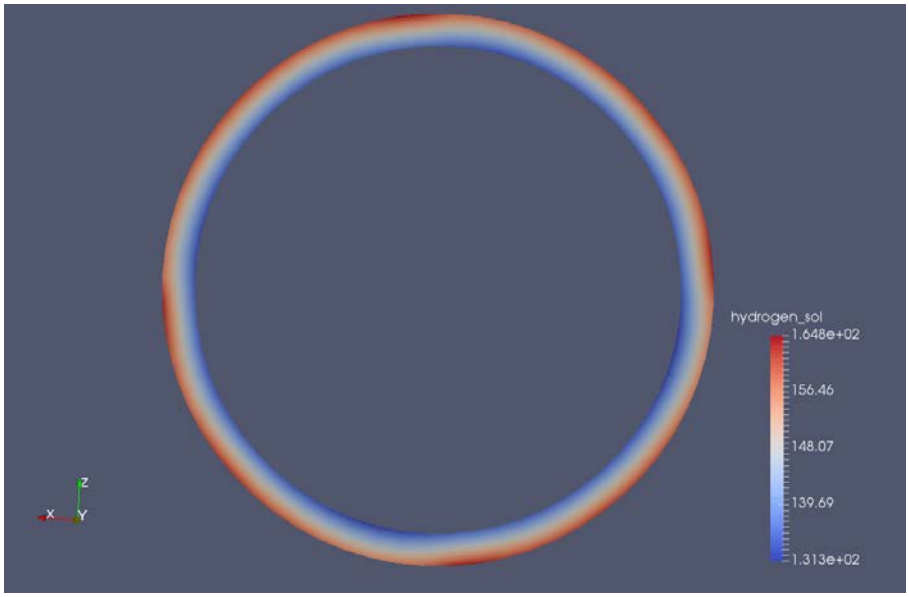


*Figure 7-10 The hydrogen distribution in a radial slice of the cladding.*

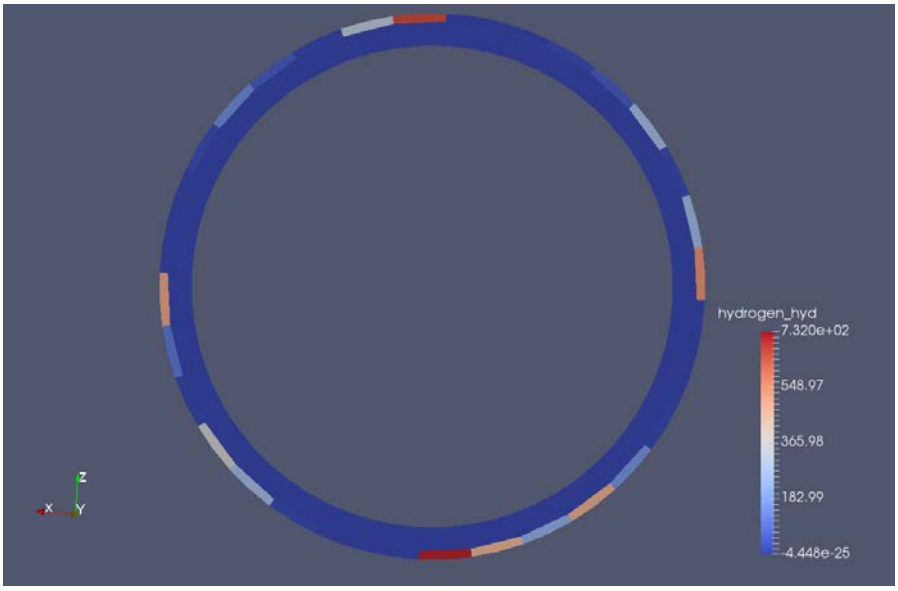


*Figure 7-11 The concentration of hydrogen as hydrides in a radial slice of the cladding.*

## 7.4 Sensitivity of the hydrogen diffusion to the level of resolution of the high-fidelity codes.

There were two sources of outer cladding boundary conditions used. One source is the four average cladding surface temperatures computed by CTF for each of the four subchannels surrounding the fuel rod. The second source is the data provided from the CFD code STAR-CCM+. The number of extracted and used data points are around 1800 data point. It is obvious that the boundary conditions from the STAR-CCM+ data are much refined and capturing a lot of details about the temperature profile on the cladding surface than the boundary conditions based on CTF. This is depicted in the comparison in Figure 7-12.

For the fuel configuration modelled here, CTF gave two values of temperature on the four quadrants of the cladding outer surface as shown in Table 7-1. In Figure 7-12 (a) the interpolation is done between those two values azimuthally. There is no axial change in the temperature and it was taken to be constant over the length of the five pellets modeled. This is because of the low resolution of the temperature outputs of CTF. On the other side in Figure 7-12 (b) the CFD data are able to capture the precise change of the temperature taking into account that there are locations closer to the fuel and should be hotter and that there are locations surrounded with more water and the temperature should be lower there. Also on the top part the effect of the rapid change of the temperature due to the mixing vanes is captured. This high gradient of temperature axially will lead to stronger diffusion of hydrogen to locations around the mixing vanes. This effect was not capture using CTF. Therefore, based on those different temperature profiles, the hydrogen diffusion and precipitation was expected to be highly sensitive to the level of resolution of the temperature boundary conditions data.

This is obvious and easy to see in Figure 7-13. In Figure 78-13 (a) The hydrogen distribution gradient follows the CTF's azimuthally varying and axially constant temperature profile. It diffuses to the slightly cooler regions on the cladding azimuthally. While it stays constant axially and the change noticed at the top and bottom of the pellets is due to the effect of the upper and lower plenums rather than the effect of the boundary conditions themselves. The effect of the mixing vanes is not captured

at all in this model. While when the CFD boundary conditions data were used, it is clear in Figure 7-13 (b) that the locations to which hydrogen diffuses are well defined and the upper and cooler locations around the mixing vanes in which the temperature decreases and becomes more uniform are the locations to which the hydrogen is attracted.

Eventually this difference in the temperature gradient driving force and the concentration of hydrogen in each finite element of the modeled case will affect the concentrations of hydrogen that precipitates as hydrides and the locations at which hydrides are formed as shown in Figure 7-14. Comparing Figure 7-14 (a) and (b), the difference in the prediction of the profile of the hydride formation is clear and not only the locations of formation but the concentration of the hydrogen in hydrides as well. The effect of the colder region due to the mixing vane and the rapid drop of temperature is the very higher concentration of hydrogen in hydride as shown in Figure 7-14 (b). This effect is not captured in Figure 7-14 (a) in which the rings of hydrides at the inter-pellet locations are captured. Those rings are due to the temperature drop on the inner surface of the cladding leading to the migration of hydrogen to those inter-pellet locations. In the vicinity of a grid spacer with mixing vanes, the gradient due to the drop in temperature due to coolant mixing is much higher than the drop at the inter pellet locations. This means that the hydride formation in Figure 7-14 (b) is more realistic for the modeled fuel section around the grid spacer than what is depicted in Figure 7-14 (a).

Based on the above discussion, it can be concluded the modelling of the hydrogen distribution and hydride formation is sensitive to the level of the resolution of the boundary conditions. Therefore, high fidelity codes with high resolution are needed to accurately predict the hydrogen behavior in the cladding, especially at locations or configurations in which the temperature gradient varies rapidly.

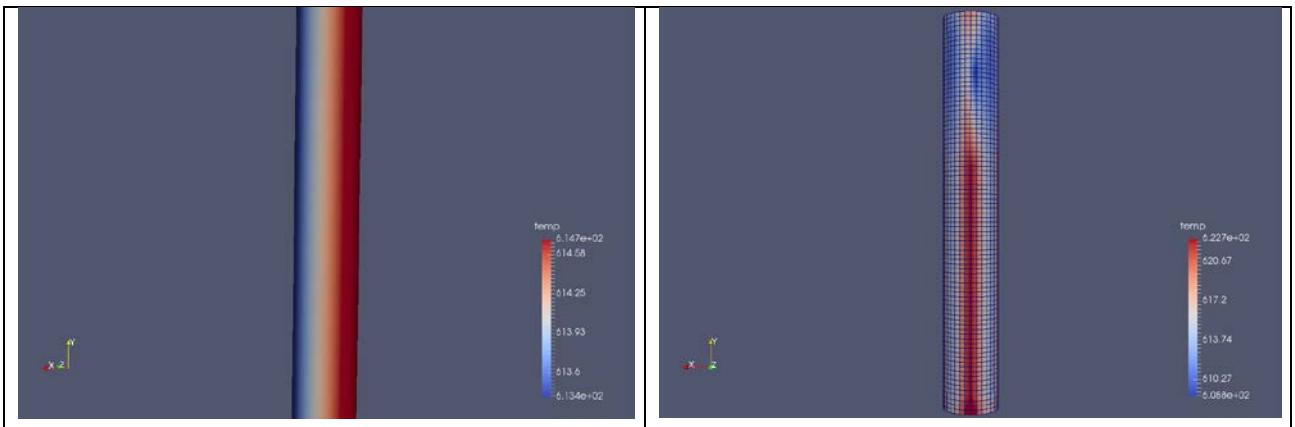


| (a) | (b) |
|---|---|

*Figure 7-12 A comparison between the temperature profile on the outer cladding surface based on (a) CTF and (b) STAR-CCM+.*

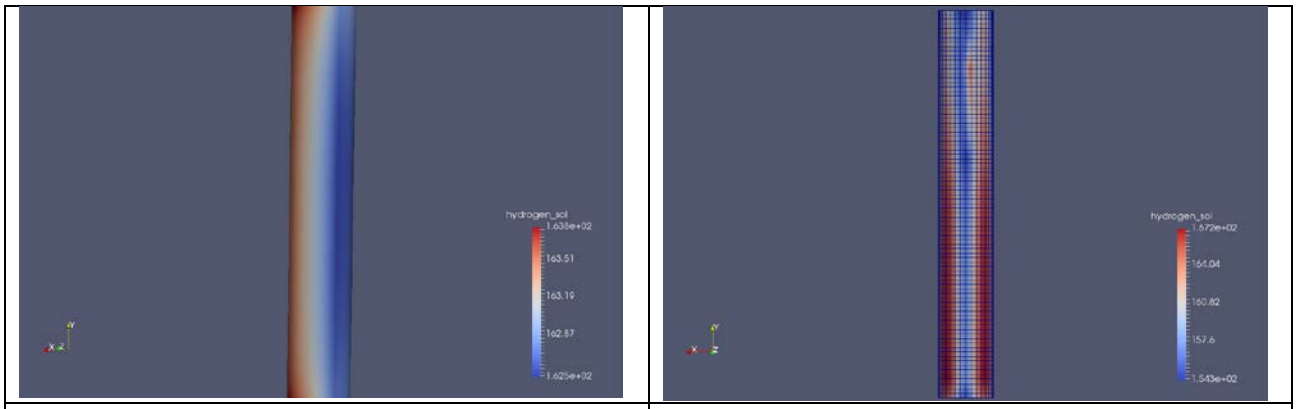


(a) (b)

*Figure 7-13 A comparison between hydrogen distribution on the cladding surface based on (a) CTF and (b) STAR-CCM+.*

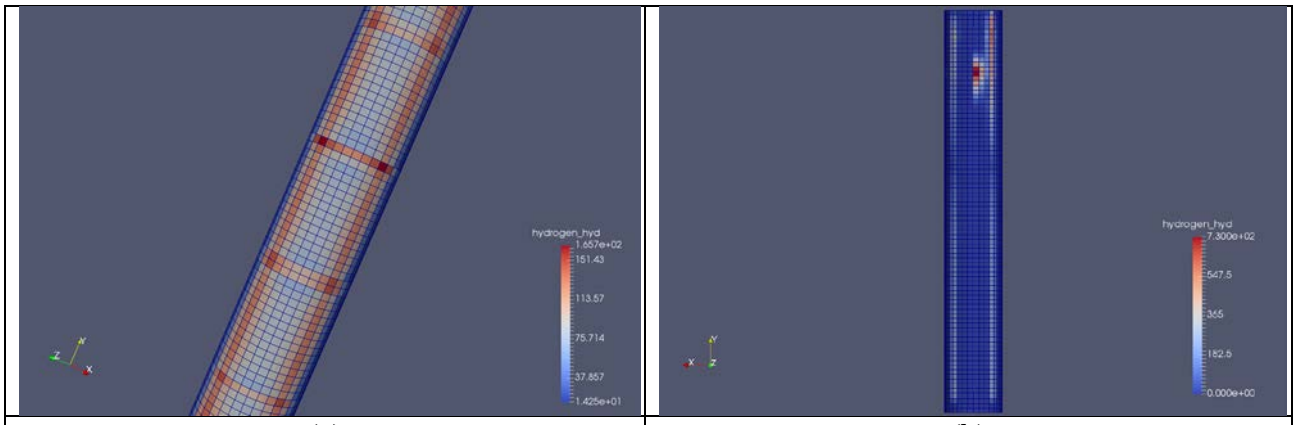


(a) (b)

*Figure 7-14 A comparison between the hydride distribution on the cladding surface based on (a) CTF and (b) STAR-CCM+.*

# 8 Conclusions

Due to the corrosive and oxidation effects of the coolant on the cladding, hydrogen can be picked up inside it. The pickup, diffusion and precipitation of hydrogen affect the ductility of the cladding. This makes it susceptible to damage and the cladding as a barrier to fission product release can be breached. The hydrogen is produced due to radiolysis of the water coolant or due to oxidation of the zirconium based cladding. An initial concentration of hydrogen of about 20 wt.ppm exists inside the cladding during its manufacturing process. The oxidation of the cladding is a temperature dependent phenomenon that leads to weight gain of the cladding. In the early life of the cladding the oxidation weight gain is governed by a cubic rate law. As the oxide thickness grows, the oxidation rate falls down then above a certain thickness a transition phase occurs and the oxidation rate becomes linear in time.

The oxidation reactions produce hydrogen. A fraction of about 15% of the produced hydrogen is picked up in the cladding. The absorbed hydrogen is redistributed in the cladding based on the concentration gradient governed by Fick's law and the temperature gradient governed by the Soret's effect. Radially, the relatively cooler outer surface of the cladding is a preferable location for the hydrogen to dwell in. The hydrogen forms a solid solution with the cladding occupying interstitial sites in the hcp α-zirconium lattice structure. Axially, locations with higher temperatures tends to have thicker zirconium oxide layer. More hydrogen is picked up at those locations then diffuses axially to locations with lower temperatures. The heterogeneity of the fuel lattice leads to asymmetry in temperature profile azimuthally leading to diffusion of hydrogen in the azimuthal direction. Therefore, there is a need of 3D modelling of the diffusion of hydrogen in the cladding.

As the concentration of hydrogen increases beyond TSSp, the hydrogen starts to precipitate on the form of immobile zirconium hydride. Hydrides tend to form near the outer surface of the cladding, where the concentration of hydrogen is higher, forming a rim of hydrides on the outer cladding surface. This rim is susceptible to cracking at 330 $^{o}$C which is near the normal operation and hot zero power conditions. Loss of ductility is also noticed due to the presence of the small cracks within the rim. The formed hydride can dissolve back to the solid solution if the hydrogen concentration decreased to lower than the TSSd value.

The model used to describe the hydrogen diffusion and precipitation depends on two constants that do not have consistent values in the literature. The heat of transport Q* which governs the Soret effect was measured by applying a temperature gradient to a Zircaloy plate that was previously charged with hydrogen. The measured value for Q* was 58.5 kJ/mol. The second constant is the rate of precipitation $\alpha^2$ from Marino, which describes the rate at which the supersaturated hydrogen in solid solution precipitates into zirconium hydrides. This rate is measured through an in-situ X-Ray diffraction experiment in transmission, at the Advanced Photon Source of the Argonne National Laboratory. Once those quantities were prepared, the model was implemented in BISON fuel performance code. BISON had a role in the investigation of the model's ability to predict the hydrogen behavior in the cladding and to investigate the importance of high-fidelity coupling codes in the prediction of the factors affecting the mechanisms of hydrogen diffusion and precipitation.

Two sets of coupled high-fidelity calculations were used in this project to investigate the hydrogen model. The coupling code TIAMAT was used to couple MPACT-CTF-BISON. MIMIC was used to couple MPCAT-STAR-CCM+-BISON. CTF is a subchannel code and STAR-CM+ is a CFD code. The two codes would produce different types of outer cladding temperature profiles that were fed to a stand-alone 3D-BISON model. While CTF returns four average cladding temperatures at each axial location. STAR-CCM+ as a CFD code has much higher resolution giving more than 300 data points at each axial location. The high resolution of the CFD boundary conditions reduced the errors due to the interpolation process. At locations around a spacer grid with mixing vanes, the accurate temperature profile is needed in order to accurately predict the hydrogen distribution profile in the cladding at that region of interest. This was shown in the simulations results. The Temperature profile based on CTF did not enable the BISON model to predict the effects of the mixing vanes and the exact locations of higher concentrations of hydrogen above them that were captured when the STAR-CCM+ boundary conditions were used. This highlights the sensitivity of the hydrogen distribution predicted by the model to the level of resolution of the boundary conditions used and how important is the usage of high fidelity codes in predicting the factors that might affect the model's behavior.

For now, the model for hydrogen distribution and precipitation is created and implemented in BISON. The importance and effects of high fidelity codes and high-resolution data for predicting the hydrogen distribution is assessed. The next step for the future work is to validate the results obtained by the model against data extracted from real experimental fuel rods. Those kinds of data are not currently available. Once such experiments are performed, the hydrogen distribution at the operation power and temperatures of the fuel will be measured. With the availability of those data related to the hydrogen distribution, validation of the model can be performed.

# REFERENCES


[1] J. Lamarch, A. Baratta, **Introduction to Nuclear Engineering**, 3rd edition, Prentice Hall, 2001.

[2] C. Lemaignan, A. Motta, **Zirconium Alloys in Nuclear Applications,** Material Science and Technology. Vol. 10B 1994.

[3] C. Coleman, D. Hardie, **The hydrogen embrittlement of alpha-zirconium review,** Journal of less common metal, pp. 168-185., 1966.

[4] J-P Garner, **Alloy M5 in action Nuclear Engineering International**, *47(587):pp. 36-37, 2002.*

[5] G. Sabol, **Zirlo – an Alloy Development Success,** Zirconium in the nuclear industry: 14th international symposium. ASTM STP 1467: pp. 3-24, 2005.

[6] J. Clayton, **Cladding Corrosion and Hydriding in Irradiated Defected Zircaloy-4 Fuel Rods,** *Corrosion, 45(12): pp. 996-1002, 1989.*

[7] IAEA, **Waterside Corrosion of Zirconium Alloys in Nuclear Power Plants**, International Atomic Energy Agency: Vienna, 1998.

[8] F. Garzarolli, et al. **Review of Corrosion and Dimensional Behavior of Zircaloy under Reactor Water Conditions.** 1979, ASTM.

[9] A. Yilmazbayhan, et al., **Transmission Electron Microscopy Examination of Oxide Layers Formed in Zr Alloys.** Journal of Nuclear Materials, 2006. **349**: pp. 265-281.

[10] L. Siefken, et al., **MATPRO - A Library of Materials Properties for Light-Water-Reactor Accident Analysis**, *SCDAP/RELAP5/MOD 3.3 Code Manual Vol.4, Rev. 2*, 2001.

[11] A. Couet, A. Motta, R. Comstock, ***Effect of Alloying Elements on Hydrogen Pick-up in Zirconium Alloys***, in *7th International Symposium on Zirconium in the Nuclear Industry* to be published: Hyderabad, India.

[12] Couet, A., Motta, A.T., Comstock, R.J., **Hydrogen Pickup Measurements in Zirconium Alloys: Relation to Corrosion Rate.** Journal of Nuclear Materials, to be published.

[13] A. Racine, **Influence de L'orientation des Hydrures sur les Modes de Deformation, D'endommagement et de Rupture du Zircaloy-4 Hydrure,** Ph.D. Thesis, Mecanique et Materiaux, L'Ecole Polytechnique, France, 2005.

[14] J. Elston, *Hydrures*, ed. G. Atomique1965: INSTN-PUF.

[15] R. Daum, **Hydride Induced Embrittlement of Zircaloy-4 Under Plane Strain Tension Testing,** PhD Thesis in Materials Science, Penn State University, 2007.

[16] R. Daum, **Radial-Hydride Embrittlement of High-burnup Zircaloy-4 Fuel Cladding,** Journal of Nuclear Science and Technology, 2006. **43**(9): p. 1054–1067.

[17] M. Billone, et al., **Cladding Embrittlement During Postulated Loss-of-Coolant Accidents**, 2008, NRC.

[18] P. Bossis, et al., **Comparison of the High Burnup Corrosion on M5 and Low Sn Zircaloy-4,** Journal of ASTM International, 2006. **3**(1): p. paper IDJAI12404.

[19] J. Arborelius, L. Hallstadius, P. Jourdain, T. Andersson, R. Lisdat, M. Hahn, E. Toscano, **The Effect of Duplex Cladding Outer Component Tin Content on Corrosion, Hydrogen Pick-**

**up, and Hydride Distribution at Very High Burnup.** Journal of ASTM International, 2005. **STP 1467**: p. 526-546.

[20] J. Zhang, **Hydruration du Zircaloy-4 et étude de la Distribution de L'hydrogène Dans une Gaine de Combustible REP,** PhD Thesis, Department de Mecanique et de technologie, Commissariat à l'Énergie Atomique, 1993.

[21] G. Smith, **Evaluation and Demonstration of Methods for Improved Fuel Utilization**, in *ET/34013-15, CND-432*1994, DOE.

[22] P. Guedeney, M. Trotabas, M. Boschiero, **Fragema Fuel Behavior and Rupture of Hydrdided Zircaloy-4,** ANS Topical Meeting on LWR fuel performance, 1991: p. 627-638.

[23] J. Kearns, **Diffusion Coefficient of Hydrogen in Alpha Zirconium, Ziraloy-2 and Zircaloy-4,** J. Nuclear Materials, 1972. **43**: p. 330-338.

[24] B. Kammenzind, H. Peters, W. Duffin, **Hydrogen Pickup and Redistribution in Alpha-Annealed Zircaloy-4,** Zirconium in the Nuclear Industry: 11th International Symposium, 1996. **ASTM STP 1295**: p. 338-370.

[25] D. Prigogine, *Modern Thermodynamics*1998: John Wiley & Sons.

[26] A. Sawatzky, E. Vogt, **Mathematics of the Thermal Diffusion of Hydrogen.** Transactions of the Metallurgical society of AIME, 1963. **227**(4): p. 917-928.

[27] K. Colas, **Fundamental Experiments on Hydride Reorientation in Zircaloy,"** PhD Thesis in Mechanical and Nuclear Engineering, Pennsylvania State University, 2012.

[28] J. Kearns, **Terminal Solubility and Partitioning of Hydrogen in the Alpha Phase of Zirconium, Zircaloy-2 and Zircaloy-4,** Journal of Nuclear Materials, 1967. **22**: p. 292-303.

[29] M. Puls, **Elastic and Plastic Accommodation Effects on Metal-Hydride Solubility,** Acta Metallurgica, 1984. **32**: p. 1259.

[30] M. Puls, **Effects of Crack Tip Stress and Hydride-Matrix Internal Stresses on Delayed Hydride Cracking.** Metallurgical Transactions A, 1990. **21**: p. 2905.

[31] G. Carpenter, **The Precipitation of [Gamma]-Zirconium Hydride in Zirconium, Acta Metallurgica**, 1978. **26**(8): p. 1225-1235.

[32] Z. Zhao, **Identification and Characterization of a New Zirconium Hydride,** Journal of Microscopy, 2008. **232**: p. 410.

[33] M. Kerr, M., **Fracture of a Minority Phase at a Stress Concentration Observed with Synchrotron X-ray Diffraction,** Scripta Materialia, 2009. **61**(10): p. 939-942.

[34] Z. Pan, I. Ritchie, M. Puls, **The Terminal Solid Solubility of Hydrogen and Deuterium in Zr-2.5Nb Alloys,** Journal of Nuclear Materials, 1996. **228**: p. 227-237.

[35] A. McMinn, E. Darby, J.S. Schofield. **The Terminal Solid Solubility of Hydrogen in Zirconium Alloys,** in *12th Int. Symp. on Zr in the Nuclear Industry*. 2000. Toronto, CA: ASTM.

[36] A. Sawatzky, "**Hydrogen in Zircaloy-2: Its Distribution and Heat of Transport,** Journal of nuclear Materials, 1960. **4**: p. 321-328.

[37] Shewmon, "**Redistribution of Second Phase during Annealing in Temperature Gradient,** Transactions of the Metallurgical Society of AIME, 1958. **212**: p. 642-647.

[38] G. Marino, **Hydrogen Supercharging in Zircaloy,** Materials Science and Engineering, 1971. **7**(1971): p. 335-341.

[39] G. Marino, *HYDIZ:* **A 2-Dimensonal Computer Program for Migration of Interstitial Solutes of Finite Solubility in a Thermal Gradient (LWBR Development Program)**, in *AEC Research and Development Report - WAPD-TM-1157*1974.

[40] A. McMinn, E. Darby, J. Schofield, **The Terminal Solid Solubility of Hydrogen in Zirconium Alloys.** Zirconium in the Nuclear Industry: Twelfth International Symposium, 2000. **ASTM STP 1354**: p. 173-195.

[41] A. Menibus, **Formation de Blisters D'hydrures et Effet sur la Rupture de Gaines en Zircaloy-4 en Conditions D'accident D'injection de Reactivite,** PhD Thesis in Sciences et Genie des Materiaux, Ecole Nationale Superieure des mines de Paris, 2012

[42] M. Jovanovic, A. Stern, A. Kneis, G. Weatherly, M. Leger, **Thermal Diffusion of Hydrogen and Hydride Precipitation in Zr-Nb Pressure Tube Alloys,** Canadian Metallurgical Quarterly, 1988. **27**: p. 323-330.

[43] H. Hong, S. Kim, and K. Lee, **Thermotransport of hydrogen in Zircaloy-4 and modified Zircaloy-4.** Journal of Nuclear Materials, 1998. **257**: p. 15-20.

[44] A. Sawatzky, **The Heat of Transport of Hydrogen in Zirconium Alloys,** Journal of nuclear Materials, 1963. **9**(3): p. 364.

[45] M. Sugisaki, K. Hashizume, Y. Hatano, **Estimation of Hydrogen Redistribution in Zircaloy Cladding of Spent Fuel under Thermal Conditions of Dry Storage and Evaluation of its Influence on Mechanical Properties of the Cladding,** IAEA, 2002.

[46] S. Morozumi, M. Kitada, K. Abe, S. Koda, **Effects of the Alloying Elements and Cold Work on the Redistribution of Hydrogen in Zirconium under a Temperature Gradient,** Journal of Nuclear Materials, 1969. **33**: p. 261-270.

[47] K. Hashizume, M. Hayakawa, M. Koganemaru, M. Sugisaki, **Temperature Dependence of Heat of Transport of Hydrogen in Zirconium,** Defect and Diffusion Forum, 1993. **95-98**: p. 323-328.

[48] J. Markowitz, **The thermal Diffusion of Hydrogen in Alpha-delta Zircaloy-2,** Transactions of the Metallurgical Society of AIME, 1961. **221**(819-823): p..

[49] B. Kammenzind, **Hydrogen Pickup and Redistribution in Alpha-annealed Zircaloy-4,** Zirconium in the Nuclear Industry: Eleventh International Symposium, ASTM STP 1295, 1996. p. 338-370.

[50] http://www.surfaceigniter.com/, *Surface Igniter*, in. p.

[51] B. Kammenzind, D. Franklin, H. Peters, W. Duffin, **Hydrogen Pickup and Redistribution in Alpha-Annealed Zr-4.** in *Zirconium in the Nuclear Industry: 11th International Symposium*. 1996. p. 338-370.

[52] D. Douglass, **The Metallurgy of Zirconium.** ed. Vol. 1971, Vienna: International Atomic Energy Agency Supplement.

[53] **Analysis of Zirconium Alloys,** Luvak Inc., 1999.

[54] K. Colas, **Fundamental Experiments on Hydride Reorientation in Zircaloy,** PhD Thesis in Mechanical and Nuclear Engineering, Pennsylvania State University, 2012.

[55] B. Cullity, **Elements of X-ray Diffraction,** Second Edition ed., ed. Vol. 1978: Addison-Wesley Publishing Company, Inc.

[56] **The Powder Diffraction File,** International Center for Diffraction Data, 2006.

[57] U.S.DOE, **The Advanced Photon Source, A National Synchrotron Radiation Research Facility at Argonne National Laboratory,** April, 1999.

[58] D. Haeffner, J. Almer, U. Lienert, **The Use of High Energy X-rays from the Advanced Photon Source to Study Stresses in Materials,** Materials Science and Engineering: A, 2005. **399**(1-2): p. 120-127.

[59] A. Larson, R. Dreele, **General Structure Analysis System (GSAS),** Los Alamos National Laboratory, LAUR 86-748, 2000.

[60] O. Courty, A. Motta, C. Piotrowski, J. Almer, **Hydride Precipitation Kinetics in Zircaloy-4 Studied using Synchrotron X-ray Diffraction,** Journal of Nuclear Materials, 2015. **461**: p. 180-185.

[61] M. Blackmur, J. Robson, M. Preuss, O. Zanellato, R.J. Cernik, S.-Q. Shi, et al., **Zirconium Hydride Precipitation Kinetics in Zircaloy-4 Observed with Synchrotron X-ray Diffraction,** Journal of Nuclear Materials, 2015. **464**: p. 160-169.

[62] C. Piotrowski, **Azimuthal Hydrogen Concentration Factor using the BISON Fuel Performance Code,** MS Thesis in Nuclear Engineering, The Pennsylvania State University, State College, PA, 2014.

[63] B. Kammenzind, D. Franklin, H. Peters, W. Duffin, **Hydrogen Pickup and Redistribution in Alpha-Annealed Zircaloy-4,** Zirconium in the Nuclear Industry: Eleventh International Symposium, 1996, **ASTM STP 1295**: p. 338-370.

[64] K. Une, **Dissolution and Precipitation Behavior of Hydrides in Zircaloy-2 and High Fe Zircaloy,** Journal of Nuclear Materials, 2003. **322**: p. 66-72.

[65] R. Tang, X. Yang, **Dissolution and Precipitation Behaviors of Hydrides in N18, Zry-4 and M5 Alloys,** International Journal of Hydrogen Energy, 2009. **34**: p. 7269-7274.

[66] P. Vizcaino, A. Banchik, J. Abriata, **Solubility of Hydrogen in Zircaloy-4: Irradiation Induced Increase and Thermal Recovery,** Journal of Nuclear Materials, 2002. **304**: p. 96-106.

[67] G. Slattery, **The Terminal Solubility of Hydrogen in the Zirconium/2 at % chromium/0.16 at % Iron Alloy,** Journal of Nuclear Materials, 1969. **32**: p. 30-38.

[68] O. Zanellato, M. Preuss, J.-Y. Buffiere, F. Ribeiro, A. Steuwer, J. Desquines, et al., **Synchrotron Diffraction Study of Dissolution and Precipitation Kinetics of Hydrides in Zircaloy-4,** Journal of Nuclear Materials, 2012. **420**: p. 537-547.

[69] A. Sawatzky, **The Diffusion and Solubility of Hydrigen in the Alpha Phase of Zircaloy-2,** Journal of Nuclear Materials, 1959. **2**(1): p. 62-68.

[70] G. Östberg, **Determination of Hydride Solubility in Alpha Phase Zirconium, Zircaloy-2 and Zircaloy-4,** Journal of Nuclear Materials, 1962. **5**(2): p. 208-215.

[71] K. Almer, **Mechanisms of Hydride Reorientation in Zircaloy-4 Studied in Situ,** Zirconium in the Nuclear Industry: 17th International Symposium, 2014. p.

[72] O. Courty, A. Motta, J. Hales, **Modeling and Simulation of Hydrogen Behavior in Zircaloy-4 Fuel Cladding,** Journal of Nuclear Materials, 2014, **452**: p. 311-329.

[73] P. Vizcaino, A. Rios, **Hydrogen Solubility and Microstructural changes in Zircaloy-4 due to neutron irradiation.** Journal of ASTM International, 2011, **8**(1): p. 1-20.

[74] D. Stafford, **Multidimensional Simulations of Hydrides During Fuel Rod Lifecycle,** Journal of Nuclear Materials, 2015, **466**: p. 362-372.

[75] J. Mullin, J**Crystallization,** Fourth ed., Vol. 2001: Butterworth Heinemann.

[76] A. Myerson, **Handbook of Industrial Crystallization,** Second ed., Vol. 2002: Butterworth-Heinenmann.

[77] S. Palmtag, A. Godfrey, **VERA Common Input User Manual,** Consortium for Advanced Simulation of LWRs, CASL-U-2014-0014-002, February 23, 2015.

[78] R. Pawlowski, K. Clarno, R. Montgomery, R. Salko, T. Evans, J. Turner and D. Gaston, **Design of a High Fidelity Core Simulator for Analysis of Pellet Clad Interaction,** in ANS Joint International Conference on Mathematics and Computation, Nashville, April 2015.

[79] M. Mankosa, **Modeling of Hydrogen and Hydride Formation in Zirconium Alloy Cladding using High-fidelity Multi-physics Coupled Codes**, MS Thesis in nuclear engineering, The Pennsylvania State University, 2015.

[80] E. Lacroix, A. Motta, **Validation of BISON: Calculation of Hydrogen Distribution by Comparison to Experiment,** in TMS 2016: 145th Annual Meeting & Exhibition. Nashville. 2016. p. 263-272.

[81] A.T. Godfrey, **VERA Core Physics Benchmark Progression Problem Specifications,** Revision 4, August 2014.